



# Microglia-induced neurotoxicity and altered cell-autonomous functions in a LRRK2 G2019S model of Parkinson's disease

## Citation

Reilly, William. 2020. Microglia-induced neurotoxicity and altered cell-autonomous functions in a LRRK2 G2019S model of Parkinson's disease. Doctoral dissertation, Harvard University Graduate School of Arts and Sciences.

## Permanent link

<https://nrs.harvard.edu/URN-3:HUL.INSTREPOS:37368935>

## Terms of Use

This article was downloaded from Harvard University's DASH repository, and is made available under the terms and conditions applicable to Other Posted Material, as set forth at <http://nrs.harvard.edu/urn-3:HUL.InstRepos:dash.current.terms-of-use#LAA>

## Share Your Story

The Harvard community has made this article openly available.  
Please share how this access benefits you. [Submit a story](#).

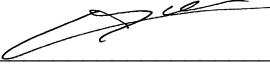
[Accessibility](#)


HARVARD UNIVERSITY  
Graduate School of Arts and Sciences




DISSERTATION ACCEPTANCE CERTIFICATE

The undersigned, appointed by the  
Department of Molecular and Cellular Biology  
have examined a dissertation entitled  
**Microglia-induced neurotoxicity and altered cell-autonomous functions in a  
LRRK2 G2019S model of Parkinson's disease**  
presented by **William Reilly**  
candidate for the degree of Doctor of Philosophy and hereby  
certify that it is worthy of acceptance.

Signature  \_\_\_\_\_  
Typed name: Prof. Catherine Dulac

Signature  \_\_\_\_\_  
Vladimir Denic (Aug 31, 2020 10:04 EDT)  
Typed name: Prof. Vladimir Denic

Signature  \_\_\_\_\_  
Jennifer Lipincott-Schwartz (Aug 28, 2020 13:59 EDT)  
Typed name: Prof. Jennifer Lippincott-Schwartz

Signature \_\_\_\_\_  
Typed name: Prof.

Signature \_\_\_\_\_  
Typed name: Prof.

Date: 8/27/20



Microglia-induced neurotoxicity and altered cell-autonomous functions in a LRRK2 G2019S  
model of Parkinson's disease

A dissertation presented

by

William Reilly

to

The Department of Molecular and Cellular Biology

In partial fulfillment of the requirements for the degree of

Doctor of Philosophy

in the subject of

Biology

Harvard University

Cambridge, Massachusetts

August 2020

© 2020 William Reilly

All rights reserved

**Microglia-induced neurotoxicity and altered cell-autonomous functions in a *LRRK2* G2019S model of Parkinson's disease**

**ABSTRACT**

Mutations in *LRRK2* are linked to the most common form of heritable, late-onset Parkinson's disease, and the *LRRK2* G2019S substitution is the most common *LRRK2* mutation in PD patients. PD is characterized by extensive death of dopaminergic neurons in the substantia nigra region of the midbrain, and significant work has been devoted to understanding the impact of the G2019S kinase-activating mutation on the health, sensitivity, and cell-autonomous function of neurons. However, an extensive body of evidence has emerged over the past decade to suggest that glial cells can induce non-cell-autonomous neurodegeneration. Motivated by these findings, we evaluated the ability of *LRRK2* G2019S microglia to impact dopaminergic neuron survival. Using a co-culture system in which the genotype of each cell type can be controlled, we observed a significant loss of dopaminergic neurons in the presence of *LRRK2* mutant microglia. We further observed dopaminergic neurotoxicity induced by conditioned medium collected from *LRRK2* G2019S microglia. In an attempt to better understand the microglia-intrinsic effects of the *LRRK2* mutation, we assayed multiple *LRRK2*-relevant organelles and cell biological pathways. We found that *LRRK2* G2019S microglia display increased mitochondrial fragmentation, decreased phagocytic activity, impaired endosome maturation, altered microtubule dynamics, and elevated chemotaxis activity in comparison to

wild-type controls. Taken together, our results suggest that the *LRRK2* G2019S mutation impacts microglial homeostasis and can lead to non-cell-autonomous dopaminergic neurodegeneration.

## Acknowledgements

I sincerely thank my PhD advisor, Erin O'Shea, for her consistent support over the course of my PhD. When I first read a selection of Erin's papers as an undergraduate, I was awed by the clear, concise, and incredibly logic-driven nature of her scientific writing. After joining Erin's lab, she continually challenged me to sharpen that scientific logic, focus on pivotal experiments and phenotypes, and consider how my results might fit into an intuitive, digestible story. Furthermore, Erin's willingness to support me in my transition from studying yeast genetics at Harvard to investigating PD-mutant glia in her lab at Janelia was extremely generous and directly impactful to my life and career. During my time at Janelia, I came to the conclusion that a non-academic career path was the right choice for me, and Erin supported me as I evaluated career options, applied for positions, and accepted a job offer. Erin's influence has been critical to my development as a scientist and as a PhD candidate with skills that are valuable outside of academia.

To my friends, including Chris Obara, James Angstman, Matt Smith, Georgia Squyres, Tess Oram, Katie Schretter, Mike Reiche, Katie Weiner, Sandy Mattei, Alyson Ramirez, Diego Baptista, Jason Gehrke, Felix Barber, Sean Wilson, and others: you have all been so supportive of me at every stage of my PhD, and I cannot imagine going through graduate school without you.

I would also like to thank my past and present lab-mates and collaborators who have helped guide my research and personal development. Aurelie de Rus Jacquet introduced me to glia, stem cells and primary culture, and my project would not exist without her patient instruction and her encouragement to study *LRRK2* mutant microglia. Chris Obara has



contributed immeasurably to my work, lending crucial microscopy and cell biology expertise as well as many, many hours of direct and indirect support for my research. Zhou Yu is a brilliant scientist with a successful career ahead of him, and he was always generous with his time and willing to share his knowledge and teach me long, labor-intensive protocols. Andrian Gutu has been a “lab dad” of sorts who did what needed to be done to keep the lab running and who was always there to give honest, direct feedback as well as technical assistance. Brian Zid was a mentor for me at a formative time in my early graduate school career, and the rest of the translation sub-group—Alicia Darnell and Rasi Subramaniam—helped me transition smoothly into the O’Shea lab.

I would also like to thank many other colleagues and members of the O’Shea group for their support and valuable conversations: Victor Wong, Mithil Jha, Jenna Tancredi, Jingyi Hou, Heejun Choi, Ya-Cheng Liao, Lauren Surface, Shankar Mukherji, Ania Puszynska, Kapil Amarnath, Kathleen Fleming, Anders Hansen, Bin He, Siting Gan, Peter Arvidson, and Michelle Quiambao. Members of Janelia’s core facilities have also been very helpful: Deepika Walpita and Jenny Hagemeyer for cell culture and primary culture; Kathy Schaefer for flow cytometry and FACS; and Crystall Lopez and the Vivarium team for mouse breeding and management.

In addition, I am very grateful to my committee members—Profs. Catherine Dulac, Vlad Denic, and Jennifer Lippincott-Schwartz—for providing invaluable advice and direction over the course of my graduate career. A long time ago, Vlad was my thesis co-advisor, and he remained as supportive and helpful as ever after he transitioned from advisor to committee member.

Finally, I would like to thank my family, without whom none of this would be possible. My wife has been a constant source of stability, rational thinking, and (usually very deserved) tough

love throughout my PhD. My parents encouraged me to pursue whatever I was passionate about, and that freedom put me in a position to pursue those passions while building a motivating and rewarding career. My two sisters have always been there to support me and pass on their older sibling wisdom, and seeing them at home and on trips was always a highlight of my moments away from the lab. The same can be said for my grandparents, who have believed in me—despite not really understanding what I do or how PhDs work—in the way that only proud grandparents can. Without my family, friends, colleagues, committee members and advisor, I would certainly not be where I am today.

## Table of contents

|  |             |
|--|-------------|
| <b>ABSTRACT</b> .....  | <b>iii</b>  |
| <b>Acknowledgements</b> .....  | <b>v</b>    |
| <b>Table of contents</b> .....   | <b>viii</b> |
| <b>List of Figures</b> .....   | <b>x</b>    |
| <b>List of Tables</b> .....  | <b>xi</b>   |
| <b>Abbreviations</b> .....   | <b>xii</b>  |
| <b>1 INTRODUCTION</b> .....  | <b>1</b>    |
| 1.1 Introduction to Parkinson’s disease, LRRK2, and glia-induced neurotoxicity .....                 | 1           |
| 1.2 Introduction to microglial biology and disease .....   | 2           |
| 1.3 An introduction to LRRK2, its cell biology, and the G2019S mutation .....                        | 8           |
| 1.4 LRRK2 in immune cells and microglia .....  | 14          |
| 1.5 Approach and Findings .....  | 16          |
| <b>2 RESULTS PART 1: Microglia-induced dopaminergic neurotoxicity</b> .....                          | <b>20</b>   |
| 2.1 Isolation and co-culture of primary microglia and midbrain DA neurons .....                      | 20          |
| 2.2 Co-culture of primary microglia and midbrain DA neurons.....                                     | 25          |
| 2.3 LRRK2 G2019S microglia induce DA neurotoxicity in a co-culture model .....                       | 29          |
| 2.4 LRRK2 G2019S microglia-conditioned medium induces DA neurotoxicity .....                         | 34          |
| 2.5 Chapter Summary .....  | 40          |
| <b>3 RESULTS PART 2: Characterization of cell-autonomous changes in LRRK2 G2019S microglia</b> ..... | <b>44</b>   |
| 3.1 Metabolic organelles: mitochondrial and lipid droplet morphology .....                           | 44          |
| 3.2 Microglial phagocytosis and the endolysosomal system .....                                       | 54          |
| 3.3 Migration/chemotaxis and microtubule dynamics .....  | 64          |
| 3.4 Chapter Summary .....  | 67          |
| <b>4 DISCUSSION</b> .....  | <b>71</b>   |
| 4.1 LRRK2 G2019S microglia-induced DA neurotoxicity.....   | 71          |
| 4.2 Characterization of cell-autonomous changes in LRRK2 G2019S microglia.....                       | 74          |
| 4.3 Integration of results and future directions.....  | 77          |
| 4.4 Therapeutic implications for PD.....   | 79          |
| <b>5 METHODS</b> .....   | <b>81</b>   |

|          |  |            |
|----------|--|------------|
| 5.1      | Serum- and BSA-free isolation and culture of primary mouse microglia ..... | 81         |
| 5.2      | Serum-free isolation and culture of primary midbrain neurons.....          | 86         |
| 5.3      | Co-culture of primary microglia and midbrain neurons .....                 | 91         |
| 5.4      | Microglia conditioned medium (MCM) culture of midbrain neurons.....        | 91         |
| 5.5      | Immunofluorescence of mouse primary cultures .....                         | 91         |
| 5.6      | Imaging and quantification of dopaminergic (TH+) neuron survival.....      | 92         |
| 5.7      | Mouse cytokine array .....   | 93         |
| 5.8      | Bead uptake imaging and analysis .....                                     | 93         |
| 5.9      | Phagocytosis flow cytometry assay.....                                     | 96         |
| 5.10     | Mitochondrial morphology imaging and analysis .....                        | 97         |
| 5.11     | Lipid droplet (LD) imaging and analysis .....                              | 100        |
| 5.12     | Endosome maturation imaging and analysis .....                             | 102        |
| 5.13     | Microtubule dynamics imaging and analysis .....                            | 104        |
| 5.14     | Migration and chemotaxis assays .....                                      | 105        |
| 5.15     | Reverse transcription and qPCR.....  | 106        |
| <b>6</b> | <b>APPENDIX .....</b>  | <b>108</b> |
| 6.1      | Supplementary Figures and Tables .....                                     | 108        |
| 6.2      | Image analysis code.....   | 113        |
| <b>7</b> | <b>REFERENCES.....</b>   | <b>153</b> |

## List of Figures

|  |     |
|--|-----|
| Figure 1 - Serum-free isolation and culture of primary microglia .....                                     | 22  |
| Figure 2 - Quality control for serum-free microglia.....   | 24  |
| Figure 3 - Midbrain neuron isolation and culture.....  | 27  |
| Figure 4 - Coculture of primary midbrain neurons and microglia .....                                       | 28  |
| Figure 5 - Genotype-specific neuron and microglia combinations in co-culture.....                          | 30  |
| Figure 6 - Microglia genotype-dependent DA neurotoxicity .....   | 32  |
| Figure 7 - Design of conditioned medium experiments .....  | 35  |
| Figure 8 - LRRK2 G2019S microglia conditioned medium causes DA neurotoxicity.....                          | 36  |
| Figure 9 - Analysis of MCM cytokine levels is inconclusive .....   | 38  |
| Figure 10 - Mitochondrial morphology analysis pipeline .....   | 46  |
| Figure 11 - Mitochondria are fragmented in LRRK2 G2019S microglia .....                                    | 48  |
| Figure 12 - Lipid droplet analysis pipeline .....  | 50  |
| Figure 13 - LPS treatment induces LD shrinking in wild-type and LRRK2 G2019S microglia .....               | 52  |
| Figure 14 - Impaired phagocytosis in LRRK2 G2019S microglia.....   | 58  |
| Figure 15 - LRRK2 G2019S mutation hinders endosome maturation .....  | 61  |
| Figure 16 - LRRK2 G2019S microglia display reduced tubulin recovery velocity and enhanced chemotaxis ..... | 66  |
| Figure 17 - A neuron-centric model for LRRK2-associated neurodegeneration.....                             | 72  |
| Figure 18 - Speculative model for LRRK2-linked neurodegeneration.....                                      | 73  |
| Figure 19 - A three-component, genotype-controlled culture system.....                                     | 74  |
| Figure 20 - <i>Ad hoc</i> evaluation of CX3CR1-GFP expressing cells in post-dounce suspension .....        | 108 |
| Figure 21 - Absence of non-specific, astrocyte, or neuron staining in primary MG immunofluorescence.....   | 109 |
| Figure 22 - Biological repeat results for lipid droplet microscopy assay .....                             | 111 |
| Figure 23 - Biological repeat results for mitochondrial morphology analysis .....                          | 111 |
| Figure 24 - Biological repeat results for endosome maturation assay .....                                  | 112 |
| Figure 25 - Biological repeat results for bead uptake assay .....  | 112 |

## List of Tables

|  |     |
|--|-----|
| Table 1 - Summary of LRRK2 G2019S microglia-intrinsic results .....        | 77  |
| Table 2 - Cytokines analyzed in membrane sandwich-based immunoassays ..... | 110 |

## Abbreviations

5-FDU - 5-Fluoro-2'-deoxyuridine

AD – Alzheimer's disease

A $\beta$  - amyloid- $\beta$

ATP – adenosine triphosphate

BDNF – brain-derived neurotrophic factor

BODIPY - boron-dipyrromethane

C1q – complement component 1q

CCCP – carbonyl cyanide *m*-chlorophenyl hydrazine

CCL3 – chemokine (C-C motif) ligand 3

CCL5 – chemokine (C-C motif) ligand 5

CCL6 – chemokine (C-C motif) ligand 6

CD – cluster of differentiation

CM – conditioned medium

CNS – central nervous system

CX3CR1 – CX3C chemokine receptor 1 (fractaline)

DA – dopamine/dopaminergic

DAPI – 4',6-diamidino-2-phenylindole

FITC – fluorescein isothiocyanate

GDNF – glia-derived neurotrophic factor

GFP – green fluorescent protein

HAVCR1 – hepatitis A virus cellular receptor 1

HEK293T – human embryonic kidney 293 with SV40 large T antigen

hiPSC – human induced pluripotent stem cell

IACUC - Institutional Animal Care and Use Committee

IBA-1 – ionized calcium binding adaptor molecule 1

IL-1 $\beta$  - interleukin-1 $\beta$

iNOS - inducible nitric oxide synthase

iPSC – induced pluripotent stem cell

LD – lipid droplet

L-DOPA - L-3,4-dihydroxyphenylalanine

LPS - lipopolysaccharide

LRP -low-density lipoprotein receptor-related protein

LRRK2 – leucine rich repeat kinase 2

MACS – magnetic-activated cell sorting

MAP2 – microtubule-associated protein 2

MCM – microglia conditioned medium

M-CSF - macrophage colony-stimulating factor

MEF – mouse embryonic fibroblast

MMP2 – matrix metalloproteinase 2

mGlu2 - metabotropic glutamate receptor 2

NFAT – nuclear factor of activated T-cells

NF- $\kappa$ B – nuclear factor kappa-light-chain-enhancer of activated B cells

NLRC4 – NLR family CARD domain-containing protein 4



NO – nitric oxide

P2RY12 – purinergic receptor P2Y12

PD – Parkinson's disease

PS – phosphatidylserine

PM – plasma membrane

PRR – pattern recognition receptor

qPCR – quantitative polymerase chain reaction

RNS – reactive nitrogen species

RONS – reactive oxygen and nitrogen species

ROS – reactive oxygen species

Siglec - sialic acid binding immunoglobulin-like lectin

SIRP $\alpha$  - signal-regulatory protein alpha

SN – substantia nigra

SOD1 – superoxide dismutase 1

TGF- $\beta$ 2 - transforming growth factor  $\beta$ 2

TGF- $\beta$ 3 - transforming growth factor  $\beta$ 3

TH – tyrosine hydroxylase

TLR – Toll-like receptor

TMEM119 – transmembrane protein 119

TMR - tetramethylrhodamine

TNF $\alpha$  - tumor necrosis factor- $\alpha$

TOMM20 – translocase of outer mitochondrial membrane 20

TREM2 - triggering receptor on myeloid cells 2

TUBB – tubulin beta chain

VTA – ventral tegmental area

# 1 INTRODUCTION

## 1.1 Introduction to Parkinson's disease, LRRK2, and glia-induced neurotoxicity

Parkinson's disease (PD) is a prevalent neurodegenerative disorder characterized by the death of dopaminergic (DA) neurons in the substantia nigra (SN) region of the midbrain [1]. Though the clinical presentation of the disease is consistent, there is a high degree of variability in the mutations that cause PD [2]. Of particular interest are a small subset of variants that cause heritable PD, including autosomal dominant mutations in *LRRK2*, *SNCA* and *VPS35*, as well as autosomal recessive mutations in *PRKN*, *DJ-1*, and *PINK1* [3]. This work focuses on LRRK2 (leucine-rich repeat kinase 2), a large, multi-domain protein that possesses both kinase and GTPase activity, as well as a WD40 domain and unique "LRRK2-repeats" [4]. A wide array of LRRK2 substrates have been identified *in vitro*, and Rab GTPases are thought to be a key substrate of the wild-type kinase [5]. The *LRRK2* G2019S mutant—the focus of this work—has a kinase-activating mutation that has been implicated in compromised autophagy, mitophagy, vesicle trafficking, neurite outgrowth, and synaptic function [1]. Study of other PD genes in cellular and animal models has further suggested defects in protein folding, the ubiquitin-proteasome system, and mitochondrial function as hallmark cellular features of PD [1].

However, emerging work in cellular neuroscience suggests that linking PD mutations such as *LRRK2* G2019S to these cell-autonomous neuronal functions will not fully explain the disease state. Rather, mounting evidence suggests that neuroglia, including astrocytes and microglia, are sensitively tuned support cells whose misregulation can be highly toxic to neurons [6-8]. Related to PD, a recent study has demonstrated that activated microglia can convert astrocytes into a reactive state (termed 'A1'), which subsequently induces neuronal

death [9]. The authors observed A1 astrocyte enrichment in a number of neurodegenerative diseases, including a 20-fold increase in the SN of PD patients [9]. These results suggest that contrary to previous thinking, neuroinflammation may not simply be a neuroglial response to neuronal malfunction. Rather, neuroglial reactivity may *contribute* to neuronal malfunction, and this reactivity should be investigated as an extrinsic stressor of neurons.

## **1.2 Introduction to microglial biology and disease**

In this work, we focus solely on the role of microglia in *LRRK2*-linked neurodegeneration. Microglia are one of many types of tissue-resident macrophages of the innate immune system, and microglia are distinguished by their exclusive localization to the central nervous system (CNS) [10]. Similar to the developmentally-related Kupffer cells (liver), Langerhans cells (skin), alveolar macrophages (lungs) and spleen macrophages, microglia originate from yolk-sac derived erythro-myeloid progenitors and perform specialized macrophage functions in their resident tissue [11-14]. These specialized activities allow microglia to adopt three general states in the brain: 1) sensing, 2) housekeeping, and 3) protecting against endogenous and exogenous stressors [15]. Although these categories are overly simplified and fail to highlight the numerous sub-states that microglia can adopt, they nonetheless provide a high-level structure for describing and understanding microglial biology.

### **1.2.1 Microglial activation states**

When microglia are in the sensing or “sentinel” state, they adopt a highly ramified morphology that allows their thin, dynamic processes to constantly surveil the surroundings and respond to changes in their environment [16]. In response to certain environmental stimuli, microglia may enter the housekeeping or “nurturer” state. In this state, microglia remain

ramified but perform a number of homeostatic functions, including clearance of apoptotic neurons, supporting neurogenesis and axonal growth, regulation of angiogenesis, and pruning of synapses [10]. In contrast, stressful environmental stimuli may convert microglia to a protective “warrior” state, which is usually characterized by retraction to a less ramified, more amoeboid morphology [17]. In this state—often termed “activated”—microglia can display enhanced phagocytic capacity, activation of inflammatory pathways, and secretion of pro-inflammatory cytokines and chemokines [18]. To provide background on the microglia functions that are central to our research, will begin with a brief overview of microglia’s homeostatic role in neuron clearance before proceeding to a summary of their neuroinflammatory (and potentially neurotoxic) behaviors in the “warrior” or “activated” state.

### **1.2.2 Microglial phagocytosis in CNS homeostasis**

In many ways, brain development can be considered somewhat wasteful, with neuronal apoptosis representing a crucial process in the maturation of the CNS [19, 20]. Because PD is characterized by extensive neuronal death, it is useful to understand the central role of microglia in the homeostatic clearance of dying neurons. One of the key characteristics shared by macrophages (tissue-resident or not) is their capacity for phagocytosis [21], and microglia’s role in the clearance of apoptotic neurons is thought to depend largely on their phagocytic activity [22]. Though this phagocytic activity in brain homeostasis is evident, the precise pathway that leads from neuronal apoptotic signaling to internalization by microglia is not well-understood. Many hypotheses point to the well-established “eat-me” signaling carried out by the flipping of phosphatidylserine (PS) to the outer leaflet of the plasma membrane (PM) as a likely mechanism. Indeed, recent work has demonstrated that the machinery necessary to

detect extracellular PS is well-expressed in microglia, and the activation of this pathway regulates phagocytic activity in microglia [23].

Importantly, phagocytosis requires that the target cell (*e.g.* neuron) must be in direct contact with microglia, which begs the question of how microglia recognize and migrate toward apoptotic neurons in need of phagocytosis. Although these neuronal “find me” chemotactic signals are not fully characterized, the generic macrophage attractants ATP and lysophosphatidylcholine are promising targets [24-27]. To date, the best understood chemoattractant is likely CX3CL1 (fractaline), which is released by apoptotic neurons and attracts microglia *in vitro* [28]. Furthermore, when microglia *in vivo* lack the receptor for CX3CL1, they fail to chemotax toward apoptotic neurons [28]. In addition to CX3CL1, the ligands for microglial cell-surface receptors such as SIRP $\alpha$  (signal-regulatory protein alpha), complement receptor 3, LRP (low-density lipoprotein receptor-related protein), TREM2 (triggering receptor on myeloid cells 2), and Siglecs (sialic acid binding immunoglobulin-like lectins) can all modulate microglial migration and phagocytosis [29-32], which adds to the possible repertoire of neuron-derived “find me” and “eat me” signals. Taken together, the evidence for microglia’s fundamental role in clearing apoptotic neurons makes it attractive to infer that in neurodegenerative diseases like PD, the role of microglia may be as simple as responding to “find me” and “eat me” signals from diseased, apoptotic neurons.

However, recent work suggests that this “eat me” signaling is not always unidirectional. Rather, exogenous activation of microglia can induce a response termed ‘phagoptosis’, wherein microglia actively phagocytose healthy, non-apoptotic neurons [33]. In this pathway, activated microglia release sub-toxic concentrations of soluble mediators (including peroxynitrite) that

induce neurons to expose a reversible PS “eat me” signal [34]. If PS bridging proteins and microglia are in direct contact with neurons, this induces microglial phagocytosis of the neurons. However, if either the bridging molecules or microglia are not in direct contact with the neurons, then the neurons can recover and survive [34]. With phagoptosis, microglia do not simply phagocytose and clear an already-dying neuron, but they instead contribute directly to the neuron’s death. In recent years, it has also become clear that microglia’s “warrior” functions can have similarly neurotoxic outcomes.

### **1.2.3 Microglial activation and neurotoxicity**

In addition to their central role in CNS development and homeostasis, microglia are actively involved in protecting the brain against harmful endogenous and exogenous stimuli. These stimuli can include pathogens; CNS tumors; endogenous proteins like A $\beta$ ,  $\alpha$ -synuclein, and mutant huntingtin; cytokines; and drugs [15]. In order to sense and respond to these widely varying ligands, microglia express an array of pattern recognition receptors (PRRs), viral receptors, Toll-like receptors (TLRs), Fc receptors, and anti-pathogenic peptides [35]. Upon sensing one or multiple of these harmful stimuli, microglia can enter the “activated”/“warrior” state that is characterized by drastically altered gene expression, morphology, and microglial behavior [36]. Activation encompasses a wide range of microglial responses to varied stimuli, so there is not a single stereotypic “activation state” that can be precisely defined by a uniform gene expression and cell biological response to these stimuli [36]. In many cases, however, activated microglia can be distinguished by a transition from a highly ramified morphology to an amoeboid or stockier morphology associated with process shortening and swelling of the soma [15]. Concomitant with this morphological change, activation is often associated with microglial

proliferation, upregulated phagocytic activity, enhanced motility, and the release of inflammatory cytokines and small molecules [37, 38]. Importantly, these secreted factors can be anti-inflammatory proteins such as glia-derived neurotrophic factor (GDNF) and brain-derived neurotrophic factor (BDNF), or they can be pro-inflammatory molecules such as tumor necrosis factor- $\alpha$  (TNF $\alpha$ ), interleukin-1 $\beta$  (IL-1 $\beta$ ), fatty acid metabolites (including eicosanoids), and reactive oxygen and nitrogen species (RONS) including nitric oxide (NO), superoxide, and the aforementioned peroxynitrite [39]. To add to this complexity, some cytokines can be either pro- or anti-inflammatory depending on their local context [40].

Although the wide range of potential microglial activation states are not fully characterized, there is strong evidence that some forms of activated microglia can promote neurotoxicity and neurodegeneration. As described above, seminal work in the field has demonstrated that microglia activated by bacterial lipopolysaccharide (LPS) can secrete defined factors that convert astrocytes to a reactive “A1” state, and those astrocytes in turn secrete potentially neurotoxic soluble factors [9]. However, direct microglia-to-neuron toxicity has also been demonstrated, for example in the previously-described case of activated microglia carrying out phagoptosis of viable neurons [34].

Another proposed mechanism of direct neuron killing includes the secretion of pro-apoptotic cathepsin B, which can be released by activated microglia and causes neurotoxicity in conditioned medium experiments [41]. In a similar soluble factor mechanism, stimulation of the metabotropic glutamate receptor mGlu2 in microglia was shown to induce TNF $\alpha$  and Fas ligand release, which causes neurotoxicity only in the presence of microglia or microglia-conditioned medium [42]. In addition, a significant body of work has focused on inducible nitric oxide



synthase (iNOS) activation in microglia, which leads to the release of NO. When NADPH oxidase (PHOX) is concurrently activated in microglia, peroxynitrites are produced at concentrations that directly kill neurons [43]. Finally, in a somewhat inverted mechanism, if activated microglia fail to produce neurotrophic factors like BDNF and IGF1, the absence of required neurotrophins can result in neuronal death [38, 44]. To date, then, four distinct mechanisms of microglia-induced neurotoxicity have been identified: 1) direct phagocytosis of viable neurons via phagoptosis, 2) indirect neurotoxicity wherein activated microglia act in concert with other cell types (*e.g.* astrocytes) to kill neurons, 3) direct neurotoxicity mediated by microglia-released soluble factors, and 4) direct neurotoxicity caused by the failure of microglia to provide neurotrophic factors.

#### **1.2.4 Microglia in neurodegenerative disease**

Building on this work that predominantly relies on exogenous activation of microglia, many researchers have focused on the neurotoxic roles of microglia in neurodegenerative disease. In Alzheimer's disease (AD) models, the release of ASC protein by A $\beta$ -activated microglia promotes further A $\beta$  oligomer and aggregate formation and seeds an enhanced A $\beta$  pathology [45]. Similarly, A $\beta$ -induced microglial release of cytokines promotes tau hyperphosphorylation and AD neuropathology [46, 47]. In mouse models of multiple sclerosis (MS), microglia secrete RONS, proteases and proinflammatory cytokines that lead to toxicity in neurons, and inhibition of this microglial response reduces CNS inflammation and axonal damage [48]. In ALS models, expression of mutant *SOD1* in microglia accelerates the onset of disease, and activation of microglia increases motor neuron death [49, 50]. Similar microglia-associated toxicity has been observed in Huntington's disease [51] and prion diseases [52]. An

attractive hypothesis for the progression of microglial toxicity in these diseases suggests that microglia can perform beneficial “nurturer” or “warrior” functions early in disease progression, but the accumulation of exogenous stressors (*e.g.* A $\beta$  and tau aggregates) or the activity of endogenous microglial proteins (*e.g.* mutant *SOD1*) tips the balance toward constitutive and neurotoxic proinflammatory phenotypes [15].

Due to limitations in current animal models of PD, mechanistic work linking microglia to neurotoxicity in PD is lacking. However, it is clear that reactive, proinflammatory microglia are abundant in the brains of human PD patients [53, 54]. Furthermore,  $\alpha$ -synuclein—a protein whose aggregates are considered a hallmark of PD—has been shown to activate microglia [55], and activated microglia are observed to accumulate near aggregates of  $\alpha$ -synuclein in post-mortem PD patient samples [56]. However, a causative role for  $\alpha$ -synuclein-activated microglia in PD neurotoxicity has yet to be established, and the contribution of  $\alpha$ -synuclein itself to PD pathology—beyond its marker status—remains unclear (and controversial) [57-59]. And although  $\alpha$ -synuclein may be the most widely-known histological marker and genetic link to PD, autosomal dominant mutations in *LRRK2*— one of which is the focus of our work—represent the most frequent cause of monogenic PD [60]. Having surveyed the numerous precedents for microglial activation and malfunction in neurotoxicity and neurodegenerative disease, we will next review the current state of our knowledge of *LRRK2*, with a particular focus on the cell biological consequences of *LRRK2* malfunction.

### **1.3 An introduction to *LRRK2*, its cell biology, and the G2019S mutation**

A recent review from leaders in the field aptly described the current state of our knowledge of *LRRK2*: “Important advances have been made in distinct areas... [but] many

details are missing and the field remains a long way from agreement” [61]. As is the case with most proteins, it is instructive to first understand LRRK2 on the basis of its biochemical structure and function. In addition to four protein-interaction domains, LRRK2 has two enzymatic domains—a kinase and a GTPase—that are central to its disease relevance [62]. Though a number of pathogenic mutations have been identified in the GTPase domain [63], the LRRK2 GTPase sub-field has been frustrated by an inability to identify interacting effector proteins, leading some to conclude that LRRK2’s GTPase activity may be solely self-regulatory [61].

### **1.3.1 LRRK2 kinase activity**

The better-studied of the enzymatic motifs is the serine-threonine kinase domain, and the first physiological substrate of LRRK2’s kinase activity to be identified was LRRK2 itself [64]. However, evidence for the physiological relevance of LRRK2 autophosphorylation is scant, and a landmark study in 2016 identified a subset of Rab GTPases (RAB8A/B, RAB12, RAB10, RAB3A/B/C/D, RAB29, RAB35, and RAB43) as *bona fide* heterologous LRRK2 kinase substrates [5]. The field has since coalesced around Rab phosphorylation as a key driver of LRRK2 biology, and subsequent work has characterized the ability of LRRK2 phosphorylation to alter Rab GTPase binding to both upstream and downstream proteins [5, 65]. These LRRK2-regulated changes in Rab GTPase activity have so far been linked to ciliogenesis, endocytosis, and centrosome positioning [65, 66]. Importantly, multiple pathogenic LRRK2 mutations are found in the kinase domain, including G2019S (the focus of this work) [60, 61]. Initially in biochemical assays, and later in studies of autophosphorylation and Rab phosphorylation, the G2019S mutation has been shown to robustly increase LRRK2 kinase activity [5, 64, 65, 67]. Thus, along

a spectrum of variants including *LRRK2* KO, *LRRK2* knockdown, wild-type *LRRK2*, and hyperactivating kinase mutations like G2019S, *LRRK2* biologists possess a number of tools for probing *LRRK2* function in varying cell types and cell biological contexts.

### **1.3.2 *LRRK2* in autophagy**

Although the use of such *LRRK2* genetic tools does not generally provide deep mechanistic insight into specific *LRRK2* interactions and upstream/downstream effectors (as has been achieved in the ciliogenesis and centrosome work above), research with *LRRK2* genetic variants has shed significant light on the range of cell biological processes impacted by *LRRK2* activity [61]. For example, both animal and cellular models have provided strong evidence for *LRRK2*'s role in regulating autophagy [68-77]. In a *LRRK2* KO mouse model, significant age-dependent effects on macroautophagy in the kidney were observed [68]. At 7 months, elevated expression of LC3-II and p62 and increased lipofuscin deposition in the kidneys suggested elevated macroautophagic activity, whereas the same markers indicated decreased macroautophagy at 20 months of age [68]. In cellular models, pharmacological inhibition of *LRRK2* kinase activity leads to increased macroautophagy in some cell types (the SH-SY5Y neuroblastoma, HEK293T, and H4 neuroglioma cell lines, as well as primary astrocytes) [69-71], but the opposite effect is observed in BV2 pseudo-microglia and RAW264.7 macrophage cell lines [72]. Building on this context-dependence of macroautophagy regulation, over-expression of *LRRK2* or its hyperactivating mutants (including G2019S) in SH-SY5Y and HEK293T cells was shown to induce autophagy [73-75], whereas these same mutants display decreased autophagy in primary mouse neurons and PD patient-derived fibroblasts [76, 77].

### 1.3.3 LRRK2 and the endolysosomal system

Abundant evidence also points to a role for LRRK2 in regulating endocytosis, phagocytosis, and the broader endolysosomal system [78-88]. Due to the relevance of LRRK2 to PD and the central role of endocytosis in synaptic activity and neuronal regulation, much of this work has been performed in neuronal models. For example, interactions between LRRK2 and RAB5a at neuronal synapses have been observed, and both knockdown and overexpression of *LRRK2* in primary neuron cultures was shown to impair synaptic vesicle endocytosis [78]. Confirming the knockdown aspect of this experiment, a number of subsequent studies have similarly observed decreased synaptic vesicle endocytosis in the absence of LRRK2 [78-81]. Further downstream in the endolysosomal system, recent work has shown that over-expression of *LRRK2* or the hyperactive G2019S mutant delays receptor trafficking and degradation by impairing late endosomal budding in HeLa cells[82], and this deficit has been directly linked to G2019S-associated misregulation of the LRRK2 substrate RAB8A [83]. Furthermore, LRRK2 and a number of its aforementioned Rab substrates (RAB8, RAB10, and RAB12) are recruited to stressed lysosomes and are required to maintain lysosomal homeostasis under stress in HEK293 cells [84]. In addition to regulating lysosomal homeostasis, the *Drosophila* homolog of LRRK2 has been shown to regulate lysosomal positioning, with the G2019S mutant disrupting RAB7 regulation of perinuclear lysosome positioning [85]. Regarding phagocytosis, LRRK2 has been observed to negatively regulate the maturation of *M. tuberculosis* phagosomes in macrophages, and although inhibition of LRRK2 enhanced phagosome maturation, the effects of hyperactive mutants (such as G2019S) were not tested [86]. Again illustrating the context

dependence of LRRK2 activity, inhibition of LRRK2 has also been shown to instead downregulate phagocytosis in some myeloid cell models [87, 88].

#### **1.3.4 LRRK2 and metabolic organelles**

In addition to its clear relevance to—and often contradictory roles in—autophagy and the endolysosomal system, LRRK2 appears to impinge on metabolic pathways, including lipid storage [75, 89, 90] and mitochondrial regulation [91-99]. With regards to lipid storage, LRRK2 has been shown to regulate lipid droplet (LD) formation and storage capacity via phosphorylation of RAB8A [89]. In HEK293T cells, overexpression of the LRRK2 kinase domain caused an increase in the number of LDs per cell [75], and a study in *LRRK2* KO mice has reported enhanced lipid droplet accumulation in the kidneys as well as hepatocytes and stellate cells [90]. Taken together, these results suggest that *LRRK2* misregulation in either direction—both knockout and kinase overexpression—can cause defects in lipid storage.

In studies of mitochondria, strong evidence links the G2019S mutation to increased sensitivity to mitochondrial toxins in both animal models [91, 92] and human iPS models [93, 94]. Furthermore, analysis of *LRRK2* mutation-carrying PD patient fibroblasts demonstrated aberrant activity of mitochondrial complexes IV and III [95]. Numerous studies have also reported altered mitochondrial morphology—including fragmentation—in mouse striatal brain slices and patient fibroblasts [96-98]. However, in contrast to work with autophagy and the endolysosomal system, there is scant evidence for physical interactions between LRRK2 and mitochondria (or mitochondrial proteins) in basal conditions. However, upon depolarization with drugs like Antimycin A and CCCP, LRRK2 localizes to the outer mitochondrial membrane via interactions with the Miro protein [99]. This is particularly intriguing because Miro is a tether

protein that links mitochondria to microtubule motor proteins, and the interaction between LRRK2 and Miro is required for transport and mitophagy of damaged (depolarized) mitochondria [99]. However, the *LRRK2* G2019S mutant fails to facilitate this interaction and subsequent microtubule-dependent mitophagy [99]. As we will see in the next section, there is a significant body of work linking LRRK2 to microtubules and the cellular pathways that they intersect with.

### **1.3.5 LRRK2 and cytoskeletal regulation**

Not long after the discovery of LRRK2, its binding to microtubules was observed [100, 101], and direct interactions between LRRK2 and three isoforms of  $\beta$ -tubulin—TUBB, TUBB4 and TUBB6—were unambiguously identified a decade later [102]. Because the binding site to these  $\beta$ -tubulins was found to be near that of Taxol—the classic microtubule-stabilizing drug—it was suggested that LRRK2 binding may influence microtubule stability [102]. Perhaps surprisingly, analysis of *LRRK2* KO MEFs and mouse kidneys showed a robust increase in microtubule acetylation [102, 103], which is a post-translational modification that increases microtubule stability. These results suggest that wild-type LRRK2 may preferentially interact with dynamic—rather than stabilized—microtubules, a hypothesis that corroborated well with the observation that LRRK2 is enriched on the highly dynamic microtubules of neuronal growth cones, in comparison to the less dynamic axonal microtubules in the same neurons [102]. Accordingly, later work demonstrated that LRRK2 interactions with microtubules are decreased when cells are treated with a tubulin acetylase or deacetylase inhibitors, both of which increase tubulin acetylation and elevate microtubule stability [104].

When we take into consideration these results and the previously-mentioned relationship between pathogenic *LRRK2* mutations, Rab GTPase activity, and deficits in cilia and centrosomes—both of which are large microtubule-based structures—as well as microtubule-dependent mitophagy mediated by Miro, the apparent link between *LRRK2* activity and microtubule regulation deepens [65, 99, 105]. In addition, trafficking of membranous organelles and vesicles on microtubules is central to autophagy and the endolysosomal system, both of which can be greatly dysregulated by *LRRK2* malfunction [61]. Though the extent to which direct *LRRK2*-microtubule interactions influence these structures and cell biological processes is unknown (and may be non-existent), microtubule biology links many of the disparate cellular processes that are impacted by *LRRK2* activity. It should be noted that in addition to the cell systems described above, *LRRK2* is also implicated in regulation of the endoplasmic reticulum, the *trans*-Golgi network, and translation [61]. The original research presented here will describe high-level changes in multiple of the aforementioned cell biological processes in *LRRK2* mutant microglia.

#### **1.4 *LRRK2* in immune cells and microglia**

Before moving on to our specific findings, we will briefly review the current knowledge of *LRRK2*'s impact on immune cell and glial function, and we will summarize the motivation for this work. Though the literature on *LRRK2* and glia—and in particular microglia—is sparse, there is strong evidence of a physiological role for *LRRK2* in immune cells [106-115]. Robust *LRRK2* expression has been reported in a number of immune cell types and cell lines, including monocytes, B lymphocytes, neutrophils, microglia, bone-marrow derived macrophages, bone-marrow derived dendritic cells, the RAW264.7 macrophage cell line, and the THP-1 monocyte



cell line [106-112]. At the level of upstream and downstream signaling, LRRK2 activity is implicated in multiple immune-relevant pathways, including its phosphorylation by I $\kappa$ B family kinases [112], its regulation of the classical inflammatory mediator NF- $\kappa$ B [111], and its repression of innate immune response-regulating transcription factor NFAT [110]. In this context, the reported genetic links between *LRRK2* and inflammatory conditions such as Crohn's disease, leprosy, and tuberculosis may not be surprising [61, 116].

Regarding functional outcomes in immune cells, a study in mouse macrophages reported that activation of NLRC4-containing inflammasomes in response to *Salmonella enteric* Typhimurium infection was significantly decreased in *LRRK2* KO macrophages compared to wild-type [113]. This decreased inflammasome response was associated with impaired pathogen clearance following infection. As might be expected, macrophages from mice expressing *LRRK2* G2019S showed *increased* inflammasome activation and pathogen clearance, as compared to both wild-type and the KO [113]. Also in *LRRK2* KO macrophages, recent work has demonstrated that KO macrophages display reduced interferon responses to the *Mycobacterium tuberculosis* pathogen and cytosolic nucleic acid agonists [114]. Recalling the cell biological functions of *LRRK2* described above, the authors linked this deficiency to multiple mitochondrial stresses, including mitochondrial fragmentation and oxidative stress due to reduced levels of purine metabolites. Unfortunately, the authors did not study the impact of hyperactive *LRRK2* mutations (like G2019S) on this response.

In results that are perhaps unsurprising, microglia—the resident macrophages of the CNS—display similar inflammatory phenotypes in *LRRK2*-deficient mice [115]. In both *LRRK2* KO and pharmacological inhibition conditions, microglia were observed to have an impaired

inflammatory response to LPS stimulation that was mediated through the NF- $\kappa$ B pathway [115]. Though this work did not examine *LRRK2* point mutants, a separate study found that the *LRRK2* R1441G mutation (which is localized to the *LRRK2* GTPase domain but is associated with increased kinase activity) causes elevated cytokine release from LPS-stimulated microglia [106].

When we integrate these *LRRK2*-related observations in microglia and other immune cells with the previously-described capacity for microglia to directly and indirectly mediate neurotoxicity and neurodegeneration [9, 34, 38, 41-44] (see Section 1.2.3) and the observation of extensive microglial activation in the SN of PD patients [53, 54], two questions naturally arise: **what are the effects of *LRRK2* mutations—and in particular *LRRK2* G2019S—on the function of microglia, and how do these mutation-carrying microglia impact neuronal health and survival?**

## 1.5 Approach and Findings

To answer these key questions, we have divided our research into two parallel workflows. In the first, we sought to answer the question of how *LRRK2* G2019S mutant microglia impact the survival of neurons. In addressing this question, **we hypothesized that G2019S mutation-carrying microglia promote dopaminergic neurotoxicity**, based on the precedents described above for microglia-mediated neurotoxicity [9, 34, 38, 41-44] and *LRRK2*-associated defects in immune (and in particular, microglia) cells [106-115]. To test this hypothesis, we chose to use an established homozygous *LRRK2* G2019S mutant mouse line with the mutation knocked into the endogenous *LRRK2* locus [117], which is back-crossed to the parental strain (Taconic B6NTac) in our lab at least every 5 generations. Using this murine model, we employed mouse primary mono- and co-culture methods for both microglia and midbrain dopaminergic neurons.

In contrast to most prior work in the mouse microglia field, our microglia isolation and culture methods are based on serum-free techniques [118].

With these culture approaches, we demonstrate that microglia carrying the G2019S mutation cause dopaminergic neurotoxicity, and this neurotoxicity appears to be limited to dopaminergic neurons. Furthermore, we discovered that microglial G2019S-derived neurotoxicity can be mediated by microglial conditioned medium (MCM) alone, in the absence of direct microglia-neuron co-culture. This result suggests that microglia-induced neurotoxicity may be mediated by soluble factors. Because phagocytosis—another prominent neuron-killing function observed in microglia—requires direct contact between the phagocyte and the target cell, our results disfavor a phagocytic hypothesis for *LRRK2* G2019S-associated neurotoxicity. Using commercially available cytokine analysis reagents, we attempted to identify soluble factor(s) responsible for this neurotoxicity, but these experiments were inconclusive. We hope that further research can define the precise mechanism that underlies this microglia-induced neurotoxicity, as the identification of relevant factors could enable rescue of the neurotoxicity phenotype. Taken together with the recent observation of *LRRK2* G2019S astrocyte-derived neurotoxicity in our lab (de Rus Jacquet, submitted) and in other groups [119], these results suggest a potential role for glia-derived neurotoxicity in the progression of *LRRK2*-associated PD.

In parallel to this work, we also sought to better understand the microglia-intrinsic effects of the *LRRK2* G2019S mutation. To guide our research into altered microglia-intrinsic behavior, we integrated the existing knowledge of microglial function and *LRRK2*-dependent cell biological processes described in Chapter 1.2 and 1.3 to identify three general topics that were

tractable to examine in our system: 1) the structure and morphology of metabolic organelles (mitochondria and lipid droplets), 2) microglial phagocytosis and the endolysosomal system, and 3) cytoskeletal dynamics and migration/chemotaxis. Across these 3 topics, we used a combination of advanced confocal microscopy techniques, quantitative image analysis pipelines, and *in vitro* assays to characterize wild-type and *LRRK2* G2019S microglia. In particular, our microscopy and analysis pipelines allowed for robust quantification of cell biological properties in thousands of cells with diffraction-limited and super-resolution techniques, which to our knowledge has not been achieved in either the microglial or *LRRK2* fields.

Using these experimental approaches, we demonstrate genotype-dependent changes in mitochondrial morphology, bead phagocytosis, endosome maturation, chemotaxis, and tubulin dynamics. Though we have not mechanistically linked these cell biological defects to the neurotoxicity results summarized above, we hope that these observations will provide future researchers with targeted starting points for mechanistic work. In addition, we believe that the microscopy and image analysis pipelines that we have built (the code for which is included in Appendix 6.2) will facilitate further studies of the fascinating cell biology of microglia, mutant or not. We do not report genotype-dependent differences in lipid droplet morphology, but we do demonstrate stimulation-dependent changes in LD morphology. Furthermore, we identify in microglial cells intracellular lipid ‘rods’ or ‘fibrils’, which to the best of our knowledge resemble lipid structures only reported in the chromoplasts of certain plant cells [120-123]. Taken together, in addition to potentially novel LD biology, we observe cell-intrinsic changes in microglial function and cell biology in the *LRRK2* G2019S mutant, and these observations

appear to be consistent with the previously-described regulatory role that LRRK2 plays in major cellular processes [61].

## **2 RESULTS PART 1: Microglia-induced dopaminergic neurotoxicity**

To test the hypothesis that *LRRK2* G2019S mutant microglia induce dopaminergic neurotoxicity, we developed a mouse primary co-culture system. This system enables us to separately isolate wild-type and *LRRK2* G2019S microglia and midbrain neurons, which allows for co-culturing microglia of either genotype with wild-type neurons. Initially, this system was developed in parallel to a human induced pluripotent stem cell (hiPSC) co-culture model that employed published methods to differentiate microglia [124] and dopaminergic neurons [125] from wild-type and patient stem cell lines *in vitro*, but the hiPSC model was abandoned due to intractable issues with the batch-to-batch consistency and yield of hiPSC-derived microglia, as well as their questionable relevance to physiological human microglia. However, progress is accelerating rapidly in the hiPSC field, so we hope that future researchers will be able to replicate our results in human models.

### **2.1 Isolation and co-culture of primary microglia and midbrain DA neurons**

In anticipation of co-culturing microglia with midbrain DA neurons, we first adapted a well-validated protocol for serum-free isolation and culture of primary rodent microglia [118]. In this work, the Barres group determined that prevalent methods for isolating and culturing rodent microglia—which rely on bovine serum in both the purification and subsequent culture of microglia—fundamentally alter the behavior of the cells, even after withdrawal of serum [118]. Anecdotally, in our hands these commonly used serum-dependent methods produced cultures of amoeboid and proliferative microglia, both of which are characteristics attributed to an activated/“warrior” microglial state (reviewed in Chapter 1.2). To develop their serum-free protocol, the Barres group identified cholesterol and the astrocyte-secreted proteins

macrophage colony-stimulating factor (M-CSF) and transforming growth factor  $\beta$ 2 (TGF- $\beta$ 2) as factors that were crucial to microglial survival [118]. Similar requirements have been observed in the serum-free culture of human iPSC-derived microglia-like cells [124]. As such, we integrated these key components into our culture technique.

The microglia isolation protocol consists of 4 crucial steps (Figure 1a), all of which have precedent in either the rat or mouse purification protocols developed by the Barres group [118, 126], and which have also been implemented successfully by other groups [127]. First, mice aged p12-15 are transcardially perfused to clear the blood vessels and avoid potential contamination by non-microglial myeloid cells [126]. Following removal of the perfused brain, the brain tissue was subjected to physical dissociation by douncing, which serves two purposes. First, physical homogenization avoids the requirement for enzymatic (*e.g.* papain) dissociation, which in many protocols is subsequently neutralized by serum [128]. Second, although dounce homogenization is generally associated with low-heat lysis of cells in tissue samples, microglia are small enough to avoid lysis. As illustrated by *ad hoc* fluorescence microscopy of a post-douncing cell suspension derived from a CX3CR1-GFP (monocyte-labelling) mouse line (Appendix 6.1, Figure 20), GFP-expressing microglia appear to be enriched well beyond the 5-10% composition expected for a typical brain suspension [129]. Following dounce homogenization, we removed contaminating myelin via density gradient centrifugation, as mice aged p12 and above produce sufficient myelin to cause downstream issues if the debris is not removed [118]. The final isolation step is antibody-based purification that takes advantage of the CD11b cell surface protein expressed by microglia [130]. To achieve this, we employed bead-based magnetic-activated cell (MACS; Miltenyi Biotec) sorting on CD11b (Figure 1a),

which has been used by the Barres group [118, 126] and many others [131-134]. The purified microglia are then plated in medium containing cholesterol, M-CSF and TGF- $\beta$ 2. The resulting cultures produced from both wild-type and *LRRK2* mutant mice display the ramified, extended processes indicative of high-quality microglia preparations (Figure 1b-c) [118].

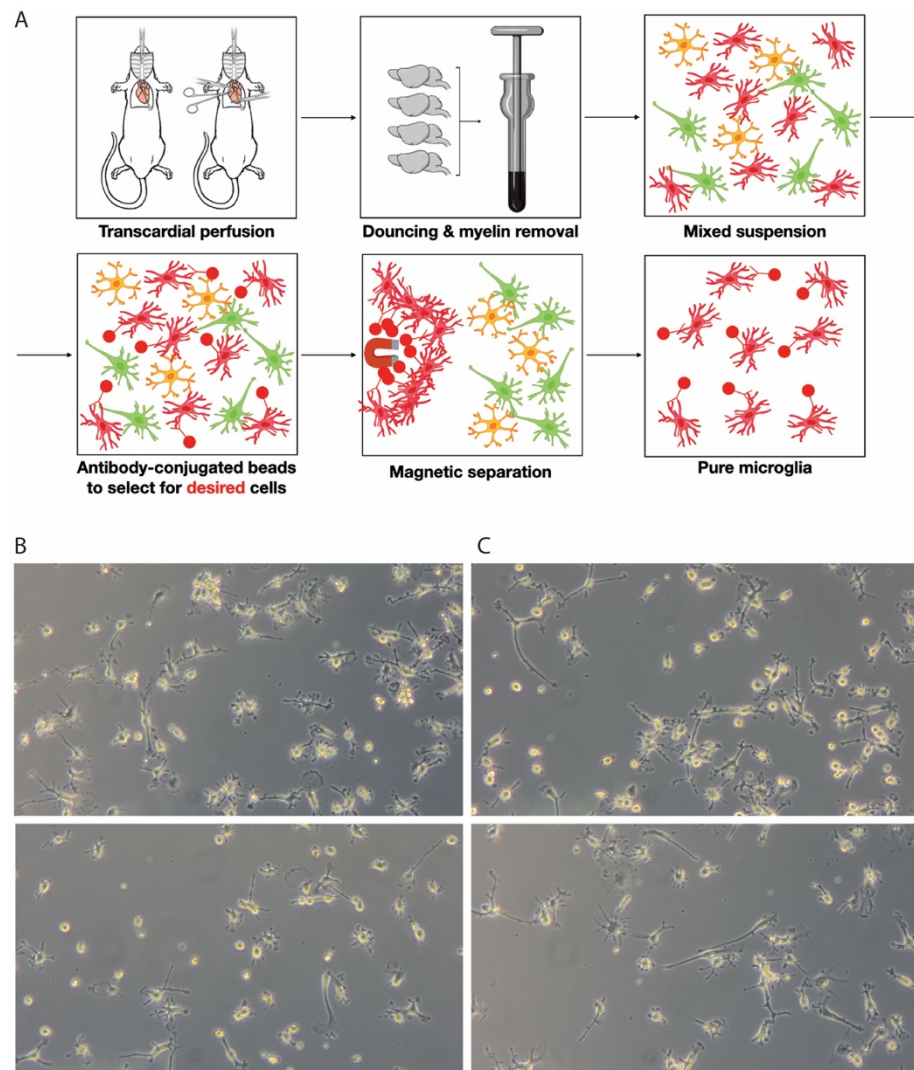


**Figure 1 - Serum-free isolation and culture of primary microglia**

(A) Primary microglia were isolated from neonatal mice by a protocol that includes transcardial perfusion, douncing, myelin removal, and MACS selection for CD11b+ microglia from a mixed CNS suspension. Example brightfield images of (B) wild-type and (C) *LRRK2* G2019S microglia derived from independent biological samples and cultured *in vitro* for 7 days.

To confirm their identity, we further characterized the purified microglia by qPCR and immunofluorescence. In these experiments, we assessed the expression of pan-macrophage



(*PU.1*, *CD11b*, and *CX3CR1*) [135] or microglia-specific (*TMEM119*, *P2RY12*, and *IBA-1*) [136] marker genes. Via qPCR (Figure 2a), we measured the relative expression of *TMEM119*, *P2RY12*, and *PU.1* in samples of wild-type microglia, *LRK2* mutant microglia, wild-type macrophages (purchased from Sciencell Research Laboratories), and a suspension of CNS cells that remained after MACS for CD11b<sup>+</sup> microglia. Supporting their microglial identity, we observed the expression of the microglia-specific markers *TMEM119* and *P2RY12* [118, 126, 137, 138] only in the wild-type and *LRK2* G2019S MACS-purified cells but not in the brain suspension or commercially-sourced macrophages. Importantly, this expression pattern did not hold for *PU.1*, which is expressed across many macrophage subtypes (including microglia) [139-141]. Accordingly, *PU.1* expression was observed in the microglial and macrophage samples, but not in the brain suspension. To further validate the identity of our microglia, we performed immunofluorescence against *IBA-1*, *CX3CR1*, *P2RY12*, and *CD11b* (Figure 2b). In our cultures, we observed positive staining for all of these microglia-expressed proteins, but we did not identify cells that stained for the unrelated markers GFAP (astrocytes) and MAP2 (neurons) (Appendix 6.1, Figure 21), nor did we observe staining with 2<sup>0</sup> antibody alone (Appendix 6.1, Figure 21). Furthermore, when we isolated microglia from a mouse line expressing GFP under a *CX3CR1* promoter [142], we observed GFP expression in live cells after 6 days *in vitro* (Figure 2c). These results suggest that our adaptation of the Barres group microglia isolation and culture protocol was successful, adding to the success that other groups have reported in replicating this approach [127].

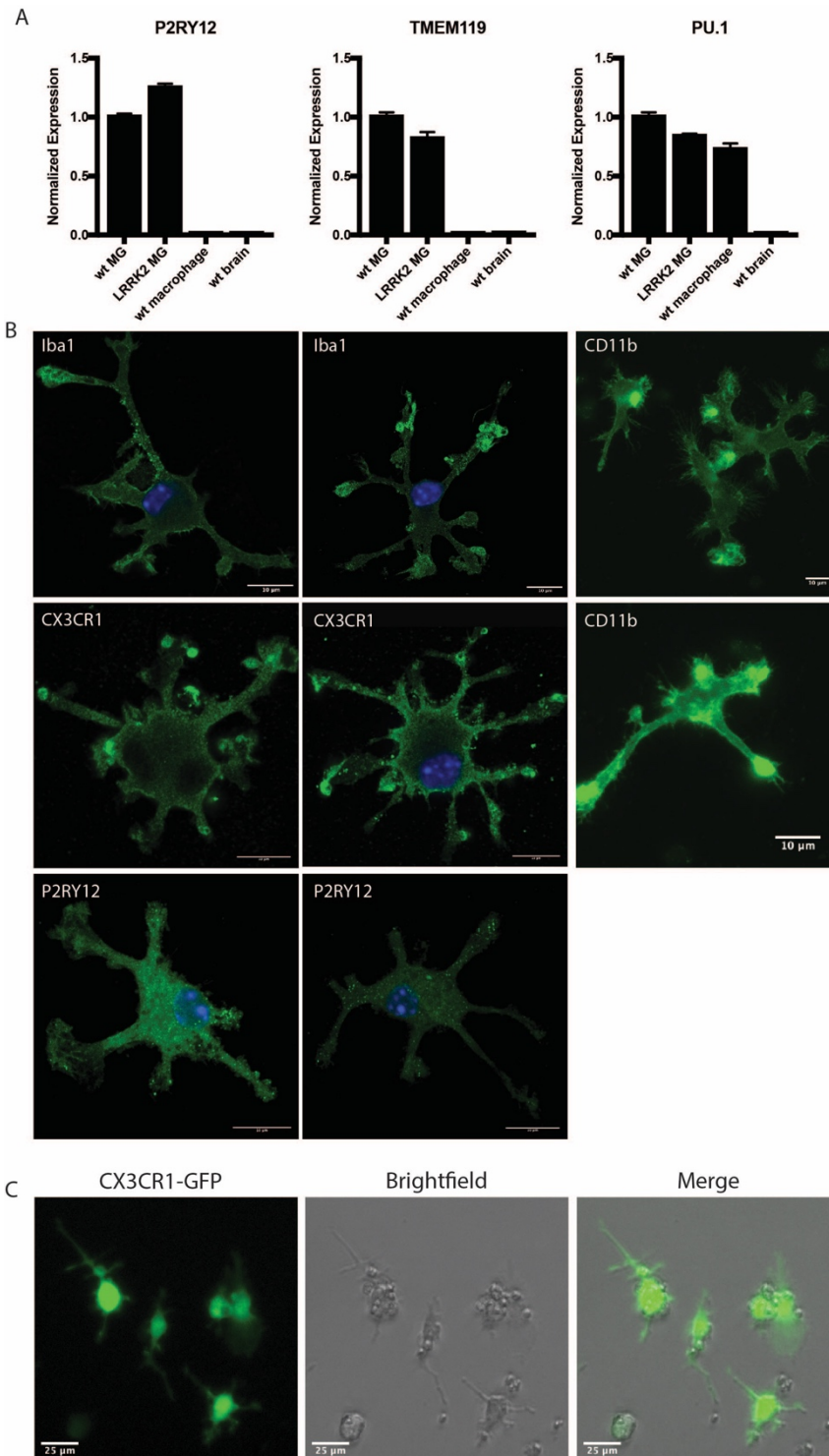


**Figure 2 - Quality control for serum-free microglia**

(A) qPCR results quantifying the relative expression of two microglial markers (P2RY12 and TMEM119) as well as a pan-macrophage marker (PU.1) in wild-type microglia (MG), LRRK2 G2019S microglia, wild-type macrophages, and a wild-type CNS suspension. (B) Immunofluorescence of 7 DIV wild-type microglia against the markers Iba1, CX3CR1, P2RY12, and CD11b. Images of Iba1, CX3CR1, and P2RY12 were acquired with a Zeiss LSM 880 with Airyscan detector using a 63x objective, whereas CD11b images were acquired with an inverted widefield microscope using a 40x objective. (C) Live microglia isolated from a mouse line expressing GFP under a CX3CR1 promoter were imaged at 20X using a Thermo Fisher Evos FL microscope. Error bars are mean  $\pm$  standard error.

## 2.2 Co-culture of primary microglia and midbrain DA neurons

Building on our microglia culture approach, we next combined these microglia with midbrain neurons in a co-culture system that could be used to test our microglia-induced DA neurotoxicity hypothesis. Due to their relevance to Parkinson's disease, primary midbrain neuron isolation and culture techniques are generally mature and well-established, and a wide range of effective protocol variants have been published [143-146].

Our approach for midbrain neuron isolation draws from multiple established protocols. First, we dissect the substantia nigra (SN) region from the ventral midbrain of neonatal mouse pups aged p0-p2. Although embryonic isolation protocols are generally easier to perform, their low (1-2%) content of tyrosine hydroxylase (TH)-positive dopaminergic neurons is insufficient for our experimental aims [146]. In contrast, neonatal SN cultures can contain up to 25% TH-positive DA neurons, with 10-15% being a reasonable goal for most researchers [146]. Following the serum-free isolation and dissociation of neonatal SN tissues, we proceed to the purification of neurons from a mixed SN suspension. Similar to the approach described for microglial purification, we employ MACS to separate neurons from contaminating cell types (Figure 3a). However, whereas microglial purification relies on positive selection by binding the CD11b cell surface receptor, MACS neuronal purification uses negative selection to bind undesired cells (astrocytes, oligodendrocytes, microglia, endothelial cells, and fibroblasts) in the SN suspension, allowing neurons to elute freely [147]. These eluted neurons are then plated in defined, serum-free medium that contains recombinant brain-derived neurotrophic factor (BDNF), glia-derived neurotrophic factor (GDNF), and transforming growth factor  $\beta$ 3 (TGF- $\beta$ 3), which have been demonstrated to support the survival of dopaminergic neurons *in vitro* [125]. To prevent the

outgrowth of any trace non-neuronal cell types that might carry over during MACS purification, the neuronal cultures are transiently treated with 5-Fluoro-2'-deoxyuridine (5-FDU), an anti-mitotic drug that removes proliferating cells—including glia and fibroblasts—but maintains the non-mitotic neurons in primary culture [143, 148]. Following 5-FDU treatment, the midbrain neuron cultures are returned to basal medium and incubated for a period of days or weeks until experiments are performed.

To assess the midbrain cultures, routine immunofluorescence analyses were performed (Figure 3b). As mentioned above, expression of tyrosine hydroxylase—the enzyme that catalyzes the conversion L-tyrosine to the dopamine precursor L-3,4-dihydroxyphenylalanine (L-DOPA) [149]—is the standard marker of dopaminergic neurons [150]. In contrast to TH, the microtubule-associated protein MAP2 is a neuron-specific (but not DA-specific) marker that is well-expressed in the soma and dendrites of post-mitotic neurons [151]. As shown in Figure 3b, our midbrain cultures display the characteristic neuronal expression of MAP2, as well as the expression of TH in a subset of these neurons. The co-staining of MAP2 and TH will be used extensively in later analyses, as the absolute number of MAP2+ cells and the ratio of TH+ to MAP2+ cells provides a metric for assessing the survival of dopaminergic and non-dopaminergic neurons in varying conditions [152-154]. In addition to expressing both MAP2 and TH, the primary midbrain neurons extend processes on the scale of hundreds of microns, as has been observed in similar primary cultures [145, 146]. When they are combined *in vitro* with primary microglia, these SN-derived neuronal cultures can be used to test our DA neurotoxicity hypothesis.

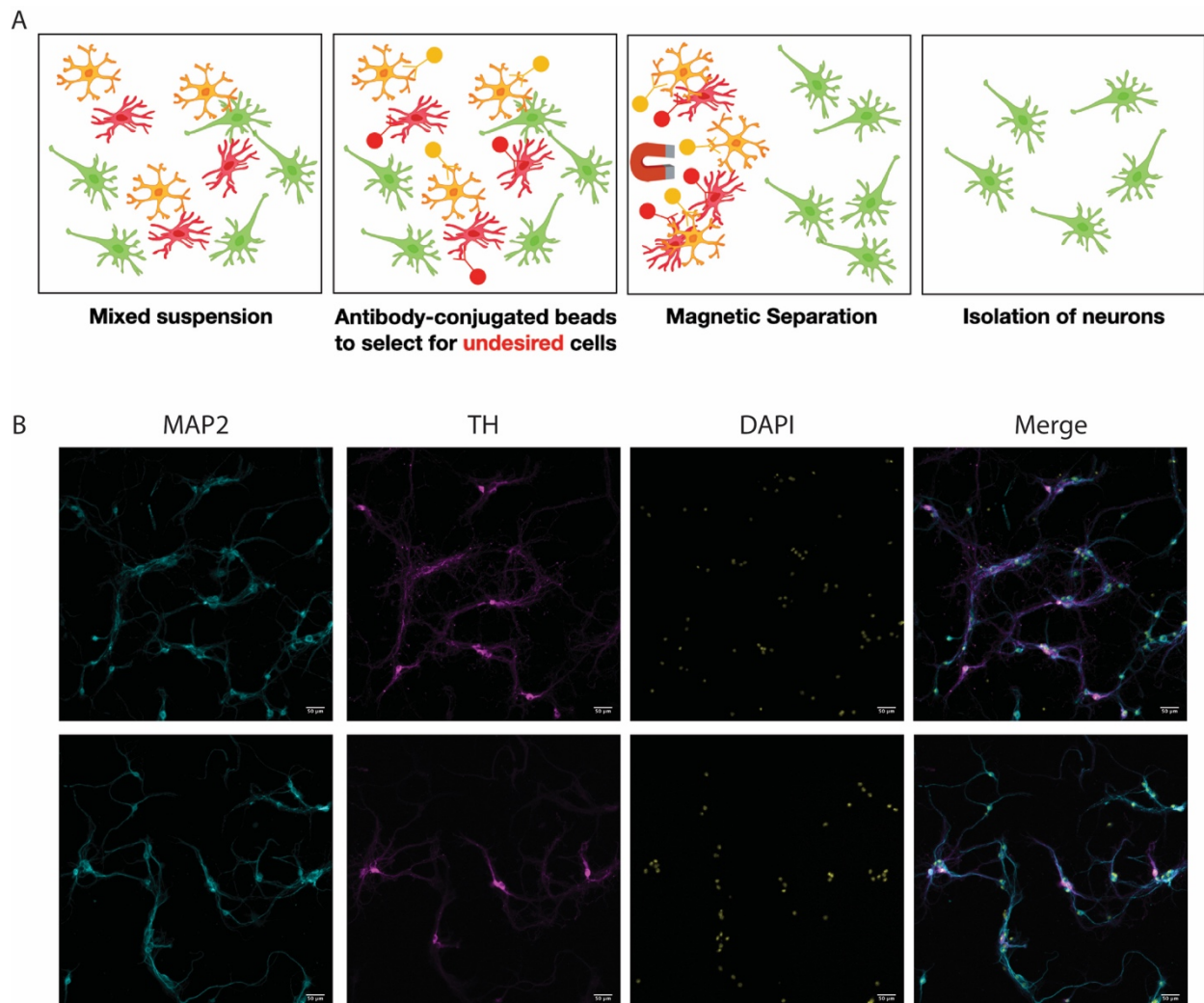


**Figure 3 - Midbrain neuron isolation and culture**

(A) Strategy for the MACS purification of neurons from a mixed suspension of midbrain cells. In contrast to microglial MACS isolation (Figure 1), MACS neuron isolation employs negative selection. (B) Representative IF images of 14 DIV midbrain neurons stained for the MAP2 (pan-neuronal) and TH (dopaminergic) neuronal markers. Images were acquired at 10x on a Nikon Eclipse Ti inverted widefield microscope.

Following the preparation of midbrain neurons from neonatal pups, freshly-isolated microglia can be directly added to produce neuron-microglia co-cultures. In this system, MACS-purified midbrain neurons are plated on D0, followed by transient treatment with 5-FDU for 12h on the following day (D1) (Figure 4a). Once the midbrain neuron cultures are returned to basal medium, they are incubated for a further two days to allow for post-5-FDU recovery. On

D3, microglia are isolated from neonatal mice as described previously using serum-free techniques. The MACS-purified microglia are then added to the midbrain neuronal cultures in a 1:1 microglia: neuron ratio in an equal volume of serum-free microglia growth medium (relative to serum-free neuronal culture medium), for a final media ratio of 1:1. Following the addition of microglia to the neuronal culture, the neuron-microglia co-culture is incubated for 7 days prior

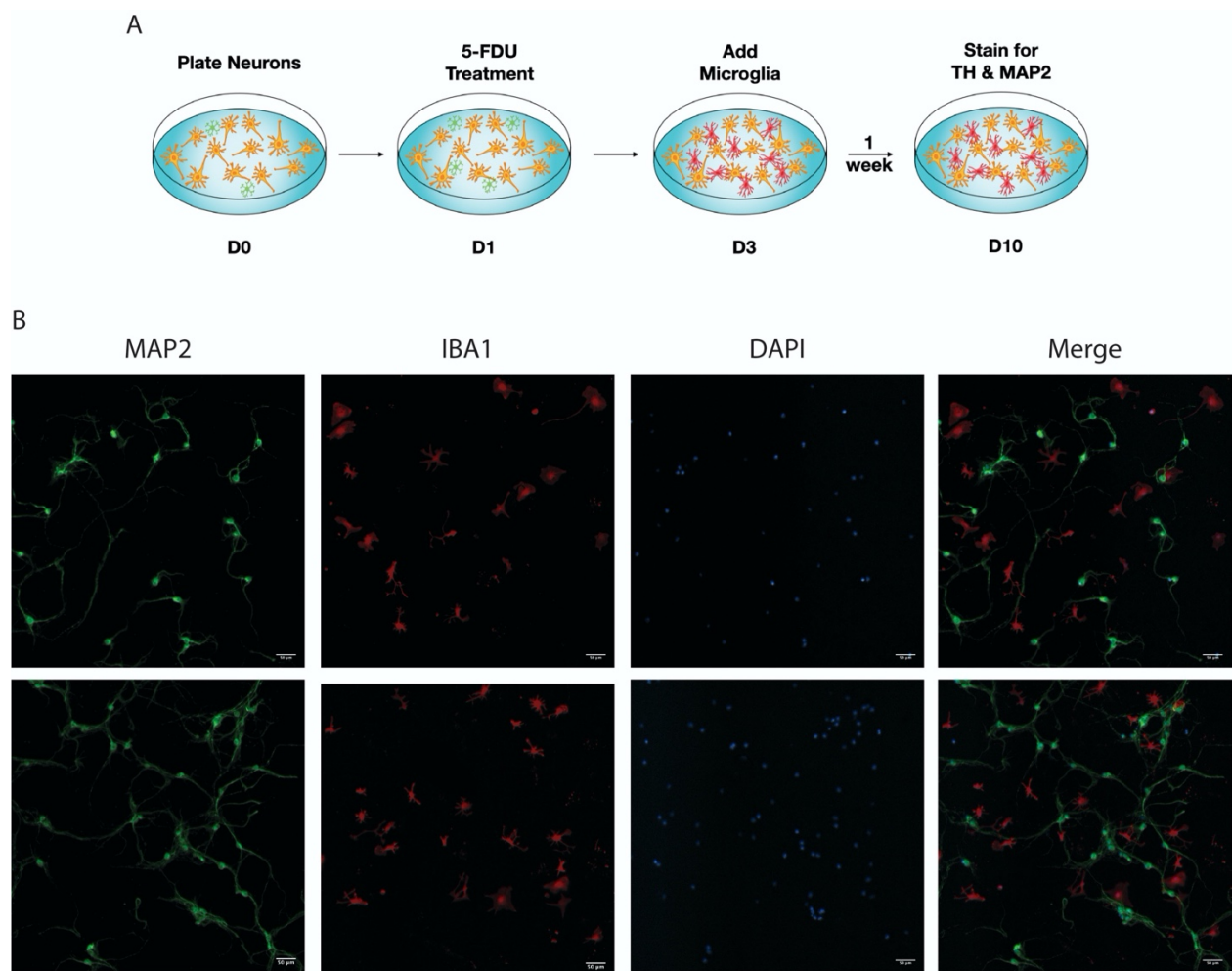


**Figure 4 - Coculture of primary midbrain neurons and microglia**

(A) Workflow for neuron-microglia co-culture experiments. Midbrain neurons were isolated and plated on D0 and treated for 12h with 15  $\mu$ M 5-FDU. Freshly-isolated microglia were added to neuronal cultures on D3, and co-cultures are fixed and stained on D10. (B) Representative images of neuron-microglia co-cultures fixed and stained on D10 for MAP2 (neurons) and Iba1 (microglia). Images were collected on a Nikon Eclipse Ti inverted widefield microscope, and quantification of MAP2, Iba1, and DAPI channels demonstrated that co-cultures are composed of 96.4% ( $\pm$ 2.2%; 95% CI of the mean; 4 replicates) neurons and microglia.

to fixation and analysis via immunofluorescence. As shown in Figure 4b, the co-cultures display robust neuronal expression of MAP2, as well as expression of the standard microglial marker IBA1. To assess the purity of neurons and microglia in our co-cultures, we calculated the number of MAP2+ and IBA+ cells that colocalized with live (DAPI+) nuclei as a percentage of the total number of live (DAPI+) nuclei in the image. Based on this metric, 96.4% ( $\pm 2.2\%$ ; 95% CI of the mean; 4 replicates) of the cells in our cultures are either neurons or microglia, indicating that our approach produces very pure co-cultures that compare favorably with published primary cultures [34, 146, 155]. Although this co-culture is quite pure, we must note that any level of neuron-microglia purity below 100% allows for the possibility—though unlikely—of neurotoxicity effects being partially dependent on the presence of trace levels of other cell types (*e.g.* astrocytes, oligodendrocytes, endothelial cells). Keeping this in mind, we moved forward to test our hypothesis of microglia-mediated dopaminergic neurotoxicity.

### **2.3 LRRK2 G2019S microglia induce DA neurotoxicity in a co-culture model**

In the Introduction (Chapter 1.5), we introduced our hypothesis that **LRRK2 G2019S mutation-carrying microglia promote dopaminergic neurotoxicity**, and the approaches outlined above enable us to directly test this hypothesis. Because we must control for any cell-autonomous malfunction caused by the LRRK2 G2019S mutation in neurons [119, 156, 157], the independent isolation of genotype-controlled neurons and microglia is crucial to testing this hypothesis. The cartoons in Figure 5 depict our co-culture strategy, wherein the double-wildtype (wild-type microglia + wildtype midbrain neuron co-culture) represents the control condition, and the pivotal comparison is between the double-wildtype and the mutant microglia (LRRK2 G2019S microglia + wildtype midbrain neuron co-culture) conditions. In

addition, we also set out to assess the magnitude of cell-autonomous neuronal toxicity (if any) induced by the G2019S mutation in neurons co-cultured with wild-type microglia. Although similar work that assessed the DA neurotoxicity induced by human *LRRK2* G2019S mutant astrocytes did not include this additional comparison [119], we reasoned that any microglia-induced toxicity that we observed would be less physiologically and therapeutically relevant if the *LRRK2* mutation in neurons induced much greater DA neurotoxicity. Therefore, we set out to assess DA neuron survival in these three conditions.

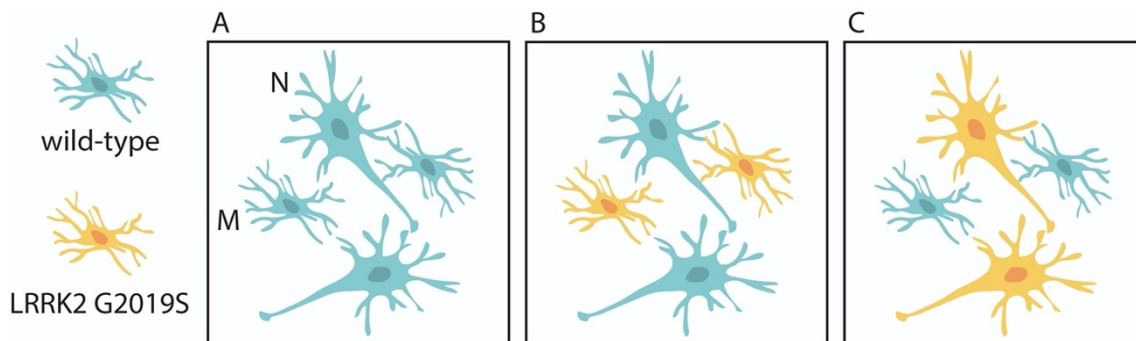


**Figure 5 - Genotype-specific neuron and microglia combinations in co-culture**

The experimental design for our three genotype-controlled co-culture conditions. Wild-type cells are depicted in blue, and *LRRK2* G2019S mutant cells are depicted in orange. “N” is a midbrain neuron, whereas “M” is a microglial cell. The three conditions are as follows: A) wild-type neurons with wild-type microglia, B) wild-type neurons with *LRRK2* G2019S microglia, and C) *LRRK2* G2019S neurons with wild-type microglia.

Following the addition of wild-type or *LRRK2* G2019S microglia to the appropriate midbrain neuron cultures, the co-cultures were incubated for 7 days prior to fixation and immunofluorescence staining against MAP2 and TH. As mentioned previously, MAP2 labels all neurons in the culture, whereas TH only labels dopaminergic neurons, so the ratio of TH+ to MAP2+ cells provides a metric for DA neuron survival [152-154]. To image thousands of cells per technical replicate, we utilized a Nikon Eclipse Ti inverted widefield microscope (Nikon



Corporation) equipped with a Perfect Focus System to tile the entirety of each well of our co-culture experiments at 10X magnification. Figure 6a shows a tiled composite image of a standard co-culture well in both the MAP2 (red) and TH (green) channels. In Figure 6b, 280  $\mu\text{m}$  x 280  $\mu\text{m}$  sub-images from a typical co-culture experiment are shown. In these examples, wild-type neurons were cultured with either wild-type or *LRRK2* G2019S microglia. Quantitative results cannot be obtained from analyzing an individual 280  $\mu\text{m}$  x 280  $\mu\text{m}$  sub-image, but in this example, the ratio of TH+ to MAP2+ neuronal soma appears to be lower in the co-culture with *LRRK2* G2019S microglia.

To perform a quantitative analysis, we used the Imaris (Oxford Instruments) image analysis platform to identify MAP2+ neuronal soma and the subset of MAP2+/TH+ dopaminergic neurons. From these analyses, we obtained the total number of MAP2+ neurons and the number of TH+ dopaminergic neurons in every well. With these values, we calculated the percentage of TH+ dopaminergic neurons in the pivotal double-wildtype and wildtype neuron + *LRRK2* G2019S microglia conditions (Figure 6c). Across multiple biological repeats, we observed a significant and robust decrease in the percentage of neurons that were TH+ when wildtype neurons were co-cultured with *LRRK2* G2019S microglia (compared to wildtype microglia). More specifically, we observed decreases in the ratio of TH neurons of  $20.6\% \pm 4.8\%$  (standard error of difference between means),  $27.1\% \pm 3.4\%$ , and  $23.5\% \pm 2.9\%$  in co-cultures

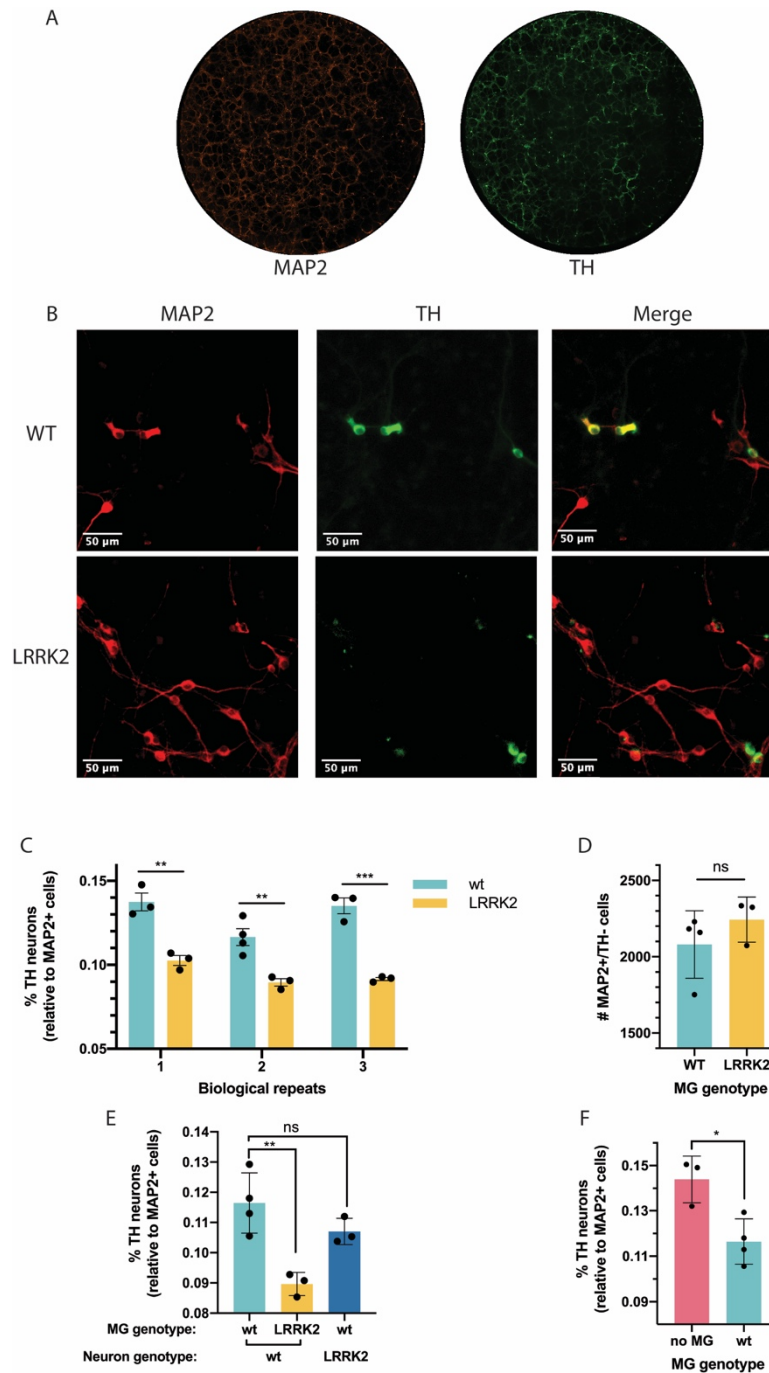


**Figure 6 - Microglia genotype-dependent DA neurotoxicity**

Full neuron-microglia co-culture wells were imaged at 10x on a Nikon Eclipse Ti inverted widefield microscope equipped with the Nikon Perfect Focus System. (a) A typical large-field, tiled image in the MAP2 and TH channels. (b) Example images of wild-type neurons co-cultured with either wild-type (top) or LRRK2 G2019S (bottom) microglia. (c) Quantification of 3 biological replicates evaluating wild-type TH dopaminergic neuron survival in co-culture with either wild-type or LRRK2 mutant microglia. (d) Quantification of the number of non-DA neurons in co-cultures of wild-type neurons with either wild-type or LRRK2 G2019S microglia. (e) Comparison of wild-type and LRRK2 G2019S TH neuron survival in co-culture with microglia. (f) The effect of co-culture on TH neuron survival. Statistical tests: two-sided Student's t-test (c, d, f) and one-way ANOVA with Tukey's post hoc test (e). \* $P < 0.05$ , \*\* $P < 0.01$ , \*\*\* $P < 0.001$ , ns = not significant. Error bars are mean  $\pm$  standard error.

with *LRRK2* mutant microglia. Importantly, the number of non-dopaminergic (MAP2+/TH-)

neurons did not change in response to microglia genotype (Figure 6d), which suggests that the loss of neurons is specific to DA neurons, whose death is the hallmark of Parkinson's disease.

Not only do *LRRK2* G2019S microglia cause DA-specific neurotoxicity in our co-culture system, but this *LRRK2* mutation-dependent toxicity appears to be specific to microglia. In a comparison of TH neuron survival between the two conditions depicted in Figure 5a and Figure 5c—where the microglial genotype is constant but the neuronal genotype differs—midbrain neurons carrying the *LRRK2* G2019S mutation do not display significant DA neuron loss in co-culture with wild-type microglia (Figure 6e). In addition to these experimental co-culture conditions, we also assessed the effect of co-culture itself on DA neuron survival, and we observed moderate DA neurotoxicity upon addition of microglia (in comparison to a pure midbrain neuronal culture; Figure 6f). This effect was not surprising, as published work has described varying levels of toxicity associated with the addition of either microglia or microglia-conditioned medium (MCM) to neuronal cultures [158-161].

In sum, our results confirm the hypothesis that **LRRK2 G2019S mutation-carrying microglia promote dopaminergic neurotoxicity**. However, the underlying mechanism of this neurotoxicity remains unclear, and in particular we do not understand *how* DA neurons die when they are co-cultured with *LRRK2* G2019S microglia. Do *LRRK2* G2019S microglia behave in a way that actively *kills* DA neurons that would otherwise survive in the presence of wild-type microglia, or do these *LRRK2* mutant microglia instead fail to provide DA neurons with support (*e.g.* neurotrophic factors) that wild-type microglia provide? Based on precedents in the literature, either hypothesis is viable. In the Introduction (Chapter 1.2.3), we reviewed examples of microglia-induced neurotoxicity that fall into both categories. Microglia have been

shown to actively kill neurons by secreting pro-apoptotic cathepsin B, TNF $\alpha$  and Fas ligand, and reactive oxygen and nitrogen species [41-43], and they can also kill healthy neurons through direct phagocytosis (or 'phagoptosis') [34]. In contrast, microglial failure to secrete proteins including BDNF, IGF1, and TGF- $\beta$ 2 can result in the death of neurons [38, 44, 162]. If we consider these potential mechanisms of microglia-induced neuronal death, there appears to be another approach to assessing the observed toxicity: is neuronal death dependent on direct neuron-microglia contact (as in 'phagoptosis'), or are soluble factors (or a lack thereof) sufficient to mediate neuronal toxicity? With the aim of more precisely understanding the neurotoxicity observed in our co-culture system, we use a conditioned medium approach to address this question in Section 2.4.

#### **2.4 LRRK2 G2019S microglia-conditioned medium induces DA neurotoxicity**

To assess the contribution of soluble factors (as opposed to direct neuron-microglia contact) to the observed neurotoxicity, we designed conditioned medium experiments. In these experiments, we applied the culture media of genotype-specific microglial monocultures to neuronal monocultures (Figure 7), and we evaluated the effects (if any) on neuronal monocultures. More specifically, we prepared monocultures of either wild-type or *LRRK2* G2019S microglia as described previously, and we collected genotype-specific microglia conditioned medium (MCM) from each culture after 6 DIV. Separately, monocultures of wild-type midbrain neurons were prepared, and we added the MCM from either genotype to the neuronal monocultures. Similar to the co-culture experiments, the final culture medium was composed of equal volumes of neuronal and microglia media. After 1 week of incubation, the

MCM-treated neuronal cultures were fixed and stained for TH and MAP2 as described previously.

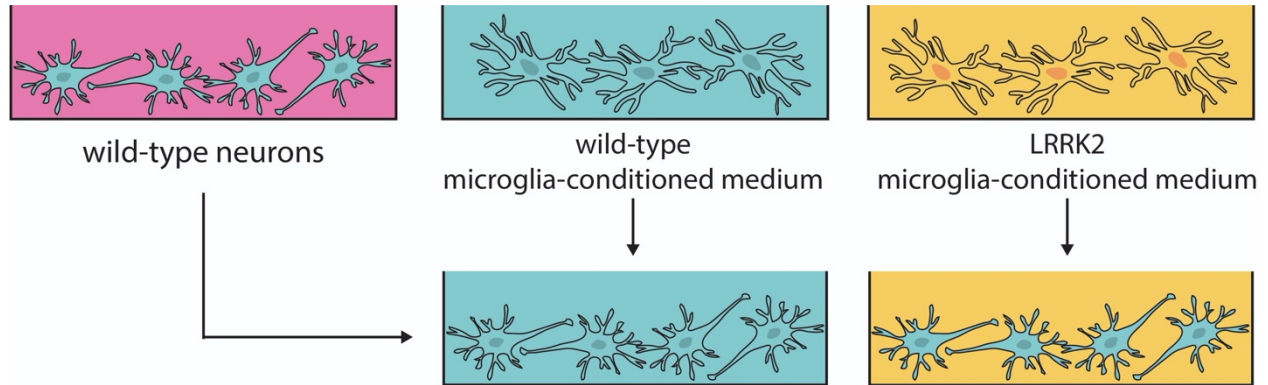


**Figure 7 - Design of conditioned medium experiments**

In conditioned medium experiments, monocultures of wild-type midbrain neurons, wild-type microglia, and *LRRK2* G2019S microglia are prepared (top row). Conditioned medium is collected from wild-type (blue) and *LRRK2* (yellow) microglial monocultures and added to the midbrain neuronal monocultures (bottom row). Neuron wells in the bottom row are depicted with only microglia conditioned medium for simplicity, but these conditioned medium neuron cultures contain a 1:1 mixture of neuronal medium and MCM.

As with the co-culture experiments, we collected large-field, tiled images of entire MCM culture wells using a microscope equipped with Nikon's Perfect Focus System. Figure 8a shows typical examples of midbrain neurons cultured with either wild-type or *LRRK2* G2019S MCM. Using Imaris software, we again identified all MAP2+ neurons as well as the subset of MAP2+/TH+ dopaminergic neurons in every condition. Similar to the co-culture experiments, we observed a robust decrease in the percentage of TH+ neurons when wildtype neurons were cultured in *LRRK2* G2019S MCM (compared to wildtype MCM). Across these repeats, we recorded decreases in the ratio of TH neurons of  $15.6\% \pm 3.7\%$  (standard error of difference between means),  $13.8\% \pm 2.0\%$ , and  $14.2\% \pm 4.5\%$  in neuronal cultures with *LRRK2* mutant MCM (Figure 8b). Again, the number of non-dopaminergic (MAP2+/TH-) neurons was not

affected by the MCM genotype, suggesting the specific loss of DA neurons in these experiments (Figure 8c). Similar to the co-culture, we observed moderate toxicity associated with the addition of conditioned medium to the neuronal cultures (Figure 8c), as has been observed in previous studies of primary microglia [158-160].

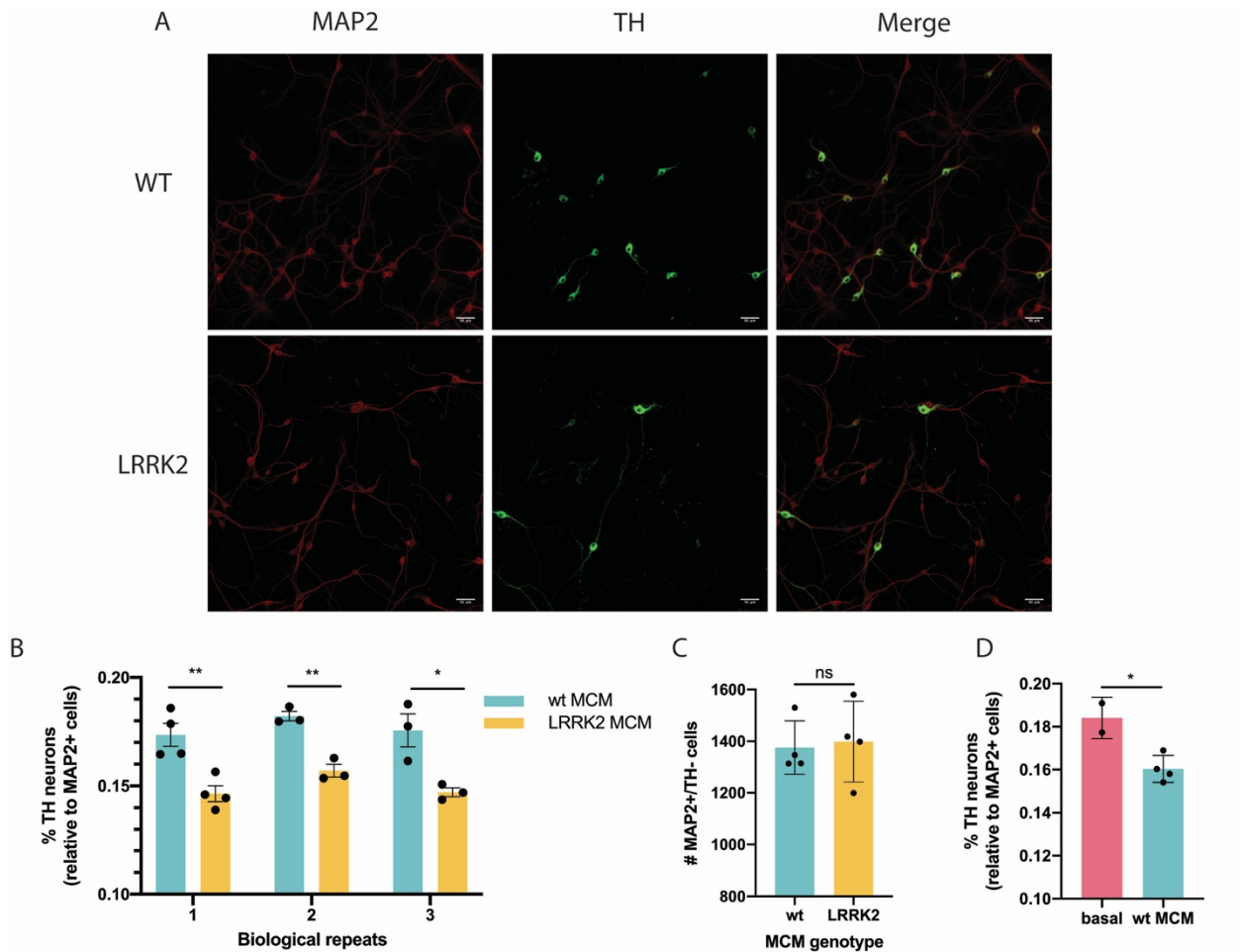


**Figure 8 - LRRK2 G2019S microglia conditioned medium causes DA neurotoxicity**

(a) Example images of wild-type neurons treated with conditioned medium from wild-type microglia ('WT') or LRRK2 G2019S microglia ('LRRK2'). Immunofluorescence from MAP2/TH and image acquisition were carried out as described in Figure 6. (b) Quantification of 3 biological replicates evaluating wild-type TH dopaminergic neuron survival in monoculture with either wild-type or LRRK2 G2019S MCM. (c) Quantification of the number of non-DA neurons in midbrain monocultures treated with either wild-type or LRRK2 G2019S MCM. (d) The effect of MCM addition on TH neuron survival in monoculture. Statistical tests: two-sided Student's t-test (b, c, d). \* $P < 0.05$ , \*\* $P < 0.01$ , ns = not significant. Error bars are mean  $\pm$  standard error.

Taken together, our results suggest that soluble factors contribute to the microglia-induced neurotoxicity reported in Chapter 2.3. Considering the strong precedent for microglia-secreted proteins (or a lack thereof) in neurotoxicity [38, 41-44, 162], this result is not a significant surprise. However, our work adds to the body of literature suggesting that microglia can kill (or fail to support) neurons at a distance, without the requirement for direct physical contact between microglia in neurons. Our data do not, however, conclusively rule out the possibility of additional contact-dependent neurotoxicity that contributes to DA loss in co-cultures with *LRRK2* mutant microglia. Relative to the wild-type microglia conditions, the *LRRK2* co-cultures displayed decreases in the ratio of TH+ neurons of 20.6%-27.1% ( $\pm 4.8\%$ ) across biological repeats, whereas the *LRRK2* MCM caused decreases of 13.8-15.6% ( $\pm 4.5\%$ ). These results suggest that the conditioned medium experiments do not fully recapitulate the level of neurotoxicity observed in the direct co-culture, leaving open the possibility of contact-dependent processes—such as the aforementioned ‘phagoptosis’—contributing to the observed neurotoxicity. Future work could assess the contribution of phagocytosis-dependent neurotoxicity, but these results nonetheless demonstrate that *LRRK2* mutant MCM can cause DA neurotoxicity.

The observation of *LRRK2* MCM-induced neurotoxicity naturally begs the question of which component(s) of *LRRK2* MCM are responsible for the loss of DA neurons. In previous studies, researchers have employed medium-throughput cytokine arrays to identify secreted proteins whose levels are dramatically altered across two or more MCM samples [9]. These commercially available arrays (R&D Systems) are membrane-based sandwich immunoassays, where conditioned medium is incubated over a membrane spotted with capture antibodies

against 111 cytokines, and the level of each cytokine can be measured following the addition of chemiluminescent detection antibodies. Generally, only large-fold changes (*e.g.* 15-fold or higher) in the signal of a given cytokine across the experimental conditions are considered ‘hits’ in this type of MCM chemiluminescent assay [9, 163]. When we performed this immunoassay using biological repeats of wild-type and *LRRK2* G2019S MCM preparations, we obtained quantifiable chemiluminescence data (Figure 9a). However, analysis of these blots revealed no

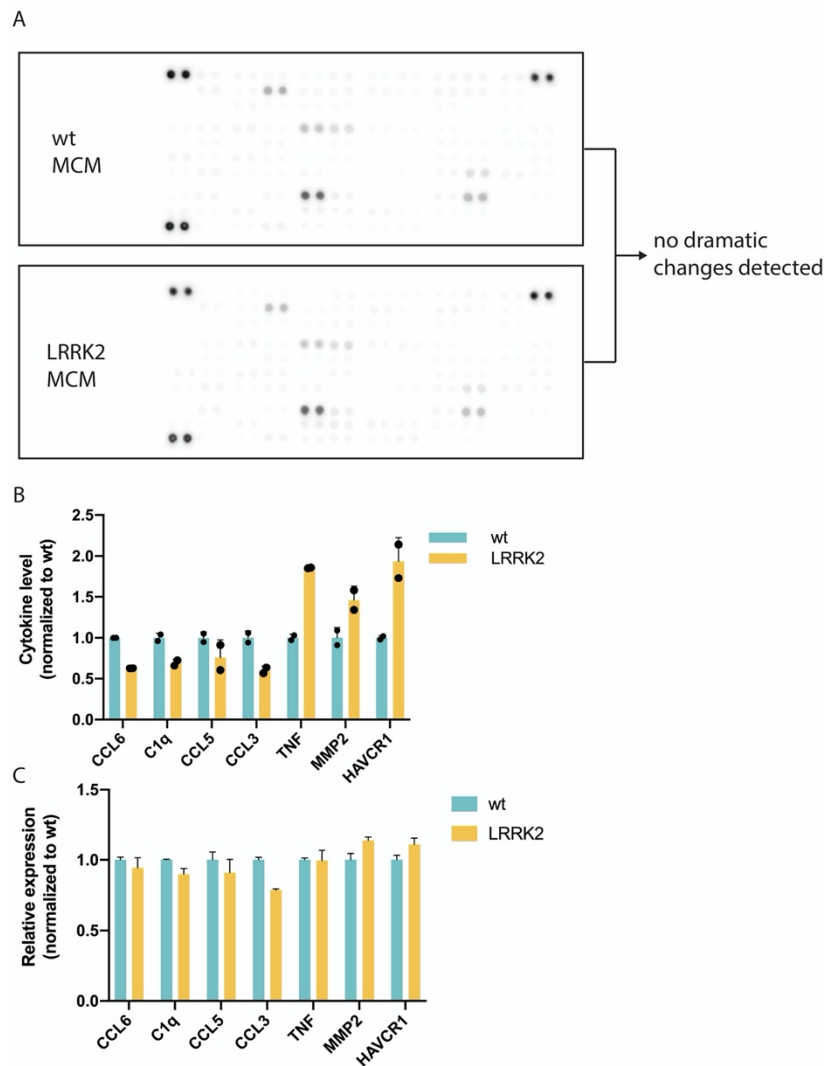


**Figure 9 - Analysis of MCM cytokine levels is inconclusive**

The levels of 111 cytokines/chemokines in conditioned medium collected from wild-type and *LRRK2* G2019S microglia were evaluated using membrane-based sandwich immunoassays. Example blots are shown in (a), and no substantial genotype-dependent changes in cytokine levels were detected. (b) A limited number of cytokines displayed minimal fold-changes (~0.7-1.9) that would not be considered ‘hits’ in such immunoassays, and (c) qPCR of these targets showed minimal changes in their gene expression. Error bars are mean  $\pm$  standard error.



dramatic changes in any of the 111 cytokines that were measured. A number of cytokines showed fold-changes in the range of 0.5-0.7 (decreased in *LRRK2* MCM) or 1.5-2.0 (increased in *LRRK2* MCM) in this assay (Figure 9b). Subtle fold-changes in this range are not expected to be physiologically relevant to inflammatory responses, and upon measurement of relative gene expression in primary microglia by qPCR, these same 7 cytokines showed very little difference between wild-type and *LRRK2* G2019S microglia (Figure 9c). As such, our data suggest that the levels of 111 cytokines profiled here (full list is in Appendix 6.1, Table 2) are not dramatically different across our genotype-specific MCM samples.

Although our initial attempts to identify candidate factors underlying *LRRK2* G2019S MCM-induced neurotoxicity were unsuccessful, we believe that future work could pin down the source(s) of toxicity. In an effort to more precisely define the composition of the wild-type vs. *LRRK2* mutant conditioned media, researchers could perform quantitative mass spectrometry (MS) on either type of MCM to more directly measure the level of each protein present in the medium. This mass spectrometry “secretomics” approach has gained prevalence in recent years [164-166], and our serum-free cultures are ideal for this experimental approach (as the presence of serum significantly confounds the interpretation of MS results). Although secreted proteins are likely candidates for microglia-associated neurotoxicity, microglia-released microvesicles and exosomes have also been linked to inflammatory and neurodegenerative phenotypes [167-171]. To test these options, differential ultracentrifugation could be performed to purify exosomes and microvesicles from MCM samples, and the effects of these genotype-specific exosomes and microvesicles on DA neuron survival could be assessed. As

such, our failed attempt to detect the neurotoxic factor(s) present (or lacking) in *LRRK2* G2019S MCM does not preclude the possibility that future work will identify those factors.

## 2.5 Chapter Summary

In this chapter, we confirmed the core hypothesis of microglia-induced DA neurotoxicity and performed additional experiments that attempted to clarify aspects of the underlying neurotoxicity. More specifically, we tested the hypothesis that ***LRRK2* G2019S mutation-carrying microglia promote dopaminergic neurotoxicity** by developing a neuron-microglia culture system that enabled us to control the genotype of either cell type in a co-culture format. Using that system, we observed a significant and robust decrease in the survival of wild-type TH+ dopaminergic neurons in the presence of *LRRK2* G2019S microglia (compared to wild-type microglia). This effect was specific to DA neurons. Our results immediately begged the question of *how* this neurotoxicity might be mediated, so we designed MCM experiments to test the hypothesis that factors released by microglia into the culture medium contribute to DA neurotoxicity. Indeed, we observed a significant decrease in TH+ DA neuron survival in the presence of *LRRK2* G2019S MCM. However, this DA neuron loss was not as drastic as that observed in the co-culture, leaving open the possibility of add-on toxicity mediated by physical contact between neurons and microglia. To identify the factor(s) responsible for *LRRK2* MCM neurotoxicity, we measured the levels of 111 cytokines using membrane immunoassays, and we performed qPCR on a subset of cytokines of interest. These efforts did not identify any factor(s) with substantially altered secretion and/or gene expression, but we are optimistic that future efforts could identify soluble factors and/or exosomes and microvesicles that contribute

to MCM-mediated neurotoxicity. However, aside from these questions regarding the immediate cause of neurotoxicity, a few major outstanding questions demand attention.

First is the question of specificity. That is: why do dopaminergic neurons die in co-culture or MCM experiments with LRRK2 G2019S microglia, but non-dopaminergic neurons do not? Before addressing this question directly, we need to clarify the underlying assumption that all other subtypes of neurons are unaffected. Though we do not observe significant changes in the overall number of non-DA neurons (Figure 6d and Figure 8c), it is possible that non-abundant neuron subtypes in the midbrain—for example serotonergic neurons [144]—are affected, but we did not measure each subtype directly. Significant losses of abundant subtypes like GABAergic and glutamatergic neurons, which together account for up to 80% of neurons in some published midbrain cultures [144], would likely be captured in our non-DA neuron survival measurements. But it is possible that drastic losses of already-scarce serotonergic neurons—which represented just 1% of neurons in one study's midbrain cultures [144]—would go undetected in our bulk non-DA neuron measurements. Although we believe this outcome is unlikely due to the strong links established between LRRK2, PD, and DA neurons over decades of research, we have not fully ruled out this possibility.

However, the question of DA neuron specificity still remains, as we do not observe major losses of non-DA neurons in our experiments. Although we have not carried out experiments related to DA neuron specificity, previous work in the literature provides evidence for a simple hypothesis. Historically, there has been a strong focus on mitochondrial and metabolic function in PD-associated DA neurons because of their acute and specific sensitivity to the mitochondrial toxins MPTP (which causes Parkinsonism in humans) [172] and rotenone

[173, 174], as well as genetic links between PD and the mitochondria-associated proteins Parkin and PINK1 [175]. Building on these precedents, subsequent work has demonstrated that SN DA neurons likely have greater metabolic needs than other neuron types. Some reasons for these increased metabolic needs are SN DA neurons' intrinsic  $\text{Ca}^{2+}$ -dependent pacemaking activity [175], which requires energetically-demanding synaptic transmission and results in increased cytosolic  $\text{Ca}^{2+}$  and elevated oxidative stress [176]; low capacity for  $\text{Ca}^{2+}$  buffering, which makes them susceptible to spike afterhyperpolarizations and subthreshold firing [177]; uniquely large axonal arbors that likely have extensive metabolic demands [178]; and lack of axonal myelination [179], which likely increases the energetic requirements of synaptic transmission in SN DA neurons [180]. Furthermore, the dopamine metabolism pathway is known to produce reactive oxygen species that increase oxidative stress and impair mitochondrial activity [181].

Taken together, these high demands could leave SN DA neurons walking a metabolic tightrope, with reduced oxidative reserve capacity and increased production of damaging superoxides in even the best conditions [182]. These factors may make DA neurons particularly vulnerable to extrinsic stressors—such as malfunctions in their glial 'support' cells—that could disrupt the SN DA neurons' homeostasis. Based on our knowledge of SN DA neurons, then, a simple hypothesis may explain the DA neuron specificity that we observe in culture: LRRK2 G2019S microglia add generic stress to the system (via toxic secreted factors, withdrawal of neurotrophic factors, or contact-dependent pathways), and SN DA neurons die because they are simply more sensitive to such stressors.

In addition to the intrinsic sensitivity of DA neurons, the enrichment of microglia in the substantia nigra has been reported in the literature. For example, in the corpus callosum and

cerebral cortex, microglia represent just 5% of all cells, whereas in the substantia nigra—the most microglia-enriched tissue that was analyzed—this proportion rises to 12% [183]. Similar work has also identified the SN as the most microglia-enriched region of the brain (among the 22 tissues that were dissected) [184]. Although there are dopaminergic neurons in many regions of the CNS, these observations provide another potential axis of specificity: the regional abundance of microglia. If DA neurons are particularly sensitive to disruptions in homeostasis, and if the SN is uniquely enriched in microglia to begin with, then the dramatic loss of SN DA neurons in PD (~60% in human patients [59]) could be linked—in part—to *LRRK2* G2019S microglial malfunction in PD patients. We do not set out to test this high-level hypothesis, and there are many other hypotheses that one could generate to explain the specific loss of DA neurons. However, this relatively straightforward hypothesis highlights the potential for simple biological processes to underlie the cell-type-specific pathology of Parkinson's disease. In addition, it raises an interesting question that we will begin to address in the next chapter: what, if anything, is intrinsically different about the function and cell biology of *LRRK2* G2019S microglia?

### **3 RESULTS PART 2: Characterization of cell-autonomous changes in LRRK2 G2019S microglia**

In the previous chapter, we focused on DA neuron survival and the MCM-carried factors that could impact DA neuron health, and we analyzed *LRRK2* G2019S microglia mainly as an extrinsic stressor that could negatively affect DA neurons. In this chapter, we focus solely on microglia. In particular, we were interested in better understanding microglial functions and cell biological processes that differ across the wild-type and *LRRK2* G2019S genotypes. Drawing on our understanding of core microglial activities, neurodegeneration-associated microglial pathologies, and the abundant literature describing *LRRK2*-associated cell biological pathways (which were reviewed in Chapter 1.3), we set out to characterize wild-type and *LRRK2* G2019S microglia across three broad regimes: 1) the metabolic organelles, including mitochondria and lipid droplets, 2) phagocytosis and the endolysosomal pathway, and 3) migration, chemotaxis, and cytoskeletal dynamics. There are many other microglial functions and cell biological processes that would be promising to investigate, but we hope that the characterization provided here provides a starting point for understanding of the microglia-intrinsic effects of the *LRRK2* G2019S mutation.

#### **3.1 Metabolic organelles: mitochondrial and lipid droplet morphology**

As reviewed in the Introduction (Chapter 1.3.4), a significant body of work has linked *LRRK2* to the regulation of metabolic organelles, including mitochondria [91-99] and lipid droplets [75, 89, 90]. Regarding mitochondria, the *LRRK2* G2019S mutation has been linked to elevated sensitivity to mitochondrial toxins [92, 93], altered mitochondrial morphology [96, 97], and impaired mitophagy of damaged mitochondria [99]. Furthermore, as mentioned above,

mitochondrial function and dysfunction has long been a focus of the broader PD field [175, 182], with that interest extending beyond *LRRK2*-linked PD to demonstrate mitochondrial defects in sporadic PD as well as PD linked to mutations in other genes (*DJ-1*, *PARKIN*, *PINK1*). Considering the strong precedent for mitochondrial misregulation linked to *LRRK2*, we hypothesized that mitochondria in *LRRK2* G2019S microglia might display signs of malfunction. To test this hypothesis, we set out to assess mitochondrial morphology and fragmentation in microglia. Because fragmentation is linked to mitochondrial dysfunction and increased cellular stress [185], we chose to measure morphology as a high-level readout of mitochondrial health.

### **3.1.1 Mitochondrial fragmentation in *LRRK2* G2019S microglia**

To measure mitochondrial morphology in thousands of microglial cells, we developed a high-throughput, semi-automated imaging and analysis pipeline (Figure 10). In the first step, we fixed microglia and stained against the TOMM20 mitochondrial marker protein. We imaged the microglia at high resolution using a Nikon spinning disk confocal microscope, and we used the Nikon Perfect Focus System to tile and stitch large (*e.g.* ~7-15 mm<sup>2</sup>) fields of mitochondria-labeled microglia (Figure 10a). From these large images—which each contain hundreds of cells—we needed to identify individual microglia. To do so, we used the Ilastik machine learning (ML) software package [186] to train Random Forest pixel and object classifiers on the DAPI (nuclear) signal of these large-field images. Using these ML classifiers, we segmented live nuclei and used custom ImageJ [187] macro (IJM) code to register the centroid of each nucleus to the original large-field image. Registering the nuclear centroids allowed us to extract a sub-image for each cell (Figure 10b). Concurrently, we trained an Ilastik ML pixel classifier to segment the cell area of each microglia based on a highly saturated (*i.e.* background-dominated)

transformation of the immunofluorescence channel (Figure 10c). We then built a blinded, custom IJM graphical user interface (GUI) to manually review each cell mask to screen for potential errors and the unwanted merging of cell masks with those of nearby microglia. After completing this blinded review process, individual cell masks were obtained (Figure 10d), which were then applied to the original images to generate single-cell raw images for each microglia (Figure 10e). A final ML pixel classifier was trained to segment individual mitochondria based on the raw TOMM20 signal, and this classifier was applied to each individual cell (Figure 10f). Properties of each mitochondrion, including area and position, were measured with custom IJM code, and these measurements were subsequently analyzed in Matlab (Mathworks).

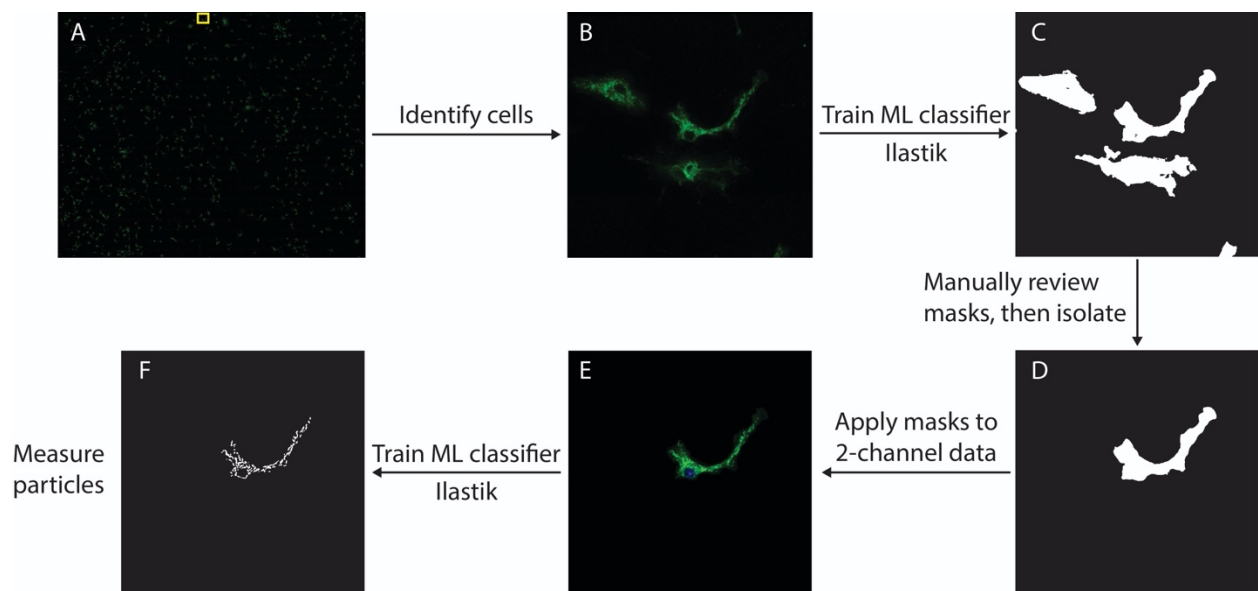


**Figure 10 - Mitochondrial morphology analysis pipeline**

(a) A large-field, tiled image of TOMM20 (mitochondria) labeled microglia was acquired at 40x magnification using a Nikon Eclipse Ti with spinning disk confocal. The data in the yellow box is magnified in (b). (b) Sub-image extracted based on the nuclear centroid of the central cell. (c) Outputs of the Ilastik ML classifier for cell masking, which were manually reviewed and isolated to produce the single-cell mask in (d). (e) Single-cell masks were applied to the raw data, and (f) an ML classifier for mitochondrial segmentation is applied to the cell-masked raw data.

After applying this imaging and analysis pipeline to wild-type and *LRRK2* G2019S

microglia, we observed clear evidence of mitochondrial fragmentation in *LRRK2* mutant



microglia (Figure 11). Across 2 biological repeats, we quantified an average of 483 cells and 21,000 mitochondria per genotype (per repeat). Measurements of mitochondrial area demonstrated a significant decrease in the area per mitochondrion in the LRRK2 G2019S condition (Figure 11b), which is an indication of mitochondrial fragmentation. Concomitant with this decrease in per-mitochondrion area was an increase in the number of mitochondria per cell (Figure 11c), which is consistent with the observation that although the area per mitochondrion decreased in the LRRK2 mutant, the total (combined) mitochondrial area per cell remained the same (Figure 11d). These three observations are self-consistent, because if we assume that total mitochondrial content is maintained across both genotypes (as shown in Figure 11d), then a decrease in per-mitochondrion area should be compensated by an increase in the number of mitochondria (and vice versa). As such, our data are consistent with mitochondrial fragmentation in LRRK2 mutant microglia. In addition to mitochondrial fragmentation, we also observed significantly increased mitochondrion-to-mitochondrion distance in the LRRK2 G2019S condition (Figure 11e), suggesting that the spatial distribution of mitochondria may be altered in the mutant.

Taken together, our results point to potential mitochondrial dysfunction in *LRRK2* mutant microglia, similar to the fragmentation that has been observed in other cell types [96, 97]. Although fragmentation is a good high-level marker for mitochondrial malfunction, future work could add deeper insight by correlating this fragmentation with changes in the metabolic properties of mitochondria, such as their membrane potential. We attempted to measure membrane potential in microglial mitochondria using variants of the commonly-cited mitochondrial membrane potential indicator tetramethylrhodamine methyl ester [188], but

these dyes failed our validation experiments in microglial cultures. Future researchers could test alternative mitochondrial potential dyes—such as JC-1 or MitoView—in microglial primary cultures, and they could also use a specialized instrument (such as the Agilent Seahorse) to measure the oxygen consumption rate of microglia, which would reflect their mitochondrial respiration state.

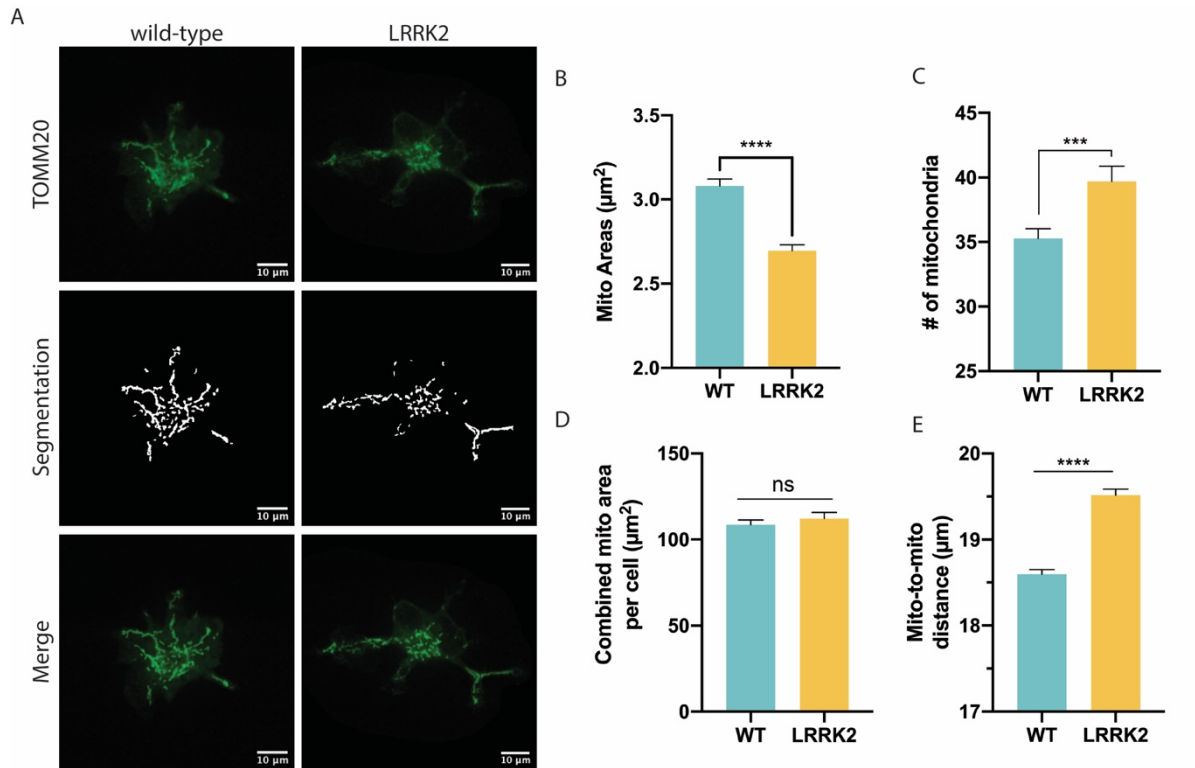


**Figure 11 - Mitochondria are fragmented in LRRK2 G2019S microglia**

Images of mitochondria-labeled microglia were processed using the pipeline outlined in Figure 10, and example wild-type and *LRRK2* G2019S images and segmentations are shown in (a). Because the segmentation channel is binary, the ‘merges’ in the bottom panel are low-opacity overlays of the binary segmentation over the raw data. (b) Area per mitochondria is significantly reduced in the *LRRK2* mutant, whereas (c) the number of mitochondria per cell is increased in the *LRRK2* G2019S mutant. (d) The total area of mitochondria per cell is similar in both genotypes. (e) Average mitochondria-to-mitochondria distances within cells are increased in the *LRRK2* G2019S mutant. Biological repeat data are shown in Appendix 6.1. Statistical tests: two-sided Student’s t-test (b, c, d, e). \*\* $P < 0.01$ , \*\*\*\* $P < 0.0001$ , ns = not significant. Error bars are mean  $\pm$  standard error.

### 3.1.2 Characterization of lipid droplet morphology in wild-type and *LRRK2 G2019S* microglia

As we mentioned above and in the Introduction (Chapter 1.3.4), lipid droplets represent another class of metabolic organelles that have been linked to *LRRK2* regulation [75, 89, 90]. More specifically, *LRRK2* has been reported to regulate LD formation, storage capacity, and accumulation in a variety of cell types and tissues [75, 89, 90]. Furthermore, the aberrant accumulation of LDs in the microglia of aging brains has been observed, and these ‘lipid-droplet-accumulating microglia’ display impaired phagocytosis, high levels of ROS, and increased secretion of proinflammatory cytokines [189]. In addition, the authors observed increased LD accumulation and more drastic phenotypes following the treatment of microglia-like BV2 cells and microglia with the classical activator lipopolysaccharide (LPS) [189]. As such, we set out to characterize the morphology and accumulation of lipid droplets in wild-type and *LRRK2 G2019S* microglia, as well as in conditions where both genotypes were treated with LPS.

Similar to the pipeline that we built for mitochondrial analysis, we also developed a semi-automated microscopy and analysis pipeline for the quantification of lipid droplet features (Figure 12). In two biological repeat experiments, live microglia were labeled with the LD-staining dye boron-dipyrromethane (BODIPY) [190, 191] prior to imaging at super-resolution on an LSM 880 laser-scanning confocal microscope with an Airyscan detector (Carl Zeiss Microscopy GmbH). Following the application of Airyscan deconvolution in the Zen (Carl Zeiss Microscopy GmbH) software suite, individual images—which captured between 1-3 cells per image—were ready for downstream analysis (Figure 12a). Because BODIPY faintly labels the plasma membrane, saturating the BODIPY signal allowed us to train an Ilastik ML pixel classifier to segment the microglial cell masks (Figure 12b), which were then manually reviewed using a

blinded IJM GUI to produce individual cell masks (Figure 12c). These single-cell microglial masks were then applied to the raw Airyscan data (Figure 12d). An ML pixel classifier was trained to segment lipid droplets in our Airyscan data, and this pixel classifier was applied to the cell-masked raw data generated in the previous step (Figure 12e). The resulting per-cell segmented LDs were analyzed using custom IJM code, and these measurements were quantified in Matlab.

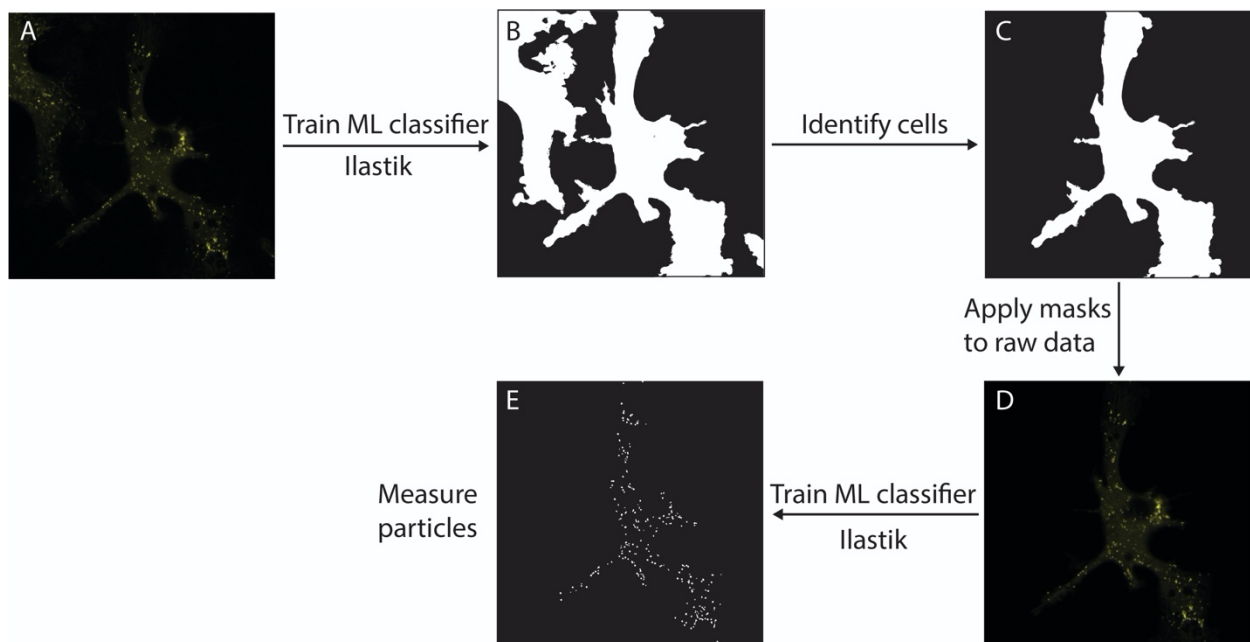


**Figure 12 - Lipid droplet analysis pipeline**

(a) BODIPY-stained live microglia were imaged at 63x magnification on a Zeiss LSM 880 microscope with Airyscan detector, with Airyscan deconvolution applied following image acquisition. (b) Outputs of our ML classifier for BODIPY-based cell masking, which were manually reviewed and isolated to generate a single-cell mask (c). (d) The single-cell microglial masks were applied to the raw Airyscan data, and (e) our ML classifier for LD segmentation was applied to the cell-masked raw data to produce binary images of segmented lipid droplets.

In contrast to the mitochondrial fragmentation observed in *LRRK2* G2019S microglia, we do not see significant genotype-dependent changes in LD morphology or accumulation (Figure 13). More specifically, quantification of LD properties revealed no significant difference between wild-type and *LRRK2* G2019S microglial area per LD (Figure 13b), number of LDs per

cell (Figure 13c), and the total LD area per cell (Figure 13d). This indicates that in contrast to previous studies in HEK293T cells [75, 89] and rat kidney cells, hepatocytes and stellate cells [90] with different LRRK2 variants, microglial lipid droplet morphology and accumulation is not affected by the G2019S mutation. Our negative results are not entirely unexpected, however, because these studies used LRRK2 kinase domain overexpression [75], LRRK2 Y1699C (a LRRK2 GTPase domain mutant) [89], and LRRK2 KO [90] in their evaluation of lipid droplets. Of these three experimental approaches, LRRK2 kinase domain overexpression is likely the most comparable to the LRRK2 G2019S hyperactive kinase mutant, but exogenous overexpression is more prone to induce non-physiologically relevant kinase activity. In sum, we do not observe gross genotype-dependent defects in LD accumulation and morphology in G2019S mutant microglia.

However, upon treatment of microglia with 100 ng/mL LPS for 24h, we observe LPS-dependent (but genotype-independent) changes in lipid droplets. First, we observed a decrease in the size of LDs after LPS treatment of both wild-type and LRRK2 G2019S microglia (Figure 13b), whereas the total number of LDs per cell did not change (Figure 13c). Concomitant with this, we observed a substantial decrease in the fractional LD area per cell (Figure 13d), suggesting that LPS-treated cells have a lower density of lipid droplets than untreated cells. These results do not agree fully with previous observations of LPS-induced LD accumulation in tissue-section microglia and the immortalized pseudo-microglia BV2 cell line [189], but numerous experimental differences could explain this contradiction. First, in their *in vitro* work, the authors treated cells with 5 µg/mL LPS, which is a 50-fold higher concentration than we

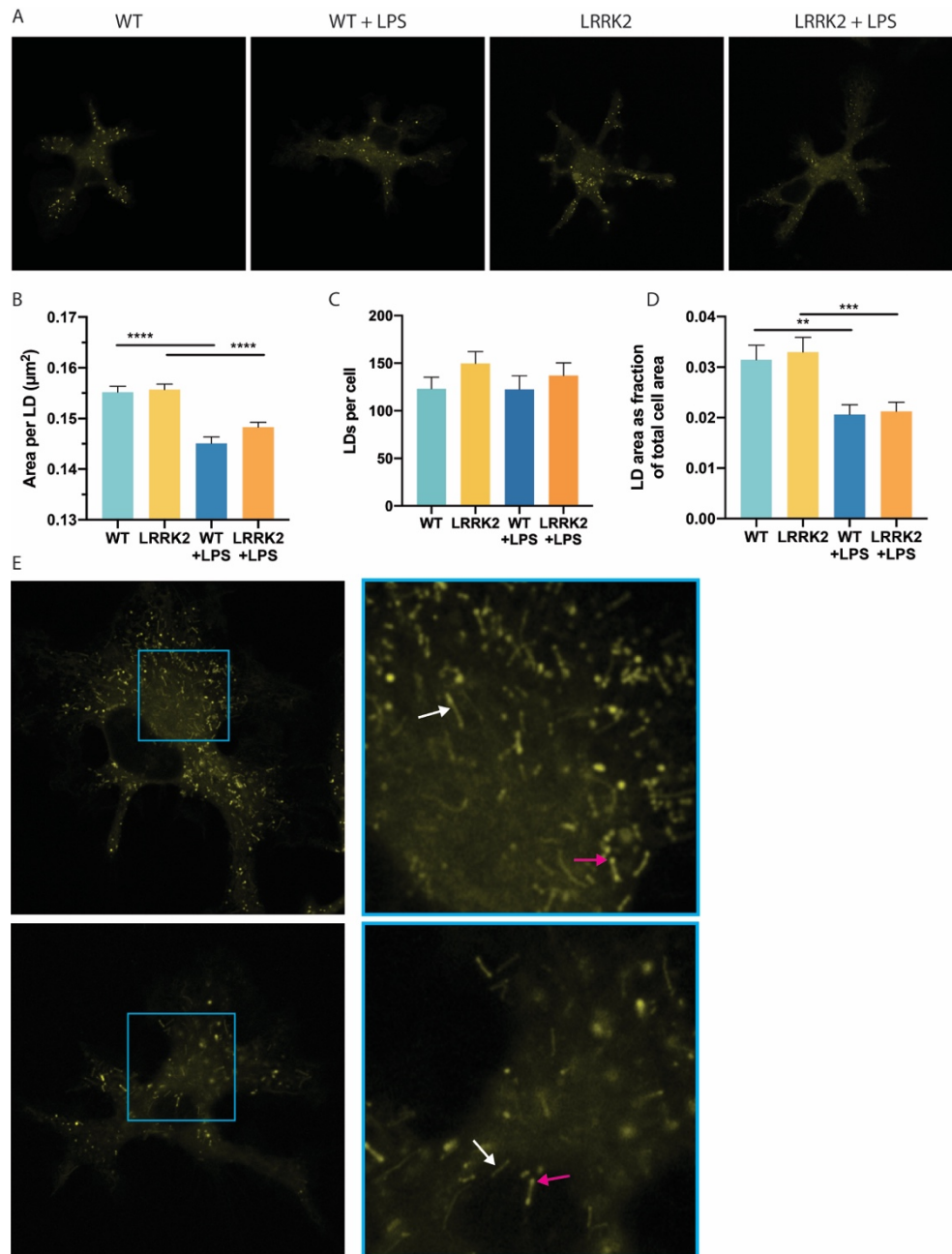


**Figure 13 - LPS treatment induces LD shrinking in wild-type and LRRK2 G2019S microglia**

Microglial lipid droplets were imaged and analyzed as described in Figure 12, and (a) shows example images acquired in each genotype and condition. (b) Quantification of the area per lipid droplet, (c) number of lipid droplets per cell, and (d) lipid droplet area fraction across genotypes and LPS conditions. (e) Example images of ‘lipid rods’ identified in wild-type + LPS (top row) and *LRRK2* G2019S + LPS (bottom row). White and red arrows indicate tubular and ‘dumbbell’ lipid rod morphologies, respectively. Biological repeat data are shown in Appendix 6.1. Statistical tests: one-way ANOVA with Tukey’s post hoc test (b, c, d). \*\* $P < 0.01$ , \*\*\* $P < 0.001$ , \*\*\*\* $P < 0.0001$ , ns = not significant. Error bars are mean  $\pm$  standard error.

used and well above the 1-2  $\mu\text{g}/\text{mL}$  concentration barrier where high toxicity and decreased

microglial viability is observed [192, 193]. Second, LD imaging was performed on fixed (rather than live) cells using an older laser-scanning confocal microscope equipped with a 40x objective, which should have a maximum X-Y resolution of  $\sim 420\text{nm}$  in the most optimal conditions. The average LD areas that they report ( $1.8 - 4 \text{ mm}^2$ ) are far larger than any we could find in the literature, including the characteristically massive single LDs carried by white adipocytes, which at their most extreme have diameters of  $100 \mu\text{m}$  (and an area of  $\sim 7.8 \mu\text{m}^2$ ) [194-196]. We must assume that units were misprinted and that the observed LDs were  $1.8 - 4.4 \mu\text{m}^2$  (with diameters of  $\sim 1500-2500 \text{ nm}$ ), but this still represents the very high end of LD sizes observed in non-adipocyte cells [196]. We suspect that some combination of fixation/staining protocols, high background signal, and (perhaps most importantly) the limited spatial resolution of the imaging modality could have contributed to an inability to detect and/or distinguish the abundant small ( $<450 \text{ nm}$  diameter) LDs that we observed in microglia using super-resolution techniques. Taken together, we believe that these microglial LD imaging results are not directly comparable to ours, but the high-quality results that the authors produced should accurately reflect the behavior and regulation of very large lipid droplets in LPS-stimulated microglia.

In addition to observing decreases in LD size and density in LPS-treated microglia, we also observed a novel LD morphology across our genotypes and treatment conditions (Figure 13e). A subset of LDs in many cells contained elongated, tubular LDs that we have termed “lipid rods,” and we have yet to find a precedent for such lipid rods in any animal or fungal model organisms. The only similar lipid structures that we have identified in the literature are lipid rods present in the chromoplasts of some plant cells [120-123]. Although we observe lipid rods

across the wild-type and *LRRK2* G2019S genotypes and in  $\pm$  LPS conditions, we do see a significant increase in the number of lipid rod-containing cells in LPS-treated cells ( $p=0.0012$ , unpaired Student's *t* test), with 8.6% (95% CI: 3.0%-14.3%) of control cells and 28.8% (95% CI: 19.2%-38.4%) of LPS-treated cells containing lipid rods. However, there is no genotype-dependence of lipid rod abundance. Among lipid rods, we see two morphologies: a dumbbell-type morphology of a lipid rod capped at one or both ends by a spherical droplet and a "purer" rod shape without large, spherical caps (indicated by red and white arrows, respectively, in Figure 13e). Although we have not probed the formation or regulation of these unique lipid rods, we hope that future researchers will carry on imaging lipid droplets at very high resolution in many cell types and under varying stimulatory (or stressful) conditions, as such studies would provide context for the broader relevance (if any) of lipid rods to mammalian physiology.

Taken together, our experiments did not identify major differences between wild-type and *LRRK2* G2019S microglia in terms of LD morphology and accumulation. However, LPS stimulation led to observations regarding LD size and density, as well as the formation of previously undescribed "lipid rods." Although they have minimal bearing on the *LRRK2* field, these results nonetheless highlight the fascinating cell biology of stimulated (and even basal) microglia, as well as the ripe opportunities associated with the application of modern imaging modalities to primary microglia.

### **3.2 Microglial phagocytosis and the endolysosomal system**

As reviewed in the Introduction (Chapter 1.3.3), significant evidence has linked *LRRK2* to the regulation of the endolysosomal system [78-88]. A subset of Rab GTPases (*RAB8A/B*, *RAB12*, *RAB10*, *RAB3A/B/C/D*, *RAB29*, *RAB35*, and *RAB43*) have been identified as physiological



substrates of LRRK2 kinase activity, and these Rabs are involved in endocytic, phagocytic, secretory, and vesicle trafficking pathways in mammalian cells [5, 65]. In neurons, studies have demonstrated LRRK2 regulation of synaptic vesicle endocytosis [78-81]. Further downstream, the LRRK2 G2019S mutant—via misregulation of its substrate RAB8A—delays the trafficking and degradation of endocytosed receptors by impairing late endosomal budding in HeLa cells [82, 83]. LRRK2 and at least 3 of its substrates (RAB12, RAB10, and RAB8) localize to stressed lysosomes and are required for the maintenance of lysosomal homeostasis under stressful conditions in HEK293 cells [84], and LRRK2 G2019S has also been shown to disrupt lysosome positioning in *Drosophila* [85]. Regarding phagocytosis, inhibition of LRRK2 in myeloid cells results in the downregulation of phagocytosis [87, 88], whereas LRRK2 has also been shown to negatively regulate the maturation of *M. tuberculosis* phagosomes in macrophages [86]. Considering the strong precedent for LRRK2 in regulating phagocytosis and the endolysosomal system—as well as the central role that phagocytosis plays in microglial physiology—we set out to assess the effects of *LRRK2* G2019S on microglial phagocytosis, pinocytosis (endocytosis of nonspecific fluid and small particles) and endosome maturation using high-throughput microscopy techniques.

### **3.2.1 Impaired phagocytosis in LRRK2 G2019S microglia**

To evaluate phagocytosis and pinocytosis in wild-type and *LRRK2* G2019S microglia, we performed a microscopy assay to measure the simultaneous uptake of two fluorescence-labeled cargoes. These two cargoes were large, green fluorescent polystyrene microspheres with 1  $\mu\text{m}$  diameter and small, far red fluorescent polystyrene microspheres with 170 nm diameter. Previous work in macrophages has demonstrated that 1  $\mu\text{m}$  beads are internalized

via phagocytosis, whereas 170 nm beads are taken up in a pinocytosis-dominated fashion [197, 198]. Wild-type and *LRRK2* mutant microglia ( $\pm 100$  ng/mL LPS) were incubated with a mixture of 1  $\mu\text{m}$  and 170 nm beads for 2 hours, followed by labeling of the plasma membrane with the red-fluorescent dye Dil (Thermo Fisher), fixation, and DAPI staining of nuclei. Across 2 biological repeats, an average of 250 cells per condition (per repeat) were imaged and quantified using a custom semi-automated imaging and analysis pipeline.

Large-field, tiled images of fixed microglia were acquired using a Nikon Eclipse spinning disk confocal microscope equipped with the Nikon Perfect Focus System (Figure 14a). Individual microglial cells were identified by manual review of the large-field images, and individual windows were extracted for each identified cell (Figure 14b). Using the Dil plasma membrane channel, an Ilastik ML pixel classifier was trained to segment microglial cell areas (Figure 14c). We wrote a custom, blinded IJM GUI to manually review each mask for potential classification errors and undesired merging of adjacent cells' masks, enabling us to obtain single-cell masks for each microglial cell (Figure 14d). Similar to previous analyses, these single-cell masks were then applied back to the raw, 4-channel data (Figure 14e). Using custom ImageJ code and the Trackmate particle-tracking plugin [199], we identified the number and position of 1  $\mu\text{m}$  and 170 nm beads in each cell (Figure 14f).

Quantification of bead uptake revealed genotype-dependent differences in the internalization of 1  $\mu\text{m}$  (but not 170 nm) microspheres. In *LRRK2* G2019S microglia, we observed a significant decrease in the number of 1  $\mu\text{m}$  beads per cell that were phagocytosed, relative to the wild-type (Figure 14g). This impaired phagocytosis was corroborated by flow cytometry analysis of wild-type and *LRRK2* G2019S microglia following incubation with 1  $\mu\text{m}$

fluorescent beads (Figure 14k). In contrast to the decreased phagocytosis observed in the *LRRK2* mutant, we observed elevated phagocytosis of 1  $\mu\text{m}$  beads in both LPS-treated conditions (Figure 14g), which agrees with previous observations of elevated phagocytosis in LPS-treated microglia and macrophages [200, 201]. Although LPS-treated microglia display enhanced phagocytic activity, the measured bead-to-bead distances of internalized microspheres were increased in the LPS conditions (Figure 14h), suggesting lower bead density and an altered spatial distribution of phagocytosed beads within LPS-treated cells. In sum, then we observed an impaired phagocytosis phenotype in *LRRK2* G2019S microglia, and this phagocytic response was the opposite of LPS-treated cells. In the case of phagocytosis, it appears that the *LRRK2* mutation does not mirror the effects observed under 'classical' LPS activation.

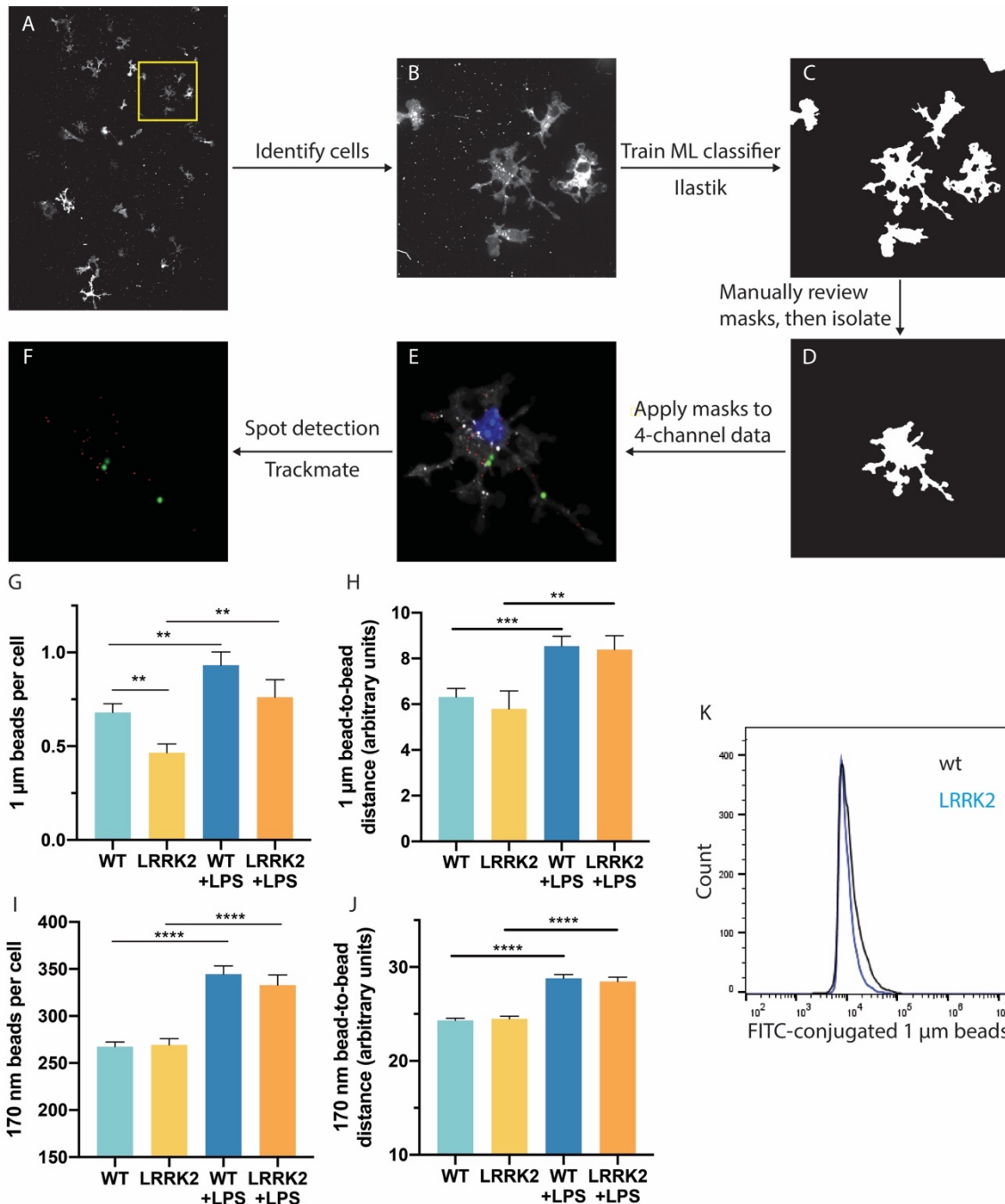


### Figure 14 - Impaired phagocytosis in LRRK2 G2019S microglia

Large-field images of fixed microglia were acquired at 40x magnification on a Nikon Eclipse Ti spinning disk confocal microscope equipped with the Perfect Focus System (a). Individual cells were identified manually, and (b) sub-images were extracted for each cell, corresponding to the yellow box in (a). (c) Outputs of our ML classifier for Dil-based cell masking, which were manually reviewed and isolated to generate a single-cell mask (d). (e) The single-cell microglial masks were applied to the raw image data, and (f) the Trackmate algorithm was implemented to determine the number and position of 1 μm and 170 nm beads in each cell. The (g) number of 1 μm beads per cell, (h) 1 μm bead-to-bead distance, (i) number of 170 nm beads per cell, and (j) 170 nm bead-to-bead distance were computed across all genotypes and LPS conditions. (k) Flow cytometry of 1 μm bead uptake in wild-type and LRRK2 G2019S microglia. Biological repeat data are shown in Appendix 6.1. Statistical tests: one-way ANOVA with Tukey's post hoc test (g, h, i, j). \*\* $P < 0.01$ , \*\*\* $P < 0.001$ , \*\*\*\* $P < 0.0001$ . Error bars are mean  $\pm$  standard error.

When we measured the internalization of pinocytosis-dominated 170 nm beads, we did not observe any LRRK2-dependent effects (Figure 14i). We did, however, record increased internalization (Figure 14i) and increased bead-to-bead distance (Figure 14j) in LPS-treated microglia. This increased uptake of 170 nm beads is consistent with previous characterization of LPS-induced pinocytosis in dendritic cells, macrophages, and the microglia-like BV-2 cell line [202-204]. Whereas LPS induces changes in the uptake of both large (phagocytosis-dominated) and small (pinocytosis-dominated) endocytic cargoes, the *LRRK2* G2019S mutation appears to only affect phagocytic uptake in microglia, and it does so negatively. Considering that phagocytosis is one of the hypothesized activities through which microglia could kill neurons in our co-culture experiments, the LRRK2 mutant's reduction of basal phagocytosis in microglia suggests that nonspecific phagocytic activity is an unlikely mediator of LRRK2-dependent DA neurotoxicity. This is consistent with our earlier observation that conditioned medium contributes significantly to LRRK2-related neurotoxicity. However, it remains possible that a more targeted form of phagocytosis (such as 'phagoptosis') that depends on neuron-microglia signaling could contribute to our observed toxicity. In any case, we observe a significant LRRK2-linked defect in phagocytosis, one of the hallmark functions of microglia. Following our characterization of cargo internalization by microglia, we set out to assess a downstream aspect of the endolysosomal system: endosome maturation.

### **3.2.2 Decreased and delayed endosome maturation in LRRK2 G2019S microglia**

Because of the strong precedents linking LRRK2 to endolysosomal regulation (discussed above and in Chapter 1.3.3) [78-88], we hypothesized that the *LRRK2* G2019S mutation might impair endosome maturation in microglia. To test this hypothesis, we designed a microscopy

assay based on the uptake of fluorescent FITC-dextran and TMR-dextran. Dextran is internalized via endocytosis (pinocytosis) [205, 206], and as dextran-carrying endosomes mature and acidify, the FITC fluorophore dims while the TMR fluorophore is unaffected [207, 208]. As a result, the ratio of FITC: TMR fluorescence in cells incubated with fluorescently-labeled dextrans can be used as a relative measure of endosomal acidification and maturity, where decreasing ratios of FITC: TMR indicate increasing endosomal maturity. To gain insight into changes in endosome maturity over time, we measured FITC: TMR ratios in wild-type and LRRK2 G2019S microglia ( $\pm$  LPS) following 5, 15, and 30 minutes of incubation with FITC- and TMR-labeled dextrans.

More specifically, we added a 1:1 mixture of FITC-dextran and TMR-dextran (both 10,000 MW; Thermo Fisher) to microglial cultures before incubating for the indicated time, washing, and fixing. Large-field, tiled images of TMR, FITC, and DAPI (nuclear) signals were collected using a Nikon Eclipse spinning disk confocal microscope equipped with the Perfect Focus System (Figure 15a). Across 2 biological repeats, we imaged an average of 457 cells per condition (per repeat). As in the mitochondrial morphology experiments, we used an Ilastik ML classifier to segment live nuclei and employed custom IJM code to record the centroid of each nucleus. These nuclear centroids provided the center points for the extraction of equal-sized sub-images for each cell (Figure 15b). An ML classifier was trained on saturated TMR+FITC channels to recognize and segment the dextran-labeled regions of microglial cells (Figure 15c), which generated approximate microglial cell masks. As in previous analyses, a blinded, custom IJM GUI was written to manually review each cell mask for classification errors and undesired merging of adjacent cell masks, resulting in the identification of a single mask per cell (Figure

15d). The individual cell masks were then applied back to the raw data (Figure 15e), and we used custom IJM code to measure the fluorescence intensity in the FITC and TMR channels. These data were further analyzed in Matlab, and a ‘relative endosome maturity’ index was calculated by dividing the pH-insensitive signal (TMR) by the pH-sensitive signal (FITC).

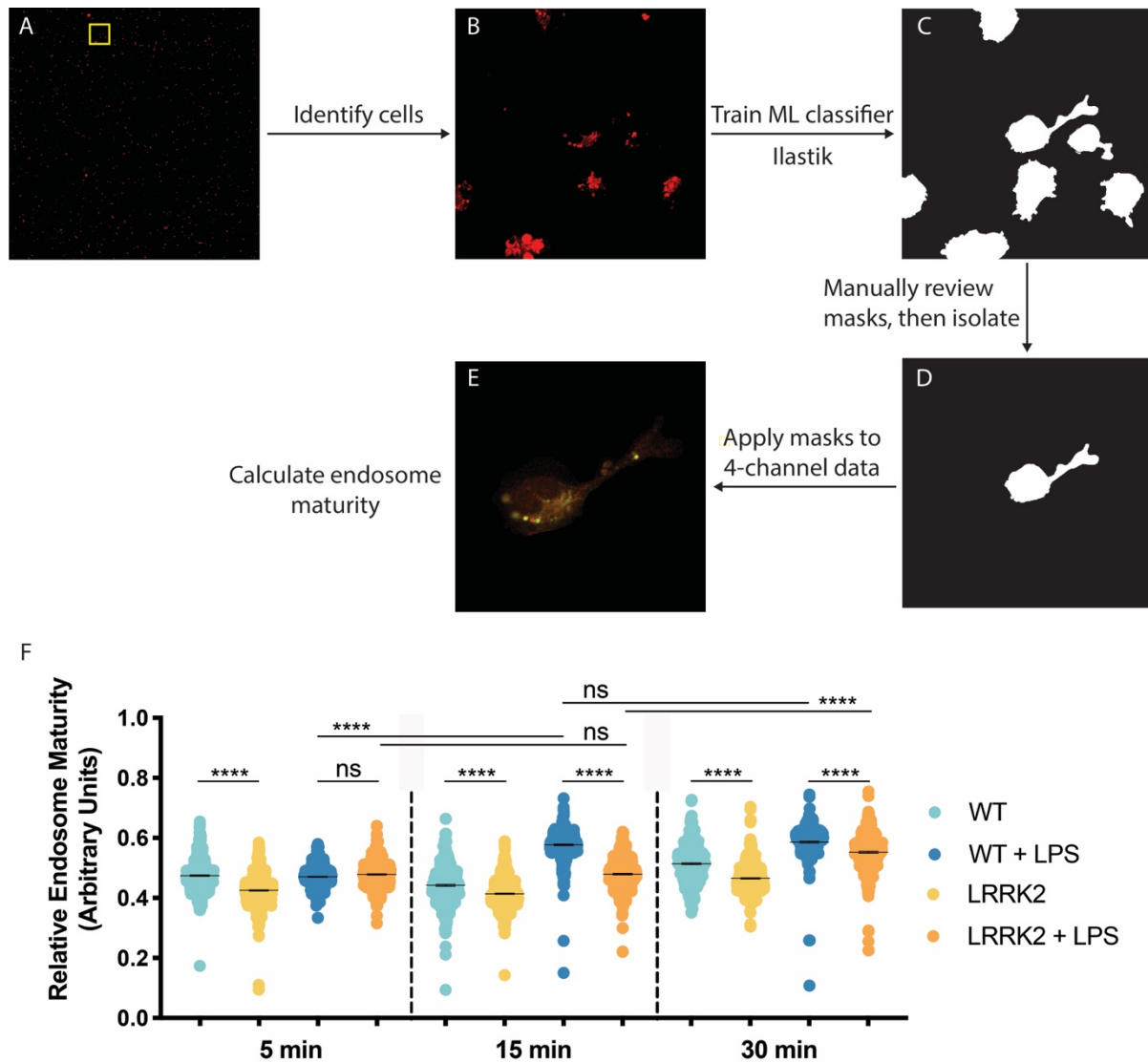


**Figure 15 - LRRK2 G2019S mutation hinders endosome maturation**

Similar to previous experiments, large-field images of fixed microglia were acquired at 40x on a Nikon Eclipse Ti spinning disk confocal microscope equipped with the Perfect Focus System (a). (b) Sub-images were extracted based on the nuclear centroid of each cell, corresponding to the yellow box shown in (a). (c) Outputs of the Ilastik ML classifier for FITC/TMR-based cell masking, which were manually reviewed and isolated to produce the single-cell mask in (d). (e) Single-cell masks were then applied to the raw data. (f) Calculating the TMR (pH-insensitive) to FITC (pH-sensitive) ratio in each cell generates endosome maturity indices, which are plotted across all time points, genotypes, and LPS conditions. Biological repeat data are shown in Appendix 6.1. Statistical tests: one-way ANOVA with Tukey’s post hoc test (f). \*\*\* $P < 0.001$ , \*\*\*\* $P < 0.0001$ . Error bars are mean  $\pm$  standard error.

Analysis of endosome maturity indices across our conditions and time points revealed *LRRK2* G2019S-associated decreases in endosome maturity (Figure 15f). To orient the reader, the Y axis represents relative endosome maturity, with higher values corresponding to more mature endosomes, and the X axis depicts 3 time points following the addition of FITC/TMR dextrans. In the initial 5 min time point, we immediately observe significantly decreased endosome maturity in *LRRK2* G2019S microglia (-LPS, relative to wild-type). This relationship continues through the 30 min time point, when *LRRK2* (-LPS) endosomes remain significantly less mature than their wild-type (-LPS) counterparts, whereas both wild-type (30 min) and *LRRK2* G2019S (30 min) microglia display significantly increased maturity relative to their own 5 min time points (comparisons not shown on plot;  $p < 0.0001$  for both comparisons, one-way ANOVA with post-hoc Tukey HSD). These results suggest that under non-stimulated conditions and across multiple timepoints, *LRRK2* G2019S microglia display impaired endosome maturity relative to the wild-type control.

In contrast to the unstimulated microglia, LPS-treated microglia do not show an endosome maturity discrepancy after 5 min incubation with fluorescently-labeled dextrans (Figure 15f). However, a drastic increase in the endosome maturity of wild-type microglia (+LPS) was observed at 15 min, and a concomitant increase was *not* observed in the LPS-treated *LRRK2* microglia at 15 min. It appears that the wild-type microglia (+LPS) reach an endosome maturity plateau at 15 min, as there is no further increase in wild-type (+LPS) endosome maturity at 30 minutes. However, after an initial lag phase, *LRRK2* mutant microglia (+LPS) show a similar jump in endosome maturity between 15 and 30 minutes, reaching a final maturity level that is still significantly lower than the wild-type (+LPS) 30 min condition. In addition to these genotype-



dependent differences, LPS-treated cells of both genotypes displayed elevated endosome maturity relative to unstimulated microglia at later time points. This observation of increased maturity in LPS-treated microglia agrees with previous results demonstrating LPS-stimulated increases in the delivery of endocytic cargo to acidified late endosomes and lysosomes in monocytes and macrophages [209, 210].

Overall, then, unstimulated *LRRK2* mutant microglia show decreased endosome maturity at every timepoint. In addition to displaying reduced endosome maturity at later time points, LPS-stimulated *LRRK2* G2019S microglia also show temporally-delayed endosome maturation, lagging the jump in maturation observed in LPS-treated wild-type microglia by 15 minutes. While a *LRRK2*-dependent deficit in endosome maturity is clear from these data, the mechanism underlying this deficit is unclear. An attractive possibility emerges from aforementioned studies in HeLa cells that demonstrated *LRRK2* G2019S-dependent delays in the trafficking and degradation of endocytosed receptors [82, 83]. The authors linked these delays in trafficking and endocytic maturation to the increased phosphorylation of the *LRRK2* substrate RAB8A (and subsequent inactivation) by the G2019S hyperactive kinase mutant, and they rescued this phenotype via expression of a phosphodeficient RAB8A mutant. If this process underlies the *LRRK2*-dependent defects in endosome maturation that we observe in microglia, then similar experiments could be performed in an attempt to rescue our phenotypes. Although it is not currently feasible to transfect primary microglia in the ways that the authors transfected HeLa cells, work is ongoing in our lab to develop viral expression constructs that are well-tolerated by microglia. If such tools become available to the primary microglia field, future

researchers could express phosphodeficient RAB8A to assess the contribution of LRRK2 G2019S and RAB8A to the endosome maturation deficits that we have observed.

### **3.3 Migration/chemotaxis and microtubule dynamics**

As we described in the Introduction (Chapter 1.3.5) [100-104], interactions between LRRK2 and the mammalian cytoskeleton have been a major focus of the LRRK2 field. More specifically, direct interactions between LRRK2 and the  $\beta$ -tubulin isoforms TUBB, TUBB4 and TUBB6 have been reported [102]. The site where LRRK2 binds these isoforms is close to the binding site for the microtubule-stabilizing drug taxol, and the authors demonstrate that LRRK2 activity can modulate microtubule (MT) stability [102]. Separate work has linked LRRK2 kinase activity to increased microtubule stability, through direct phosphorylation of both  $\beta$ -tubulin [211] and tau [212]. In the former study, the authors reported that the LRRK2 G2019S mutant shows elevated phosphorylation of  $\beta$ -tubulin, and this phosphorylation activity was linked to increased MT stability *in vitro* [211]. Drawing on these precedents, we hypothesized that the *LRRK2* G2019S mutation might disrupt microtubule dynamics in microglia. Furthermore, due to the role that microtubules play in scaffolding and regulating cell migration [213, 214], we suspected that *LRRK2* G2019S microglia might display deficiencies in chemotaxis and migration, one of the core cell-type-specific functions that microglia perform in the CNS.

#### **3.3.1 Reduced tubulin recovery in LRRK2 G2019S microglial lamellipodia**

To assess microtubule dynamics in microglia, we performed live super-resolution microscopy of microtubules. Microglia were incubated for 12 hours in 100 nM SiR-Tubulin (Cytoskeleton, Inc.), a fluorogenic dye that labels microtubules. Live microglia were imaged at 30s intervals on an LSM 880 microscope with Airyscan detector (Zeiss GmbH), and automated

Airyscan deconvolution was applied in the Zen software package (Zeiss GmbH). An example frame from the time series acquisition of a live tubulin-labeled microglial cell is shown in Figure 16a.

Analysis of tubulin dynamics in microglial lamellipodia revealed a clear qualitative decrease in the *LRRK2* G2019S recovery velocity of extended microtubules returning toward the cell body (Figure 16b). In these images, successive frames are colored according to the legend, so individual MTs in motion appear as a series of distinctly-colored tubules. Increased distance between frames corresponds to higher microtubule recovery velocity, so the indicated MT in the wild-type cell is moving more rapidly than the MT indicated in the *LRRK2* mutant cell. To quantify these dynamics, we analyzed MT velocity in lamellipodia using the ImageJ Manual Tracking plugin. Across 2 biological repeats, analysis of MT tracks in 17-19 cells per genotype revealed a robust and significant decrease in the tubulin recovery velocity of *LRRK2* G2019S microglia (Figure 16c).

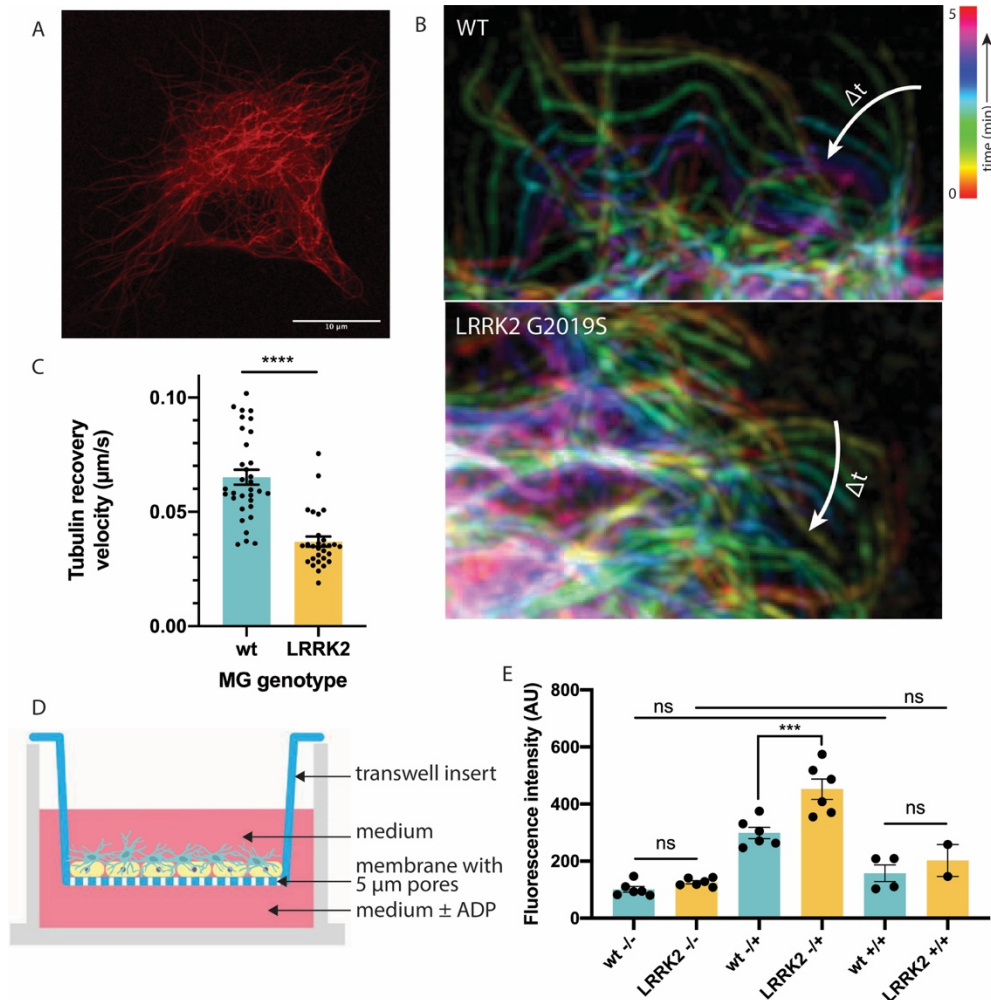


**Figure 16 - LRRK2 G2019S microglia display reduced tubulin recovery velocity and enhanced chemotaxis**

Microglia were labeled with the fluorogenic microtubule dye SiR-tubulin, and time series were collected at 63x with 30s intervals on a Zeiss LSM 880 with Airyscan detector, and Airyscan deconvolution was applied to the time series following acquisition. (a) An example frame from a time lapse experiment. (b) Temporal color-coded projection of representative microtubule time series in wild-type and LRRK2 G2019S microglia. According to the legend at right, the colors in each image correspond to different points in the time series. (c) Quantification of tubulin recovery velocity in lamellipodia of wild-type and LRRK2 mutant microglia. Each data point represents the velocity of one MT track, and the data are pooled across 2 biological repeats (19 cells for wild-type, 17 cells for LRRK2). (d) Design of transwell experiments for microglial chemotaxis, where microglia are plated in the upper chamber, and the media in the upper and lower chambers can be changed to induce chemotaxis. (e) Chemotaxis results, where (-/-) indicates microglia medium + vehicle in both chambers, (-/+) indicates microglia medium + vehicle in the upper chamber and microglia medium + ADP in the bottom chamber, and (+/+) indicates microglia medium + ADP in both chambers. Fluorescence intensity corresponds to the number of migrated cells. Statistical tests: two-sided Student's t-test (c), one-way ANOVA with Tukey's post hoc test (e). \*\*\* $P < 0.001$ , \*\*\*\* $P < 0.0001$ . Error bars are mean  $\pm$  standard error.

### 3.3.2 Increased migration and chemotaxis in LRRK2 G2019S microglia

To address the question of microglial chemotaxis in the context of our *LRRK2* mutation, we carried out trans-well migration assays similar to those in previous studies of microglia [124,

215]. Briefly, following the isolation of primary microglia, cells were plated on a transwell insert that holds a membrane with 5  $\mu\text{m}$  pores (Figure 16d). The media composition above and below the insert can be independently controlled, and chemotaxis activity is induced by adding ADP (a chemoattractant) to the lower well while keeping basal medium in the upper well. Microglia can travel through the pores toward the chemoattractant, and the number of migrated cells can be measured using the CyQuant Direct kit (Thermo Fisher). When we measured ADP-induced chemotaxis in primary microglia, we saw that ADP increased chemotaxis in both genotypes, but the *LRRK2* G2019S microglia showed enhanced chemotactic activity (Figure 16d). In this figure, the left 2 columns represent basal medium in the top and bottom chambers (-/-), the middle two columns only have ADP in the lower chamber (-/+), and the right two columns have ADP in both chambers (+/+). If elevated migration was observed in the double-ADP (+/+) condition (relative to the (-/-) condition), then one could conclude that ADP may simply enhance the nonspecific motility of the microglia. However, this is not the case (Figure 16d), so we conclude that ADP induces chemotaxis of our primary microglia and that *LRRK2* G2019S microglia have an enhanced migratory response to this chemotactic cue.

### **3.4 Chapter Summary**

In contrast to the neuron-microglia focus of the previous Results chapter, our work here focused solely on the cell biology and intrinsic functions of microglia. In our evaluation of previous work in the field, we identified strong links between *LRRK2* and the regulation of 3 major systems: metabolic organelles, the endolysosomal system, and the cytoskeleton. Because we sought to better understand the intrinsic differences between the wild-type and *LRRK2*

G2019S microglia that we used to study neurotoxicity in a co-culture model, we decided to characterize aspects these 3 broad areas of cell biology as they related to the *LRRK2* mutation.

When we analyzed the morphology and distribution of metabolic organelles, we identified *LRRK2*-dependent and *LRRK2*-independent effects. Characterization of mitochondrial morphology revealed that *LRRK2* G2019S mitochondria are fragmented relative to the wild-type control, with smaller, more abundant, and less densely packed mitochondria (Figure 11). Because fragmentation is associated with mitochondrial dysfunction and increased cellular stress [185], mitochondrial regulation by *LRRK2* (and the hyperactive G2019S mutant) could represent a potential cell-intrinsic contributor to the microglia-induced neurotoxicity that we observe in co-culture. Future work focused on rescuing this mitochondrial fragmentation (for example, through inhibition of mitochondrial fission) could shed light on the relevance of mitochondria to the neurotoxicity we observe. When we analyzed the size, number and distribution of lipid droplets, we found no differences between wild-type and *LRRK2* G2019S microglia (Figure 13). This suggests that *LRRK2* may not play a major role in the regulation of LDs size or accumulation in primary microglia. However, we did note that LPS stimulation reduced LD size and the cellular area fraction composed of LDs, a finding that we have not seen reported in the microglia literature. Furthermore, we identified intriguing 'lipid rods' that have not been reported in animal or fungal literature, and these novel structures likely warrant in-depth cell biological investigation independent of any *LRRK2* regulation.

In our characterization of elements of the endolysosomal system, we identified *LRRK2*-dependent deficiencies in phagocytic uptake and endosome maturation. In our first set of experiments, we evaluated the internalization of phagocytosis-dominated 1  $\mu$ m beads and

pinocytosis-dominant 170 nm beads (Figure 14g,i). We observed that *LRRK2* G2019S microglia show reduced phagocytic activity (relative to wild-type), whereas there were no genotype-dependent changes in pinocytic uptake. Based on this demonstration of reduced phagocytic activity in *LRRK2* mutant microglia, we further speculated that elevated nonspecific phagocytosis is not a likely contributor to neurotoxicity in our co-cultures, as wild-type microglia appear to phagocytose more readily than *LRRK2* mutant microglia in our assays. Furthermore, as expected, stimulation with LPS elevated both pinocytosis and phagocytosis in microglia of both genotypes. Further downstream of these 2 internalization pathways, we observed *LRRK2*-dependent decreases in the magnitude of endosome maturation, as well as temporal delays in endosome maturation in LPS-treated *LRRK2* mutant cells (Figure 15f). As discussed in Chapter 3.2.2, *LRRK2* G2019S phosphorylation of RAB8A results in delays in endocytic trafficking, maturation and degradation [82, 83]. Misregulation of this pathway in G2019S mutant microglia is an attractive explanation for the endosome maturation behavior that we observe, and future work could assess the relevance of RAB8A to the phenotype that we observe. In sum, then, *LRRK2* G2019S microglia display reduced phagocytic activity as well as decreased and delayed endosome maturation in comparison to wild-type controls.

Our final area of interest was the microtubule cytoskeleton and microglial migration/chemotaxis, and we observed genotype-dependent changes in both of these experiments. As reviewed above, MT recovery velocity in microglial lamellipodia was decreased in *LRRK2* G2019S cells (Figure 16c), whereas chemotaxis was elevated in the *LRRK2* mutant. Considering the precedent for increased tubulin phosphorylation and elevated MT stability in the presence of the *LRRK2* G2019S hyperactive kinase [211], our observation of reduced MT

recovery velocity makes intuitive sense. However, future work to characterize LRRK2 phosphorylation of MTs, MT-associated proteins, and tau in our system—and to visualize any such alterations in the lamellipodia of live or fixed cells—would begin to directly link our work to this potential mechanism. At first glance, our observation of elevated chemotaxis and migration toward ADP in *LRRK2* mutant microglia might seem at odds with observations of decreased MT velocity in lamellipodia. However, it is crucial to note that although MTs are required for migration and are involved in its regulation, microglial chemotaxis has many additional layers of signaling-based regulation, including the phosphoinositol-3-kinase (PI3K), calcium-independent phospholipase A<sub>2</sub> (iPLA<sub>2</sub>), ionotropic (P2X), metabotropic (P2Y) and protein kinase A (PKA) pathways, among others [216]. Thus, we should not expect changes in migration and chemotaxis to be dependent entirely on MT regulation, and it is possible that the elevated chemotaxis we observe in *LRRK2* G2019S microglia is linked to one or more of these MT-independent pathways.



## 4 DISCUSSION

The work described here has presented evidence of changes in the DA neurotoxicity and cell-intrinsic functions of microglia carrying the Parkinson's disease mutation *LRRK2* G2019S. Because mutations in the *LRRK2* locus represent one of the strongest genetic risk factors for PD—and because the G2019S mutation alone is linked to 6% of familial PD cases and 2% of sporadic cases [217, 218]—*LRRK2* has long been a focus of the Parkinson's and neurodegenerative disease fields [219]. Considering that dopaminergic neuron death in the substantia nigra is one of the defining characteristics of PD [1], CNS-focused *LRRK2* research has largely characterized the cell-autonomous effects of *LRRK2* mutations in neurons. Such work has been fruitful, with numerous studies in human stem cell models demonstrating susceptibility to oxidative stress [93], morphological alterations [220], impaired NF- $\kappa$ B signaling [221], and elevated cell death [222, 223] (among other phenotypes) in neurons and neural stem cells. These phenotypes, combined with the observation of glial activation in PD-affected brains [9, 224], naturally led to a neuron-centric view of *LRRK2*-related neurodegeneration (Figure 17) wherein supportive astrocytes and microglia are thought to simply respond and cater to the needs of diseased and malfunctioning neurons.

### 4.1 *LRRK2* G2019S microglia-induced DA neurotoxicity

However, as reviewed in the Introduction (Chapters 1.1 and 1.2.4), abundant recent work has shown that independent of neuronal function (or malfunction), astrocytes and microglia are capable of inducing neurotoxicity and neurodegeneration [9, 15, 119]. Independent of these observations, *LRRK2* has been linked to immune-related pathways (including I $\kappa$ B family kinases [112], NF- $\kappa$ B [111], and NFAT [110]); inflammatory diseases like Crohn's, leprosy, and



**Figure 17 - A neuron-centric model for LRRK2-associated neurodegeneration**

Based on precedents for deleterious cell-autonomous effects in LRRK2 G2019S neurons, a neuron-centric model of LRRK2-related neurodegeneration is logical. In such a model, neurons ('N'), astrocytes ('A'), and microglia ('M') all carry the relevant PD mutation, but neurodegeneration and PD progression is catalyzed in a cell-autonomous manner by disease-carrying neurons (green, middle panel). Glial activation and/or malfunction (green astrocyte and microglia, right panel) are a reaction to—and consequence of—neuronal malfunction.

tuberculosis [61, 116]; and cell biological processes—such as phagocytosis [86-88]—that are central to microglial function in the CNS. Considering both the precedent for microglia-induced neurotoxicity and the cellular effects of LRRK2 mutations, we set out to test the hypothesis that

**G2019S mutation-carrying microglia promote dopaminergic neurotoxicity.**

In Chapter 2 (Results Part 1), we tested this hypothesis using a co-culture system. When we cultured wild-type midbrain neurons with wild-type and *LRRK2* G2019S microglia, we observed a robust decrease in dopaminergic neuron survival only in the presence of *LRRK2* mutant microglia, but not wild-type microglia (Figure 6c). These results suggest that microglia can contribute to non-cell-autonomous dopaminergic neurodegeneration. Our findings in microglia mirror those reported with iPSC-derived *LRRK2* G2019S astrocytes, where the authors also observed non-cell-autonomous neurodegeneration induced by astrocytes [119]. In contrast, the *LRRK2* G2019S genotype in neurons was not associated with reduced DA neuron survival in our co-culture system (Figure 6e), suggesting that LRRK2-associated cell-autonomous neurodegeneration is not a major factor in our *in vitro* system. Still, other groups have reported significant deficiencies and sensitivities in human stem cell models of *LRRK2* G2019S neurons,

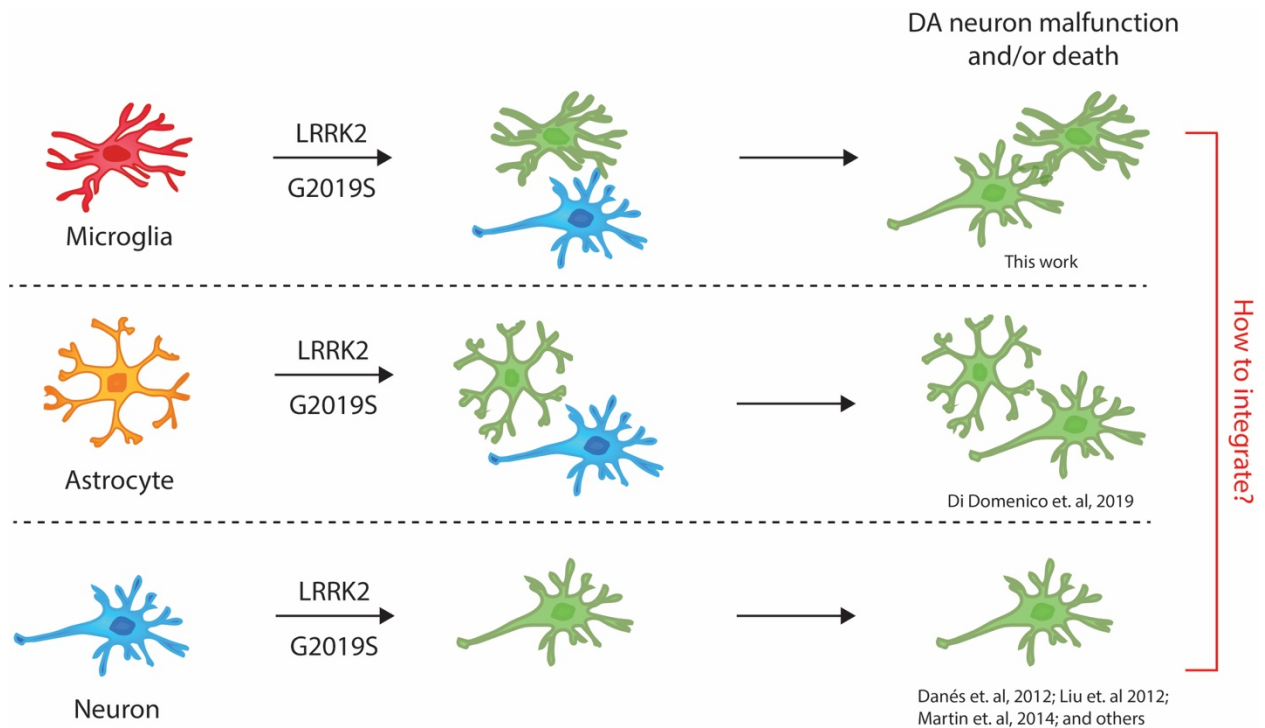


**Figure 18 - Speculative model for LRRK2-linked neurodegeneration**

An updated model for LRRK2-linked neurodegeneration recognizes the capability of LRRK2 mutations in at least 3 cell types (microglia, astrocytes, and neurons) to induce neurodegenerative phenotypes. (Top panel) In the work reported here, *LRRK2* G2019S microglia induced neurotoxicity in wild-type dopaminergic neurons. (Middle panel) Previous human iPSC work in other groups (and yet-to-be-published work from our group) has demonstrated similar killing of wild-type midbrain DA neurons by *LRRK2* G2019S astrocytes. (Bottom panel) Multiple studies have reported cell-autonomous neuronal malfunction and death in human stem cell models.

and these observations are reflected in our updated model of LRRK2-linked neurodegeneration (Figure 18). This model acknowledges that DA neurodegeneration can be caused non-cell-autonomously by both microglia and astrocytes, and cell-autonomous neuronal malfunction also appears to play a role. However, the weakness of this ‘model’ is obvious: it does not integrate or quantify the relative contributions of each cell type to LRRK2-linked neurodegeneration. We attempted to touch on this question by evaluating *LRRK2* G2019S neurons in our co-culture system, but future work in this area could more comprehensively tease apart these contributions. As depicted in Figure 19, a co-culture system in which the genotypes of neurons, microglia, and astrocytes are all independently controlled offers a more

exhaustive approach to evaluating the quantitative contribution of each cell type to neurodegeneration. In theory, such experiments could be carried out in both human iPSC and rodent primary culture models. Although they would be logistically demanding in either system, the results would help illuminate the ambiguities of the disjointed model presented in Figure 18.

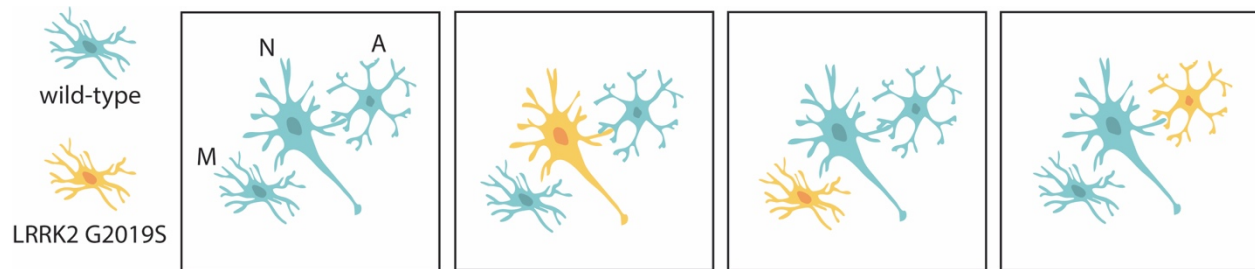


**Figure 19 - A three-component, genotype-controlled culture system**

In a three-component co-culture system, the *LRRK2* genotypes of neurons (N), microglia (M), and astrocytes (A) could be independently controlled. By comparing the triple-wild-type condition (far left) to conditions in which either neurons, microglia or astrocytes alone carry the *LRRK2* G2019S mutation, the relative contribution of each cell type to DA neurodegeneration could be assessed. A more exhaustive set of experiments (not shown) could increase the number of genotype combinations by testing the effects of 2 cell types carrying the mutation (e.g. *LRRK2* G2019S microglia and astrocytes with wild-type neurons) in addition to evaluating a triple-mutant condition.

## 4.2 Characterization of cell-autonomous changes in *LRRK2* G2019S microglia

Narrowing our focus back on microglia, we sought to better understand the general mechanism by which *LRRK2* G2019S microglia can negatively impact DA neuron survival. Experiments with microglia conditioned medium demonstrated that *LRRK2* G2019S microglia-induced neurotoxicity can occur in the absence of direct physical contact with neurons (Figure 9). These results suggested that media components—such as cytokines, exosomes, and microvesicles—released (or not released) by *LRRK2* G2019S microglia could contribute to neurodegeneration. Follow-up experiments focusing on the cytokine profiles of wild-type and *LRRK2* mutant MCM were inconclusive (Figure 9), and we suggested future experiments—

including conditioned medium mass spectrometry and toxicity experiments with exosomes and microvesicles—as avenues to better understand the basis of MCM-induced toxicity.

Additionally, the magnitude of *LRRK2*-induced DA neurotoxicity was lower in MCM experiments than in co-culture, suggesting that contact-mediated toxicity (such as ‘phagoptosis’) may also contribute to the neurodegeneration that we observe. After confirming *LRRK2* G2019S microglia-induced neurotoxicity and failing to identify the factor(s) responsible, we next characterized the effects of our *LRRK2* mutation on a number of cell biological processes and microglial functions.

Based on precedents in the literature linking *LRRK2* activity to the regulation of metabolic organelles, the endolysosomal system and the microtubule cytoskeleton, we designed a series of microscopy experiments to evaluate the effects of the *LRRK2* G2019S mutation on elements of these systems in microglia. The results of these experiments are summarized in Table 1. Briefly, microscopy experiments demonstrated that mitochondria in *LRRK2* mutant microglia are more fragmented and more numerous than in wild-type microglia (Figure 11). In contrast, no genotype-dependent differences were observed when we assessed lipid droplet morphology and accumulation (Figure 13). However, in results that are not relevant to *LRRK2* but that may be of interest to the broader microglia field, we observed LPS-induced changes in LD size as well as a novel ‘lipid rod’ morphology that is more prevalent in LPS-treated microglia.

When we evaluated the uptake of large (phagocytosis-dominated) and small (pinocytosis-dominated) fluorescent microspheres by wild-type and *LRRK2* G2019S microglia ( $\pm$  LPS), we observed impaired phagocytosis and unchanged pinocytosis in the *LRRK2* mutant (Figure 14). We also reported elevated phagocytosis and pinocytosis in all LPS-stimulated conditions,

consistent with previous reports in microglia, macrophages, dendritic cells, and the microglia-like BV-2 cell line [200-204]. Microscopy assays of endosome maturation demonstrated impaired (in unstimulated microglia) as well as impaired and delayed (in LPS-stimulated microglia) endosome maturation in *LRRK2* G2019S microglia (Figure 15). We proposed that elevated phosphorylation of the *LRRK2* kinase substrate RAB8A might be responsible for these deficits [82, 83], and we suggested experiments with phosphodeficient RAB8A as a possible future experiment to evaluate this hypothesis.

We next assessed one aspect of microtubule dynamics by measuring the retraction velocity of microtubules in microglial lamellipodia. We observed a significant and robust decrease in MT retraction velocity in *LRRK2* G2019S lamellipodia (Figure 16), a result that fits in well with previous observations of *LRRK2* regulation of MT stability by binding to and phosphorylating  $\beta$ -tubulin and MT-associated proteins [102, 211, 212]. In our final characterization of microglia-intrinsic function, we employed a transwell assay to measure the chemotaxis activity of microglia. We found that both wild-type and *LRRK2* mutant microglia chemotax toward ADP, but this chemotaxis activity is elevated in *LRRK2* G2019S microglia (Figure 16). Observations of reduced MT velocity and elevated chemotaxis in G2019S microglia might seem contradictory, but the many layers of signaling-based regulation of chemotaxis [216] suggest that *LRRK2* regulation may intersect with chemotaxis in a MT-independent manner. In sum, we have cataloged a number of changes in microglia-intrinsic cell biological processes and functions in *LRRK2* G2019S mutants, although the mechanisms underlying these effects are unclear, and we have not attempted to link or unify the results across these disparate experiments.

**Table 1 - Summary of *LRRK2* G2019S microglia-intrinsic results**

| Microglial cell biological feature or process | Observed behavior in <i>LRRK2</i> G2019S mutant |
|---|---|
| Mitochondrial morphology                      | Fragmented                                      |
| Lipid droplet morphology and accumulation     | Unchanged                                       |
| Phagocytosis                                  | Impaired  |
| Pinocytosis                                   | Unchanged                                       |
| Endosome maturation                           | Impaired  |
| MT recovery in lamellipodia                   | Reduced velocity                                |
| Chemotaxis                                    | Elevated  |

### 4.3 Integration of results and future directions

In sum, our results fall into two main categories—microglia-induced DA neurotoxicity and altered cell-autonomous microglial activity—that would ideally be linked together in an overarching model of the role of *LRRK2* G2019S microglia in neurodegeneration. Again, such a model would address 2 main concerns: 1) the mechanism(s) by which *LRRK2* G2019S microglia kill (or fail to support) DA neurons and 2) how changes in microglial-intrinsic processes underlie those mechanisms. To better understand *how* neurons die in the presence of *LRRK2* mutant microglia, future researchers could carry out experiments that we described in Chapter 2.4. These include ‘secretomics’ mass spectrometry of wild-type and *LRRK2* G2019S microglia conditioned medium to identify proteins that are enriched or depleted in *LRRK2*-conditioned medium. Furthermore, differential ultracentrifugation could be used to purify and characterized the contents of exosomes and microvesicles from microglial culture medium, and

the toxicity of these preparations toward DA neurons could be assessed. Across all of these experiments, the goal would be to identify a factor (or set of factors) that contribute to DA neurotoxicity, and then rescue the phenotype by neutralizing the factors (if they are proteins that are enriched in *LRRK2* MCM, exosomes, or microsomes) or adding back recombinant versions of factors (if they are depleted in *LRRK2* G2019S extracts). Along with rescue, recapitulation of DA neurotoxicity by adding or neutralizing components of wild-type microglial extracts would provide more certainty regarding the basis of neurotoxicity. Further downstream, a full mechanistic understanding of neurotoxicity would require research into the ways that neurons respond to and die upon exposure to such factor(s).

The other half of an overarching model would seek to explain how changes in *LRRK2* G2019S microglial regulation and behavior underlie the observed neurotoxicity. Put more simply: what is happening within microglia that leads them to secrete toxic factors (*e.g.* cytokines, exosomes, microvesicles, or another mediator) or withhold supportive factors? Once the mediator of toxicity is determined, the modulation of relevant pathways in microglia could provide a means of rescuing or recapitulating the phenotype that we observe. For example, drawing on the processes characterized in this work, does inhibiting mitochondrial fission in *LRRK2* mutant microglia with Mdivi-1 [225] rescue neurotoxicity, and does inducing fission via Drp1 overexpression [226] recapitulate the phenotype? As another example, does the introduction of phosphodeficient RAB8A [66] to *LRRK2* G2019S microglia rescue their endosome maturation defect and, as a result, rescue the neurotoxicity phenotype? It is clear that defining the mechanisms linking *LRRK2* to the microglia-intrinsic effects that we observe would be very valuable to future efforts to clarify this half of the overarching model.



#### 4.4 Therapeutic implications for PD

Perhaps even superseding the relevance and importance of the idealized model is a more therapeutically-oriented question: how does such work relate to Parkinson's disease, and could insights from a complete model help treat PD patients? When we consider the disease course of PD, it is important to highlight that age is the strongest risk factor for PD, and *LRRK2*-associated PD is the most common late-onset form of the disease [1]. PD develops slowly over the course of many years, and once a patient has begun to show signs of Parkinsonism (*e.g.* tremor and bradykinesia), 60% of DA neurons in the SN have already been lost, leading to an 80% reduction in striatal dopamine levels [59]. After recognition of the disease, treatment is essentially the same as it was in the 1960s: relief of symptoms by supplementing CNS dopamine levels with oral administration of levodopa [227]. The most promising treatments in the pipeline for diagnosed patients are stem cell therapies to replace the dopaminergic neurons that are lost in PD. Following successful proof-of-principle studies in macaques [228], these stem cell therapies have moved on to human trials in multiple countries [229].

However, the potentially fatal weakness of such treatments is that significant damage has already been done by the time a patient has been diagnosed with PD. As such, understanding the earlier, pre-Parkinsonism stages of PD at a cellular level may provide opportunities to diagnose the disease earlier and *prevent* the massive loss of DA neurons, as opposed to replacing them once they're gone. To that end, understanding *LRRK2*-dependent changes in the regulation and behavior of microglia, astrocytes, and neurons could provide new avenues for both diagnosis and treatment. If future researchers determine that neurotoxic *LRRK2* mutant microglia and/or astrocytes release factors that contribute to neurodegeneration, those factors

could be evaluated as potential biomarkers for early detection of disease. Furthermore, if misregulation of specific pathways or processes in glia—such as exosome release, mitochondrial homeostasis, or endolysosomal regulation—could be directly linked to neurodegenerative phenotypes, then small molecule-based modulation of these pathways could provide a means to *prevent* DA neuron loss. As such, more fully understanding LRRK2 PD from a glial perspective could provide opportunities to improve the way that PD is diagnosed and treated. Although we have not yet developed a unified neuron-astrocyte-microglia model of LRRK2-dependent neurotoxicity (Figure 18) or a detailed mechanism for microglia-induced neurotoxicity, the tools and resources required to understand these processes are improving at a rapid rate.

## **5 METHODS**

### **5.1 Serum- and BSA-free isolation and culture of primary mouse microglia**

This protocol is a modified and extended version of a previously-published rat microglia isolation protocol [118]. Primary microglia cultures were prepared from neonatal mice using methods approved by the Janelia Research Campus Institutional Animal Care and Use Committee (IACUC; protocols #15-129 and #17-152). This method is appropriate for a single researcher to isolate primary microglia from 8-10 mice aged p12-p15. To purify microglia from greater numbers of neonatal mice, it is recommended that multiple researchers work in tandem to minimize the time between dissection and eventual plating. Long periods of waiting lead to increased cell death and decreased isolation efficiency.

#### **5.1.1 Transcardial perfusion and dissection**

Mice were anesthetized with isoflurane until gasping ceased and a foot pinch elicited no response (generally 1-2 minutes, but this varies with age). During anesthetization, 5-10 mL of ice-cold perfusion buffer (50 µg/mL heparin [Sigma #H3149-100KU] in DPBS with Ca<sup>2+</sup> and Mg<sup>2+</sup> [DPBS++], sterile filtered) was loaded into a 10 mL syringe equipped with a 25g needle. Anesthetized mice were then placed on a wax-coated dissection tray, and 3x25g needles were used to pin the limbs to the tray. Pin placement is a choice of personal comfort, but pins were placed in 3 approximate locations: the left axilla, the right axilla, and underneath the right groin.

Graefe forceps (F.S.T #11051-10) were used to pinch the skin along the midsagittal plane, inferior to the ribcage. Cut only the pinched skin (and no underlying tissue) using small scissors (F.S.T. #14058-09), and continue to cut in the superior direction, stopping near the superior end of the ribcage. Use the scissors to extend the incision laterally and remove the flaps

of skin that are produced. The skin should now be completely removed above the ribcage. Using Graefe forceps to hold the xiphoid process, cut through the abdominal wall laterally. Next, make a small incision in the diaphragm to equilibrate with ambient air, and then cut the diaphragm laterally. Do not cut any organs, particularly the liver. Oftentimes, the position of the liver prevents a clean diaphragm cut; to avoid this, simply close the scissors and use them to push the liver away from the diaphragm. Next, cut the ribs parallel to sternum on both sides, and lift up the ‘flap’ of ribcage that is produced. Cut this ‘flap’ off completely, again taking care to not cut any organs or major blood vessels.

The heart should now be visible. Insert the syringe needle into inferior side of the left ventricle, and use micro dissecting spring scissors (ROBOZ #RS-5603) to cut the right atrium. Slowly inject perfusion buffer into the left ventricle. As perfusion progresses, the run-off will transition from dark red to clear, and the liver will become white. With perfusion complete, use large scissors to decapitate. Spray the head with 70% ethanol before transferring to an ethanol-soaked paper towel in a laminar flow hood.

Use a new pair of scissors to cut the skin sagittally on the dorsal side of the head, and move the skin to reveal the skull. Next, cut the skull sagittally, and use blunt tweezers (Digi-Key #243-1270-ND) to remove either half of the skull, revealing the cortex. Insert a pre-wetted spatula (F.S.T. #10090-13) underneath the brain, remove the brain, and transfer to a 50 mL tube containing ~8mL douncing buffer (200uL 0.4% DNase [12,500 units DNase (Worthington #LS002007) in 1mL EBSS, sterile filtered] per 50mL DPBS++, ice cold) in a bucket of ice.

### **5.1.2 Douncing**

Repeat the above steps for every mouse, adding brains to the same tube of douncing buffer (on ice and in the laminar flow hood). Place an overturned lid of a 60 mm dish on top of a

100 mm dish containing packed ice and transfer the brains into the overturned lid. Use a scalpel to cut the brains into  $\sim 1 \text{ mm}^3$  pieces. Pipette 2-3 mL of douncing buffer into the overturned lid, and then tip the douncing buffer + brain pieces mixture into a 15mL dounce grinder (Wheaton #357544) on ice. Raise the volume of douncing buffer to the horizontal line on the dounce grinder, and proceed to dounce with 8-12 slow, gentle strokes, taking care to avoid contact between the pestle and the bottom of the douncer. Place the douncer back on ice, and allow the tissue to settle for 3-4 minutes. Carefully transfer the homogenized supernatant to a fresh tube without disturbing the un-homogenized chunks that remain at the bottom of the douncer. Add more douncing buffer and repeat the above steps, for a maximum of 3 total rounds of douncing. After each round, add the supernatant to the same tube.

### **5.1.3 Myelin removal**

Raise the volume of the collected homogenate to 33.5 mL with douncing buffer, and then add 10mL of isotonic myelin separation buffer (9mL Percoll PLUS [GE Healthcare #17544501], 1mL 10X PBS Buffer pH 7.4 (Thermo Fisher #AM9625), 9 $\mu$ L 1M CaCl<sub>2</sub> [Sigma #21115-100ML], 5 $\mu$ L 1M MgCl<sub>2</sub> [Thermo Fisher #AM9530G]). Invert multiple times to mix thoroughly. Centrifuge at 4 $^{\circ}$  C for 15min at 500 x g with slow braking, and transfer the tube(s) to an ice bucket in a biosafety cabinet. Remove the top layer of debris with a p1000 pipette, ensuring that no debris remains. Remove the cloudy supernatant carefully with a serological pipette, leaving  $\sim 5$ mL remaining at the bottom of the tube. Remove the remaining supernatant carefully with a p100 pipette, leaving only the pelleted cells.

Resuspend the pellet in 1mL ice-cold panning buffer (0.5% peptone in dPBS++, sterile filtered, de-gassed for at least 30min on the day of dissection), and transfer to a pre-wet 20  $\mu$ m

filter (Sysmex #04-004-2325) set in a 15mL tube on ice. Allow the suspension to pass through the filter, and then wash filter with 1mL panning buffer. Continue to wash in 1mL increments, for a final suspension volume of 7-9 mL. Centrifuge at 4° C for 10min at 300 x g with slow braking. Place the tube back on ice in the biosafety cabinet.

#### **5.1.4 Magnetic-activated cell sorting (MACS)**

Resuspend the pellet in 135uL panning buffer, and transfer the suspension to a 1.5mL microcentrifuge tube on ice. Add 15uL CD11b MicroBeads (Miltenyi Biotec #130-093-634) and mix well by flicking the tube. Incubate at 4° C for 15min. Wash with 1mL panning buffer and centrifuge at 4° C for 10min at 300 x g with slow braking. Meanwhile, place 2 MS columns (Miltenyi Biotec #130-042-201) per sample in the appropriate magnets on a MACS separation stand, and wash the column with 500uL panning buffer.

Resuspend the pellet in 500uL panning buffer, and apply the suspension to the first MS column. Allow the suspension to run through the column fully, and then wash 3X with 500uL panning buffer. Remove the column from the magnet and place in the upper reservoir of the second column. Add 1mL of panning buffer, and use the plunger to elute directly into the second column. Wash 3X with 500uL panning buffer. Elute into a fresh 1.5mL microcentrifuge tube with 1mL microglia growth medium (MGM) complete. MGM basal (DMEM/F12 [Thermo Fisher cat. #21331020] with 100 units/mL Penicillin, 100 µg/mL streptomycin, 1mM sodium pyruvate, 1:100 glutamax [Thermo Fisher #35050061], 5 µg/mL insulin [Sigma #I6634-50MG], 100µg/mL apo-transferrin [Sigma #T1147-5x100MG], 100 ng/mL sodium selenite [Sigma #S5261-10G], and 5 µg/mL N-acetyl cysteine [Sigma #A8199-10G], sterile filtered) can be prepared ahead of time. MGM complete (MGM basal with 1.5 µg/mL ovine wool cholesterol

[Avanti Polar Lipids #700000P-1g], 1 µg/mL heparan sulfate [Sigma #H7640-1MG], 0.001 µg/mL gondoic acid [Cayman Chemicals #20606], 0.1 µg/mL oleic acid [Cayman Chemicals #90260], 10 ng/mL M-CSF [Peprotech cat. # 315-02], and 2 ng/mL TGF-B2 [Peprotech cat. # 100-35B]) must be prepared fresh. Fresh MGM complete should be equilibrated in a 50 mL bioreactor (Corning #CLS431720-25EA) in a 37° incubator at 10% CO<sub>2</sub> for at least 30 minutes prior to use.

### **5.1.5 Plating**

Acid-washed coverslips in 24-well plates were previously coated with 0.1mg/mL PDL (Thermo Fisher # A3890401) for at least 1 hour before washing 3X with water. Coverslips are allowed to dry before coating with collagen. Collagen should be thawed slowly on ice from LN<sub>2</sub> storage and diluted immediately before use to 2 µg/mL in MGM basal or complete. Coat coverslips by adding a 60uL collagen bubble to each coverslip and incubating for at least 15min in a 37° incubator. Do not allow the bubble to pop. When cells are ready to plate, remove from incubator and aspirate collagen solution. Do not allow the coverslips to dry.

Count eluted cells and dilute to 1e6 cells/mL in MGM complete. Plate a bubble of 50uL cell suspension (50,000 cells/bubble) on a 12 mm PDL- and collagen-coated coverslip in a 24-well plate, and transfer to a 37° incubator at 10% CO<sub>2</sub>. It is crucial that the bubble remain intact. Different bubble volumes may be used, as long as 50,000 cells are plated and the bubble does not pop. After transferring the bubble-plated suspensions to the incubator, allow the microglia to attach for 30 min. Then, add 450 µL per well of MGM complete, for a final volume of 500 µL. Move the microglia back to the incubator and culture according to experimental needs.

## **5.2 Serum-free isolation and culture of primary midbrain neurons**

Primary midbrain neuron cultures were prepared from neonatal mice using methods approved by the Janelia Research Campus IACUC (protocols #15-129 and #17-152). This protocol is appropriate for a single researcher to isolate primary midbrain neurons from 6-8 mice aged p1. To purify neurons from greater numbers of neonatal mice, it is recommended that multiple researchers work in tandem to minimize the time between dissection and eventual plating. Long periods of waiting lead to increased neuronal death and decreased isolation efficiency.

### **5.2.1 Brain isolation**

Transfer 3-4 p1 pups to a paper towel placed on top of an absorbent mat in an uncoated dissection tray. Decapitate all pups, spray with 70% ethanol, and transfer to an ethanol-soaked paper towel in a laminar flow hood. Use small scissors to cut the skin sagittally on the dorsal side of the head, and move the skin to reveal the skull. Next, cut the skull sagittally, and use blunt tweezers to remove either half of the skull, revealing the cortex. Insert a pre-wetted spatula underneath the brain, remove the brain, and transfer to a 60 mm dish with ~10 mL cold dissection buffer (HBSS [Thermo Fisher #24020117] with 10 mM HEPES, 100 units/mL Penicillin, and 100 µg/mL streptomycin, sterile filtered). To keep the tissue chilled throughout the experiment, we recommend placing the 60cm dish(es) on a metal block set in an ice bucket.

After all brains have been isolated, use a spatula to transfer them to a new 60 mm dish filled with chilled dissection buffer. Place the 60 mm dish on top of a 100 mm dish containing packed ice, and move the stacked dishes to a dissecting microscope in the laminar flow hood.



### 5.2.2 Midbrain dissection

Orient the brain with the dorsal side up and the cerebellum on the left side of the microscope view. Using angled forceps (F.S.T. #00109-11), hold the brain in place firmly but carefully by pinching the midbrain. With a No. 10 (curved) scalpel, cut between the cortical hemispheres to allow access to the underlying structures, without cutting into the structures that are ventral to the cortex. Cut away connective tissue holding the cortical hemispheres in place, and use the scalpel to 'peel' one hemisphere away from the rest of the brain. Repeat for the other hemisphere. Then, remove both hemispheres by cutting sagittally and discard. Make a coronal cut near the forebrain, discarding the rostral fragment. Next, make a cut along the entirety of the midsagittal plane. Orient both pieces such that the midsagittal plane is facing upwards.

Isolate one of the hemi-brains, and pinch the cerebellum with angled forceps to hold the tissue in place, and make a coronal cut rostral to the midbrain. Make another coronal cut caudal to the midbrain. Finally, make an axial cut through to remove the dorsal  $\sim 1/3$  of the midbrain, and retain the ventral midbrain fragment. Transfer this fragment to a fresh 60 mm dish filled with dissection buffer on the chilled metal block. Repeat for the other half of the brain to obtain a second midbrain fragment. Dissect each brain in the same manner, and collect midbrain fragments into the same 60 mm dish.

Once all midbrain fragments have been isolated, move the midbrain dish onto the microscope (on top of the 100 mm dish of packed ice). Using 2 pairs of fine forceps (F.S.T #11252-00), hold the fragment in place with one hand while removing all meninges with the other hand. Dispose of meninges into a waste dish. Repeat for all midbrain fragments, and then

transfer the meninges-free fragments to a new overturned 60 mm lid placed on top of the 100 mm dish of packed ice. The lid should be dry, and there should be minimal carry-over of buffer from the midbrain transfer. Chop the midbrain into fine pieces using the scalpel and add dissection buffer to the dish. Cut the end off of a p1000 tip, and use this 'wide-bore' tip to transfer the pieces to a 15 mL tube on ice. Repeat the addition of buffer and p1000 transfer until no pieces remain in the dish.

### **5.2.3 Papain digestion**

Allow the chopped pieces to settle at the bottom of the 15 mL tube before aspirating the buffer with a p1000. Add 5mL papain solution (1 vial papain [Worthington #LK003178] resuspended in 5mL dissection buffer with 1-3  $\mu$ L benzonase [Sigma #E1014-25KU]) to the tube, and transfer to a 37<sup>o</sup> C water bath. Incubate for 30 min, inverting the tube 3-5 times every 7-8 minutes.

After incubation, invert the tube a final 3-5 times and transfer to an ice bucket in a biosafety cabinet. Allow the tissue to settle at the bottom of the tube and aspirate using a p1000 followed by a p200 (to remove as much papain solution as possible). Resuspend the fragment in 1mL low-OVO solution (1 mL low-ovomuroid 10X stock solution raised to 10 mL with dissection buffer). Low-ovomuroid 10X stock contains 3g BSA and 3g trypsin inhibitor (Worthington #LS003086) in dPBS, with the pH adjusted to 7.4 using ~1 mL of 1 N NaOH for a total volume of 200 mL (sterile filtered). Triturate the resuspended fragments 10 times with a p1000, and allow the tissue fragments to settle. Aspirate the homogenized supernatant and pass through a pre-wet 20  $\mu$ m filter set in a 15 mL tube on ice. Add 1mL low-ovomuroid buffer

and repeat the above trituration and filtration, collecting all supernatant in the same tube. Repeat this step until no tissue pieces remain, for a maximum total of 3 rounds of trituration.

Wash the filter 1 mL at a time with low-OVO solution, until a final volume of 7 mL is obtained. Next, use a 5 mL serological pipette to carefully underlay 4.2 mL high-OVO solution (1 mL high-ovomuroid 6X stock solution raised to 6 mL with dissection buffer) below the cell suspension. High-ovomuroid 10X stock contains 6g BSA and 6g trypsin inhibitor in dPBS, with the pH adjusted to 7.4 using 10 N NaOH for a total volume of 200 mL (sterile filtered). After underlaying the high-OVO solution, a clear lower phase and a cloudy upper phase should be visible. Centrifuge at 4° C for 10 min at 500 x *g*.

#### **5.2.4 MACS purification**

The volumes of antibodies and beads used below are for  $\leq 10^7$  input cells. To purify neurons from  $\geq 10^7$  input cells, consult the Miltenyi Neuron Isolation Kit (mouse) literature. Aspirate the supernatant and resuspend the pellet in 70  $\mu$ L ice-cold panning buffer. Transfer the suspension to a 1.5 mL microcentrifuge tube on ice. Add 20  $\mu$ L of non-neuronal cell biotin-antibody cocktail (one component of Miltenyi #130-115-389) and 10  $\mu$ L CD140a-biotin antibody (Miltenyi #130-101-905) to the suspension and flick the tube multiple times to mix well. Incubate for 10 min at 4° C. Wash with 1 mL panning buffer and centrifuge at 4° C for 10 min at 300 x *g*. Place back on ice. Aspirate the supernatant and resuspend the pellet in 80  $\mu$ L panning buffer. Add 20  $\mu$ L of anti-biotin microBeads (the other component of Miltenyi #130-115-389), and flick to mix well. Incubate for 10 min at 4° C.

Meanwhile, place 1 MS column per sample in the appropriate magnet on a MACS separation stand and wash the column with 500uL panning buffer. After incubation is complete,

place the cell suspension back on ice and add 400  $\mu$ L panning buffer, for a total volume of 500  $\mu$ L. Apply suspension to the column and *collect the flow-through* in a fresh 1.5 mL microcentrifuge tube. Because we are using negative selection, the purified neurons are in the flow-through. Wash 2X with 500  $\mu$ L panning buffer, collecting all flow-through in the same tube. The final volume should be 1.5 mL. Centrifuge the suspension at 4<sup>o</sup> C for 10 min at 300 x *g*.

### **5.2.5 Plating and culture**

Aspirate and resuspend the pellet in 400-1000  $\mu$ L primary neuron culture medium (NBA/B27 with 0.5 mM cAMP [Millipore #28745-100MG], 20 ng/mL BDNF [Peprotech #450-02], 20 ng/mL GDNF [Peprotech #450-10], 4 ng/mL TGF-  $\beta$ 3 [R&D Systems #8420-B3-025]). NBA/B27 is Neurobasal A (Thermo Fisher #10888022) with 2% v/v B27 (Thermo Fisher #17504044), 100 units/mL Penicillin, 100  $\mu$ g/mL streptomycin, and 1:100 glutamax (sterile filtered). Count neurons, dilute to the desired concentration in primary neuron culture medium, and plate. Plate 45,000 cells/well in 100  $\mu$ L in a 96-well plate, or adjust as necessary for different culture vessels. Incubate at 37<sup>o</sup> C with 5% CO<sub>2</sub>.

Regardless of the purification efficiency, some glia will remain in the neuronal culture. The next morning, to prevent the growth of unwanted glia, add an equal volume (100  $\mu$ L for a 96-well plate) of primary neuron culture medium supplemented with 30  $\mu$ M 5-FDU (Cayman Chemicals #14154) to each well. The final concentration of 5-FDU is 15  $\mu$ M. Incubate for 10-12 hours and perform a full medium change with 200  $\mu$ L fresh primary neuron culture medium. Maintain cultures according to experimental needs.

### **5.3 Co-culture of primary microglia and midbrain neurons**

Isolate, plate, and culture primary midbrain neurons from p1 mice as described above. Isolate primary microglia from p12-p15 mice as described above and add microglia to plated neurons in a 96-well plate at a 1:1 microglia: neuron ratio. Culture in a 1:1 mixture of primary neuron culture medium (excluding cAMP) and MGM complete.

### **5.4 Microglia conditioned medium (MCM) culture of midbrain neurons**

MCM experiments were carried out using neurons isolated from p1 pups as described above. After treatment with 5-FDU to prevent glial expansion, medium was changed to a 1:1 mixture of primary neuron culture medium and microglia conditioned medium. MCM was collected at 6 DIV from primary microglia isolated and plated as described above. Debris was cleared by centrifuging MCM at room temperature for 20 min at 1000 x g, and only the supernatant was retained. MCM was stored in aliquots at -80° C.

### **5.5 Immunofluorescence of mouse primary cultures**

Successful immunofluorescence depends on maintaining attachment of primary cells throughout fixation and staining, so care must be taken to aspirate and add solutions gently. Mouse primary cells were cultured on circular coverslips in TC plates or on optically-compatible 96-well plates. After washing 2X with dPBS++, cultures were incubated in 4% formaldehyde (Thermo Fisher # 28906) in dPBS++ for 20 min at room temperature in the dark. Wells were washed 3X with dPBS++ before incubating in blocking buffer (dPBS++ with 5% v/v normal goat serum [Thermo Fisher #31873], 0.3% Triton X-100 [Sigma #T8787-50ML], and 1% w/v BSA [Sigma #A9418-50G]) for 1 hour in the dark at room temperature. After aspirating blocking buffer, the desired primary antibodies in incubation buffer (dPBS++ with 1% w/v BSA) were

added to the wells. Antibodies were diluted as follows: rabbit anti-TH (PhosphoSolutions #2025-THRAB) at 1:500, chicken anti-MAP2 (Thermo Fisher #PA1-10005) at 1:1000, rabbit anti-Iba1 (Wako #019-19741) at 1:500, and mouse anti-GFAP (BD Biosciences #556328) at 1:500. Primary antibody incubation was performed at 4° C overnight.

The next morning, the primary antibodies were aspirated, and the wells were washed 2X with dPBS++. Depending on the desired color combinations and isotype compatibility, appropriate secondary antibodies (all Invitrogen) were diluted to 1:1000 and added to the wells. After incubating with the secondary antibody for 60 minutes, the wells were aspirated and washed 3X with dPBS++. For optical 96-well plates, 200 µL dPBS++ was added to each well, and the plate was sealed with a clear adhesive sealing sheet (Thermo Fisher #AB-0558) and stored at 4° C. Coverslips were mounted with ProLong Gold or Diamond (Thermo Fisher #P36965 or #P36935) and stored at 4°C.

## **5.6 Imaging and quantification of dopaminergic (TH+) neuron survival**

Cultures stained for MAP2 and TH were imaged on a Nikon Eclipse microscope with a 10x air objective. MAP and TH were in either the Cy5 or FITC channels. Nikon's high-content imaging software was used to capture and stitch either 6x6 or 7x7 images per well in a single optical plane. The stitched images were imported into Imaris (Bitplane), and the Spots detection feature was used to identify MAP2+ and MAP2+/TH+ neuronal soma. As MAP2 is expressed across all neurons in our cultures, TH+/MAP2+ soma are considered true TH+ neurons. The number of MAP2+ and TH+ neurons per well were recorded, and TH neuron survival was quantified by calculating the percentage of MAP2+ neurons that were TH+ on a per-well basis. A drop in this percentage indicates loss of TH+ dopaminergic neurons.

## **5.7 Mouse cytokine array**

The Mouse XL Cytokine Array Kit (R&D Systems #ARY028) was used to quantify cytokine levels in conditioned media according to the manufacturer's protocol. Conditioned medium (CM) was collected as described above, and debris was cleared by centrifugation at 1000 x *g* for 20 min. If CM had been previously collected and was stored at -80° C, the tubes of CM were thawed on ice at 4° C (for multiple hours or overnight). On day 1, 1 mL of conditioned medium was combined with 0.5 mL of Array Buffer 4 and applied to a previously-blocked Mouse XL Cytokine Array blot. The blot was incubated overnight with rocking at 4° C. The next day, the detection antibody cocktail, Array Buffer 4/6, 1X Wash Buffer, Chemi Reagent Mix, and 1X Streptavidin-HRP were prepared. The blot was washed and stained according to the manufacturer's protocol, and the array was imaged using the automatic exposure chemiluminescence settings on a ChemiDoc (BioRad) imager. For greater detection sensitivity, SuperSignal West Femto Maximum Sensitivity Substrate (Thermo Fisher #34095) may be used in place of the provided Chemi Reagent Mix.

To quantify the cytokine dot blot, the automated spots detection feature of Imaris (Bitplane) was used. The sum of signal intensity for each spot was recorded, and the sum of signal intensity for a background spot was subtracted to produce a background-corrected intensity.

## **5.8 Bead uptake imaging and analysis**

### **5.8.1 Plating and image acquisition**

Microglia were prepared as described previously (Chapter 5.1), and 45,000 cells/well were plated in 300  $\mu$ L MGM complete on PDL- and collagen-coated 8-well optical coverglass

dishes (Ibidi #80826). At 6-8 DIV, 1 $\mu$ m yellow-green fluorescent beads (Thermo Fisher #F13083) and 170nm deep-red fluorescent beads (Thermo Fisher #P7220) were both added to the wells at concentrations of  $6 \times 10^5$  beads/mL and  $6 \times 10^7$  beads/mL, respectively. After 2h bead incubation, Vybrant Dil lipophilic membrane stain (Thermo Fisher #V22889) was diluted 1:100 into the wells, and microglia were returned to the incubator for 10 min. The cells were then washed gently 3X with pre-warmed MGM basal and fixed in 300uL per well of 4% PFA + 0.1% glutaraldehyde in PBS. After 20 min, the fixative was removed before washing 2X with PBS+DAPI (1  $\mu$ g/mL), followed by replacement with 300uL PBS. It should be noted that in our testing, Dil also successfully stains microglial membranes post-fixation. Each well was imaged at 40x on a Nikon Eclipse spinning disk confocal equipped with Nikon's Perfect Focus System with 405 nm, 488 nm, 561 nm, and 647 nm lasers using Nikon's large image acquisition ("tiling") settings. Generally, between 200-900 fields were acquired per well. In our experience, Nikon Perfect Focus (PFS) is crucial for successful large image acquisition in this experimental setup. If a PFS-enabled system is not available, each field should be acquired manually. In our hands, Zeiss Definite Focus technology does not maintain the focal plane sufficiently in large tiling experiments (as opposed to single-field, time-lapse experiments).

## **5.8.2 Image analysis pipeline**

A custom analysis pipeline was built for the quantification of bead uptake images.

### **5.8.2.1 Cell segmentation**

First, the Ilastik machine learning (ML) software package [186] was used to generate cell masks from data in the Dil (647 nm laser) channel. To generate the masks, representative Dil channel images were imported into the Ilastik Pixel Classification workflow, and images were



annotated to identify true Dil signal (label class #1) vs background (label class #2). After training, a Random Forest pixel classifier was generated and applied to the Dil channel of every image. After the application of the Random Forest pixel classifier, a probability map is generated for each image. Using these probability maps and the original Dil raw data as inputs, the Ilastik Object Classification workflow was used to threshold the probability maps and export cell masks.

#### **5.8.2.2 Cell Identification and splitting of merged masks**

Because cells (and in particular microglia) *in vitro* can form clusters and directly contact other microglia, the high-quality cell masks produced by ML classifiers must be processed further to address merged masks. To this end, FIJI [187] was used to manually mark the approximate center of each cell in every large-field, tiled image. A custom ImageJ Macro (IJM) script was written to extract a 676x676 pixel window centered around each marked point and save each window as a separate image. After this splitting process, each image contains one 'target' cell, but they may also contain other 'non-target' cells. Of particular focus are non-target cells whose masks merge with the target cell. To process these merged masks, a custom IJM graphical user interface (GUI) was written to review every image in the full dataset individually, with options to 1) accept the target mask as-is, 2) split the target mask away from non-target masks by manually drawing a border, or 3) reject the mask entirely. The last option is used to remove poor-quality, un-segmentable, aberrantly annotated, or otherwise unusable masks/cells from the analysis. Importantly, the researcher running the GUI is blinded to the sample type and condition of each cell that is presented during review.

Following GUI review, an IJM script was used to apply these single-cell masks to the corresponding raw data for each 676x676 window. This produces single-cell, cell-masked images with all 4 channels of data. In addition, cell areas were recorded by measuring the size of each cell mask.

### **5.8.2.3 *Per-cell bead quantification***

Cell-masked data from the 1  $\mu\text{m}$  bead (488 nm) and 170 nm bead (647 nm) channels were used as inputs for particle identification with Trackmate [199]. Custom Jython scripts were written to identify and count the number of large and small beads in each cell using Trackmate. Each bead's location was also recorded for distance-based analyses.

### **5.8.2.4 *Nuclear segmentation and analysis***

The DAPI (405) and 1  $\mu\text{m}$  bead (488) channels were used to train an Ilastik ML classifier. Because the 1 $\mu\text{m}$  beads are extremely bright, there is spectral overlap with the adjacent DAPI channel. So, the pixel classifier was trained to recognize DAPI (label class #1) vs background and beads (label class #2). Following thresholding of the probability maps, an ML object classifier was trained to recognize live (label class #1) vs dead (label class #2) nuclei based on the structure of the underlying fluorescent signal. After running the pixel and object classifiers on each image, live nuclear masks were obtained. The masks were linked to individual cells by splitting as described in Chapter 5.8.2.2, and per-cell nuclear measurements (size, number, shape) were computed.

## **5.9 Phagocytosis flow cytometry assay**

Microglia were prepared and plated as described above. Similar to the phagocytosis microscopy assay, 1 $\mu\text{m}$  yellow-green fluorescent beads (Thermo Fisher #F13083) were added to

6-8 DIV microglial cultures at a concentration of  $6 \times 10^5$  beads/mL. After 2h incubation, microglia were harvested using Accumax, resuspended in FACS buffer (dPBS—with 0.1% BSA), and stained with DAPI (1  $\mu\text{g}/\text{mL}$ ). Samples were analyzed via flow cytometry, and gating on DAPI (which preferentially stains dead cells) was used to isolate live microglia populations. Data analysis and visualization were performed in FlowJo (FlowJo, LLC).

## **5.10 Mitochondrial morphology imaging and analysis**

### **5.10.1 Sample preparation and image acquisition**

Microglia were prepared and plated as described previously (Chapters 5.1 and 5.8.1). At 6-8 DIV, microglia were fixed in 4% PFA + 0.2% glutaraldehyde in PBS for 10 minutes, followed by 3 washes with PBS. Cells were then permeabilized for 10 minutes in 0.2% Triton X-100 (Sigma #T8787-50ML) before blocking in 1% BSA (Sigma #A9418-50G) + 5% Normal Goat Serum (Thermo Fisher #31873) + 0.2% Triton X-100 for 1 hour at room temperature. Microglia were stained using 1:400 anti-TOMM20 (Abcam #ab78547) in 1% BSA + 0.2% Triton X-100 and left overnight at 4<sup>o</sup>. The next morning, the wells were washed 3X, followed by secondary staining with 1:1000 Goat anti-Rabbit AF+ 488 (Thermo Fisher #A32731) in 1% BSA + 0.2% Triton X-100. The cells were washed 5X in PBS, with 2 of the washes including 1  $\mu\text{g}/\text{mL}$  DAPI.

The wells were imaged in PBS as described in Section 5.8.1 using the 405 nm (DAPI) and 488 nm (TOMM20) lasers.

### **5.10.2 Image analysis pipeline**

A custom analysis pipeline was built for the quantification of bead uptake images.

### **5.10.2.1 Nuclear segmentation and cell identification**

Rather than employing manual annotation to identify cell locations across large-field, tiled images (*e.g.* Section 5.8.2.2), we instead used our DAPI signal and ML classifiers to determine cell positions. An ML pixel classifier was trained to identify DAPI (label class #1) vs background (label class #2). Using pixel prediction maps and the saturated images as inputs, a ML object classifier was trained to recognize live (label class #1) vs dead (label class #2) nuclei. The pixel and object classifiers were sequentially applied to entire large-field images, and output images containing 3 channels (background, live nuclei, and dead nuclei) were obtained. Using custom IJM code, the live nuclei were isolated and analyzed. For each live nucleus, the centroid and shape were recorded. The positions of the nuclear centroids within the large-field image can be used to extract and save 676x676 windows for each nucleus. This window extraction process is analogous to the extraction based on manual annotations described in Section 5.8.2.2, except that the positions here are derived from automatically-detected nuclei.

### **5.10.2.2 Cell segmentation**

Similar to the cell masking described in Section 5.8.2.1, Ilastik was used to generate a ML classifier. Whereas the bead uptake imaging experiments included a membrane stain (DiI), the mitochondrial morphology experiments did not. However, due to the faint background signal inherent to IF staining and the sensitivity of our microscope, it is possible to reconstruct cell masks by saturating the TOMM20 signal. To achieve this, lookup tables (LUTs) were adjusted in ImageJ to produce a saturated signal throughout the cell area, and an Ilastik ML pixel classifier was trained to discriminate saturated TOMM20 (label class #1) from background (label class

#2). The classifier was applied to every image to produce pixel probability maps. Using custom IJM code, these maps were auto-thresholded and converted into binary masks.

The nuclear centroids identified in the previous section were then used to extract 676x676 windows containing the binary cell mask channel for each live nucleus. As in Section 5.8.2.2, a blinded custom IJM GUI was written with options to 1) accept the target mask as-is, 2) split the target mask away from non-target masks by manually drawing a border, or 3) reject the mask entirely. These cell-specific masks can be applied to any raw channel (or mask/transformation thereof).

### ***5.10.2.3 Mitochondrial segmentation and quantification***

The unsaturated TOMM20 signal was used as an input to train an Ilastik ML pixel classifier for mitochondrial segmentation. The pixel classifier was trained to identify TOMM20 (label class #1) vs background (label class #2). Custom IJM code was used for auto-thresholding and masking, with segmented mitochondrial binary masks generated as the output.

Using the nuclear centroids from Section 5.10.2.1, the segmented mitochondrial masks were extracted into 676x676 windows, and the cell masks above were applied to the corresponding window containing segmented mitochondria (all with IJM code). These processing steps produce single-cell, cell-masked segmented mitochondrial masks. For each cell, we can then measure the 1) number of mitochondria, 2) the size, shape, and position of each mitochondrion, and 3) the area of the cell. In addition, the nuclear masking completed in Section 5.10.2.1 allows us to measure the position, size, and shape of each nucleus.

## **5.11 Lipid droplet (LD) imaging and analysis**

### **5.11.1 Sample preparation and image acquisition**

Microglia were prepared and plated as described previously (Chapters 5.1 and 5.8.1). In preparation for lipid droplet staining, a 1X stock of BODIPY 493/503 (Thermo Fisher #D3922) was freshly prepared for each experiment by diluting a 1 mg/mL stock 1:20,000 into MGM complete. The medium was kept in a bioreactor in the incubator while not in use. At 6-8 DIV, each well's existing medium was removed and reserved in a separate wells of a 24-well dish for later use. 300  $\mu$ L of fresh 1X BODIPY was added to each well, and the cells were incubated with BODIPY for 20 minutes. After 2 gentle washes with pre-warmed MGM basal (or complete), the reserved medium was added back into the original microglial wells. The cells were allowed to equilibrate for 15 minutes before imaging, and Hoechst dye (Thermo Fisher #H21492) was added to a final concentration of 1  $\mu$ g/mL prior to imaging.

An LSM 880 with Airyscan (Carl Zeiss Microscopy GmbH) was used to image lipid droplets in live cells at 63x magnification. Images of at least 50 cells per condition were acquired with BODIPY (488 nm laser) and Hoechst (405 nm laser) channels, and the acquisition settings were optimized for Nyquist sampling at 488 nm. Following image acquisition, Zen (Carl Zeiss Microscopy GmbH) was used to apply Airyscan deconvolution [230] to each image.

### **5.11.2 Image analysis pipeline**

A custom analysis pipeline was built for the quantification of bead uptake images.

#### **5.11.2.1 Cell segmentation**

Ilastik was used to generate a ML pixel classifier for cell masking. Although BODIPY preferentially enriches in lipid droplets [189, 231], it also faintly stains the plasma membrane

(PM). As a result, saturation of the BODIPY signal enables visualization of the PM and subsequent cell masking. First, the BODIPY channel was saturated using custom IJM code. To isolate masks, an Ilastik ML pixel classifier was trained to discriminate BODIPY signal (label class #1) from background (label class #2). After running the classifier on every image to produce pixel prediction maps, custom IJM code was used to auto-threshold the data and produce binary cell masks.

As in Section 5.8.2.2, a blinded custom IJM GUI was used to further process the masks. All images were processed with options to 1) keep a single mask from the image (if there is only one cell), 2) split multiple masks from the image (if there are multiple cells), or 3) reject the image entirely. The masks output from this code are used in later analyses.

#### ***5.11.2.2 Lipid droplet segmentation and quantification***

Similar to the mitochondrial segmentation in Section 5.10.2.3, the unsaturated BODIPY signal was the input for training a lipid droplet segmentation classifier in Ilastik. The ML classifier was trained to identify lipid droplets (label class #1) vs background (label class #2). After applying the classifier to every image, the resulting prediction maps were auto-thresholded and converted to lipid droplet masks. The cell masks generated in the previous step were then applied to the LD masks to produce single-cell, cell-masked segmented lipid droplet masks. Using the cell masks and cell-masked LD masks, we can measure 1) the number of LDs, 2) the size, shape, and position of each LD, and 3) the area of the cell.

#### ***5.11.2.3 Nuclear segmentation and analysis***

An Ilastik pixel classifier was trained to discriminate nuclear Hoechst signal (label class #1) from background (label class #2). After running the classifier on every image, the resulting pixel

prediction maps were auto-thresholded and converted to binary masks using custom IJM code. Because the live-cell Hoechst signal was less amenable to automated segmentation than fixed-cell DAPI signals, a custom IJM GUI was written to manually review the nuclear masks. With this GUI, the blinded reviewer can 1) accept the masks, 2) manually draw new masks, or 3) indicate that the Hoechst signal was not amenable to either automated or manual segmentation. The previously-generated cell masks were then applied to the nuclear masks that were output by the GUI. As in previous analyses, we used custom IJM code to measure the size, shape, and position of each nucleus.

## **5.12 Endosome maturation imaging and analysis**

### **5.12.1 Sample preparation and image acquisition**

Microglia were prepared and plated as described previously (Chapters 5.1 and 5.8.1). In preparation for endosome imaging experiments, stocks of 1000X TMR-dextran (fixable, Thermo Fisher #D1817) and FITC-dextran (fixable, Thermo Fisher #D1820) were prepared by dissolving 25 mg of dextran into 100 mL ddH<sub>2</sub>O. The dextrans were combined in MGM complete to prepare a stock solution that contained 100X TMR-dextran and 100X FITC-dextran.

For the time lapse endosome maturation experiment, the 100X dual-dextran mixture was diluted to 1X in each microglia well. After addition of the dextran mixture, the culture medium was very gently mixed by repeated pipetting with a p200. The cells were returned to the incubator for 5, 15, or 30 minutes. Following the incubation period, the microglia were fixed in 4% PFA + 0.1% glutaraldehyde in PBS for 20 minutes and washed gently 3X with PBS.

The wells were imaged in PBS as described in Section 5.8.1 using the 405 nm (DAPI), 488 nm (FITC-dextran), and 651 nm (TMR-dextran) lasers.



## **5.12.2 Image analysis pipeline**

A custom analysis pipeline was built for the quantification of endosome maturation data.

### ***5.12.2.1 Nuclear segmentation and cell identification***

The ML classifiers described for nuclear segmentation in the mitochondrial morphology experiments (Section 5.10.2.1) were applied to both the steady-state and time-lapse endosome maturation data. After applying the DAPI pixel prediction classifier and the live/dead object classifier to these images, custom IJM code was used to extract the centroid and shape of each live nucleus. As with the mitochondrial experiments, the nuclear centroids were used as seeds for extracting 676x676 windows around each live nucleus in the large-field, tiled images.

### ***5.12.2.2 Cell segmentation***

The available dye for membrane staining in a spectral region distinct from the spectra of FITC and TMR was Vybrant DiO (Thermo Fisher #V22889). However, in validation experiments, this very bright far-red dye showed significant spectral overlap with the much dimmer TMR-dextran. Instead, an ML classifier was trained on combined and saturated TMR+FITC channels to segment the dextran-labeled regions of microglial cells (Figure 15c), and these masks were used as approximate microglial cell masks. The pixel classifier was trained to identify saturated TMR+FITC cell masks (label class #1) vs background (label class #2). After applying the ML pixel classifier to all images, custom IJM code auto-thresholded and binary masked the resulting pixel prediction maps.

As in Section 5.10.2.2 of the mitochondrial analysis, the nuclear centroids identified above provided seeds for the extraction of 676x676 windows with cell mask data for each nucleus-seeded window. Similar to the mitochondrial processing, a blinded IJM GUI was used to

1) accept the target mask as-is, 2) split the target mask away from non-target masks by manually drawing a border, or 3) reject the mask entirely. After this manual review process, single-cell masks are ready for downstream applications.

### **5.12.2.3 Quantification of endosome immaturity**

Using custom IJM code, the cell masks were applied to the TMR-dextran and FITC-dextran data to obtain cell-masked raw images in each channel. The integrated density of the fluorescence intensity across each cell was measured in both channels. For every cell, the integrated intensity of the TMR-dextran (pH-insensitive) signal was divided by the integrated intensity of the FITC-dextran (pH-sensitive) signal to produce an “endosome maturity” ratio for each cell, which were then normalized to the data range of all conditions in a given experiment.

## **5.13 Microtubule dynamics imaging and analysis**

Microglia were prepared and plated as described previously (Chapter 5.1 and 5.8.1). In preparation for microtubule imaging experiments, a 1 mM stock of SiR-tubulin (Cytoskeleton, Inc.) was prepared by dissolving 50 nmol of SiR-tubulin in 50  $\mu$ L DMSO. SiR-tubulin was diluted into MGM complete to a concentration of 100 nM, and microglia were incubated with 100 nM SiR-tubulin for 12h. The next day, time lapses of live tubulin-labeled microglia were imaged at 63x magnification with 30s intervals on an LSM 880 microscopy with Airyscan detector (Zeiss GmbH). Airyscan deconvolution was applied to the time lapses using the Zen software package (Zeiss GmbH). To quantify MT recovery velocity in microglial lamellipodia, we tracked and quantified the motion of individual microtubules using the ImageJ Manual Tracking plugin.

## 5.14 Migration and chemotaxis assays

In preparation for the migration and chemotaxis assay, culture media and specialized culture dishes were prepared. In addition to standard MGM complete, 10 mL of MGM complete + ADP was prepared by diluting ADP (stock prepared with Sigma #A2754-500MG) into MGM complete to a final concentration of 100  $\mu$ M. Additionally, transwell cell culture inserts in a 24-well dish (polycarbonate, 5  $\mu$ m pore size; Corning #3421) were coated with PDL for 1 hour at room temperature and washed 3X with ddH<sub>2</sub>O.

Microglia were isolated from neonatal pups as described previously (Section 5.1). Prior to the addition of cells, 500  $\mu$ L of medium (with or without ADP) was added to the well below the transwell insert. The PDL-coated inserts were then added to each well, and 100  $\mu$ L of a  $1 \times 10^6$  cells/mL microglia suspension ( $1 \times 10^5$  cells/well) in MGM complete was added to the inside of the transwell insert. The cells were incubated at 37<sup>o</sup> and 10% CO<sub>2</sub> for 4 hours.

Following the incubation period, the supernatant above each transwell insert was carefully aspirated. The inserts were transferred to clean wells containing 400  $\mu$ L per well of Accumax (Innovative Cell Technologies #AM105-500) and returned to the incubator for 30 minutes. The medium in the lower portion of each well—which contains the chemoattractant and any cells that migrated through the membrane and into suspension—was reserved for later use.

During this incubation step, CyQUANT Direct Cell Proliferation Assay reagents (Thermo Fisher #C35011) were prepared according to the manufacturer's protocol. Following the incubation with Accumax, microglia were detached from the bottom of the transwell membrane by tilting the insert 10 times in the Accumax solution. After detachment, the inserts

were discarded. The reserved medium containing migrated suspension microglia and the detachment solution containing migrated adherent microglia were combined, transferred to a 1.5 mL microcentrifuge tube, and centrifuged for 10 minutes at 300xg. 500  $\mu$ L of supernatant was aspirated, leaving 400  $\mu$ L of cell suspension in the tube. 100  $\mu$ L of this suspension was mixed with 100  $\mu$ L of 2X CyQUANT detection reagent and transferred to a clear-bottom, black 96-well plate (Corning #3603). The plate was placed in a 37 $^{\circ}$  incubator for 60 minutes, and fluorescence was measured at the bottom of each well with a SPARK plate reader (Tecan Group Ltd.) using an excitation wavelength of 508 nm and an emission wavelength of 527 nm.

### **5.15 Reverse transcription and qPCR**

RNA was purified from live cells using the Direct-zol RNA MiniPrep kit (Zymo Research #R2050) according to the manufacturer's protocol (including the optional in-column DNase treatment). RNA concentrations were determined using the Qubit RNA HS assay kit (Thermo Fisher #Q32852) on the Qubit 3.0 fluorometer (Thermo Fisher #Q33216). Following quantification, equal amounts of RNA per sample (generally 25-100 ng, depending on the experiment) were reverse transcribed using the SuperScript IV VILO system (Thermo Fisher #11766050) according to the manufacturer's protocol. qPCR was performed on cDNA templates in a 15  $\mu$ L reaction volume using either the KAPA SYBR FAST qPCR kit (for SYBR-based qPCR; Kapa Biosystems #KK4602) or the PrimeTime Gene Expression Master Mix (for probe-based qPCR; IDT #1055772). The  $C_t$  value for the target gene was normalized to the  $C_t$  value of a reference gene (either *HPRT1* or *RPLP0*) to determine  $\Delta C_t$  for the target gene. The  $\Delta C_t$  values were normalized to an arbitrary reference sample (wild-type microglia for Figure 2a and

Figure 9c) to calculate  $\Delta\Delta C_t$ . This value was then converted to normalized mRNA level by calculating  $2^{-\Delta\Delta C_t}$ .

## 6 APPENDIX

### 6.1 Supplementary Figures and Tables

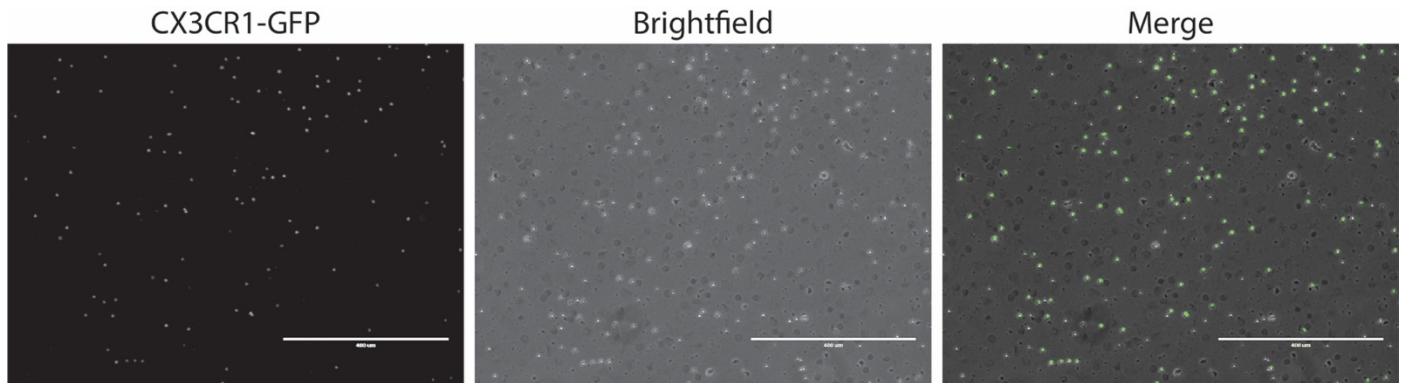


**Figure 20 - Ad hoc evaluation of CX3CR1-GFP expressing cells in post-dounce suspension**

Midway through our microglial isolation from a mouse line expressing GFP from the CX3CR1 promoter, we add a small volume of our post-douncing cell suspension to a hemocytometer slide and imaged the cell suspension on an EVOS FL microscope. Although douncing is typically employed to lyse cells in a tissue/sample, microglia are small enough to escape lysis. As such, we observed a high proportion of GFP-positive microglial cells in this dounced suspension. Because microglia are in suspension, they adopt a small, spherical morphology that differs from the extended and ramified morphology typically observed *in vivo* and in plated primary culture.

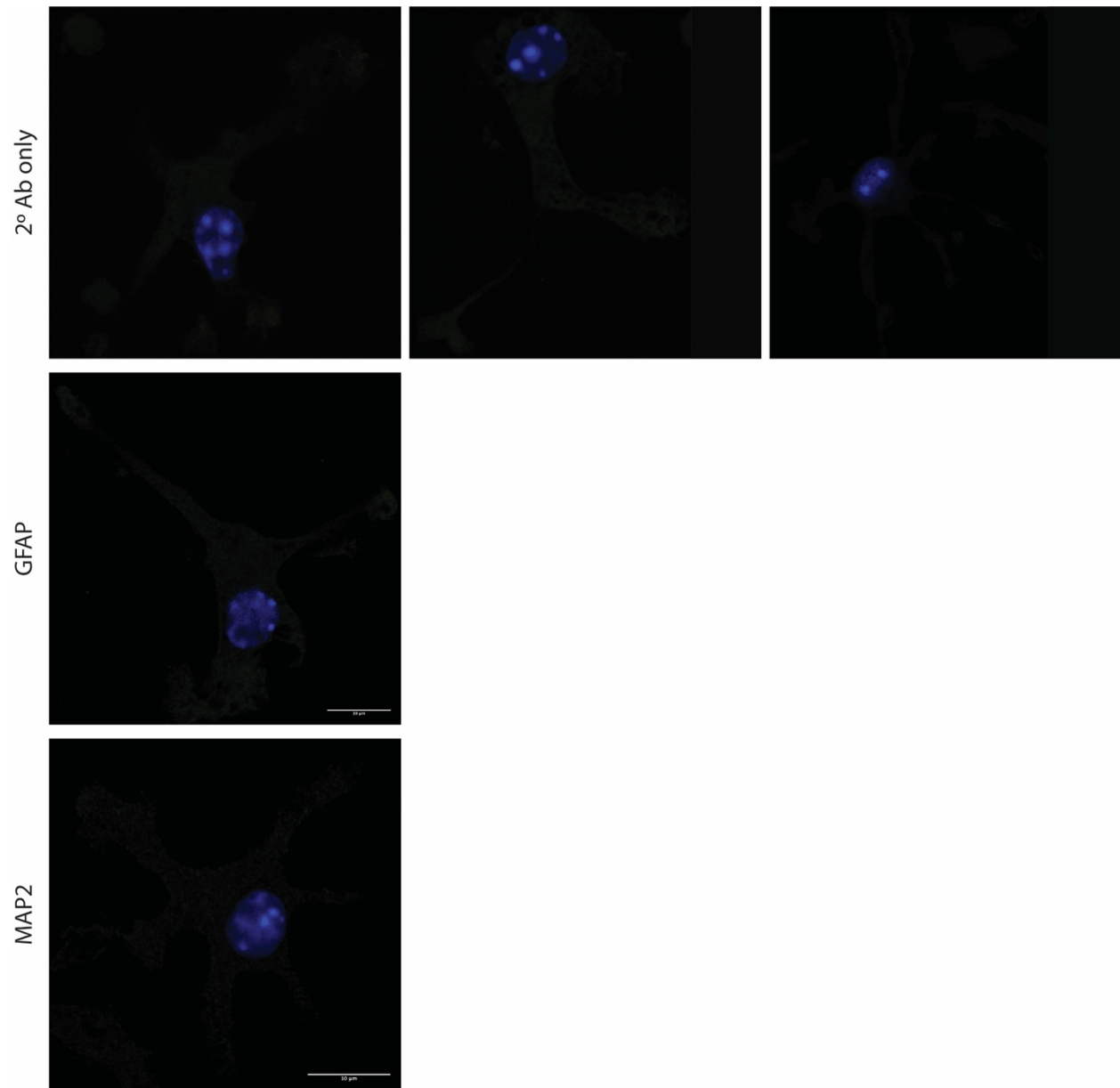


**Figure 21 - Absence of non-specific, astrocyte, or neuron staining in primary MG immunofluorescence**

Microglia were fixed, stained and imaged as described in Figure 2. We did not observe staining above background using secondary antibody alone or with GFAP (astrocyte) and MAP2 (neuronal) primary antibodies.

**Table 2 - Cytokines analyzed in membrane sandwich-based immunoassays**

|                    |                  |                  |                           |
|--------------------|------------------|------------------|---------------------------|
| Adiponectin/Acrp30 | CXCL9/MIG        | IL-2             | PDGF-BB                   |
| Amphiregulin       | CXCL10/IP-10     | IL-3             | Pentraxin                 |
| Angiopoietin-1     | CXCL11/I-TAC     | IL-4             | Pentraxin                 |
| Angiopoietin-2     | CXCL13/BLC/BCA-1 | IL-5             | Periostin/OSF-2           |
| Angiopoietin-like  | CXCL16           | IL-6             | Pref-1/DLK-1/FA1          |
| BAFF/BLyS/TNFSF13B | Cystatin         | IL-7             | Proliferin                |
| C1q                | DKK-1            | IL-10            | Proprotein                |
| CCL2/JE/MCP-1      | DPPIV/CD26       | IL-11            | RAGE                      |
| CCL3/CCL4/MIP-1a/β | EGF              | IL-12            | RBP4                      |
| CCL5/RANTES        | Endoglin/CD105   | IL-13            | Reg3G                     |
| CCL6/C10           | Endostatin       | IL-15            | Resistin                  |
| CCL11/Eotaxin      | Fetuin           | IL-17A           | E-Selectin/CD62E          |
| CCL12/MCP-5        | FGF              | IL-22            | P-Selectin/CD62P          |
| CCL17/TARC         | FGF-21           | IL-23            | Serpin                    |
| CCL19/MIP-3β       | Flt-3            | IL-27            | Serpin                    |
| CCL20/MIP-3a       | Gas              | IL-28A/B         | Thrombopoietin            |
| CCL21/6Ckine       | G-CSF            | IL-33            | TIM-1/KIM-1/HAVCR         |
| CCL22/MDC          | GDF-15           | LDL              | TNF-a                     |
| CD14               | GM-CSF           | Leptin           | VCAM-1/CD106              |
| CD40/TNFRSF5       | HGF              | LIF              | VEGF                      |
| CD160              | ICAM-1/CD54      | Lipocalin-2/NGAL | WISP-1/CCN4               |
| Chemerin           | IFN-?            | LIX              | CXCL2/MIP-2               |
| Chitinase          | IGFBP-1          | M-CSF            | IL-1ra/IL-1F3             |
| Coagulation        | IGFBP-2          | MMP-2            | PD-ECGF/Thymidine         |
| Complement         | IGFBP-3          | MMP-3            | CXCL1/KC                  |
| Complement         | IGFBP-5          | MMP-9            | IL-1β/IL-1F2              |
| C-Reactive         | IGFBP-6          | Myeloperoxidase  | Osteoprotegerin/TNFRSF11B |
| CX3CL1/Fractalkine | IL-1a/IL-1F1     | Osteopontin      |                           |



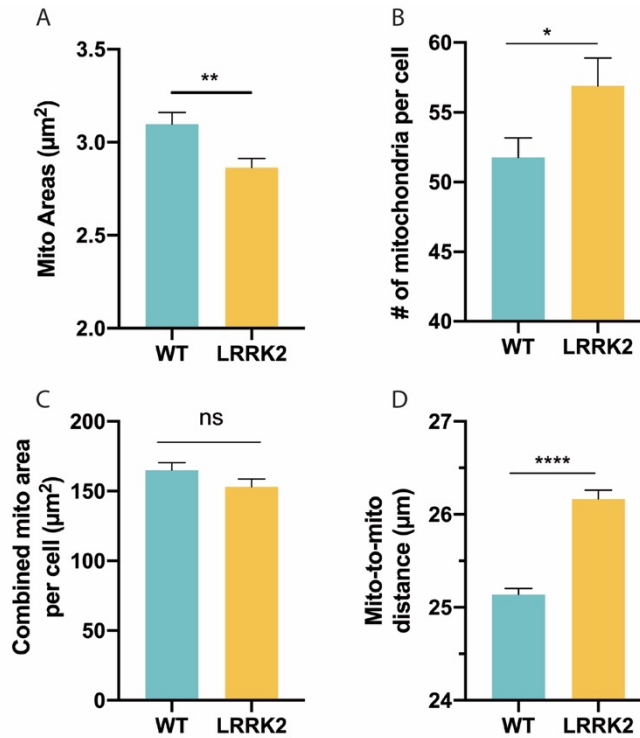


**Figure 23 - Biological repeat results for mitochondrial morphology analysis**

A second biological repeat of the mitochondrial morphology microscopy assay shows that the relationships between wild-type and *LRRK2* G2019S microglia were replicated. The repeat experiment was carried out and analyzed as described in Figure 11. (a) Area per mitochondria is significantly reduced in the *LRRK2* mutant, whereas (b) the number of mitochondria per cell is increased in the *LRRK2* G2019S mutant. (c) The total area of mitochondria per cell is similar in both genotypes. (d) Average mitochondria-to-mitochondria distances within cells are increased in the *LRRK2* G2019S mutant. Statistical tests: two-sided Student's t-test (a, b, c, d). \* $P < 0.05$ , \*\* $P < 0.01$ , \*\*\*\* $P < 0.0001$ , ns = not significant. Error bars are mean  $\pm$  standard error.

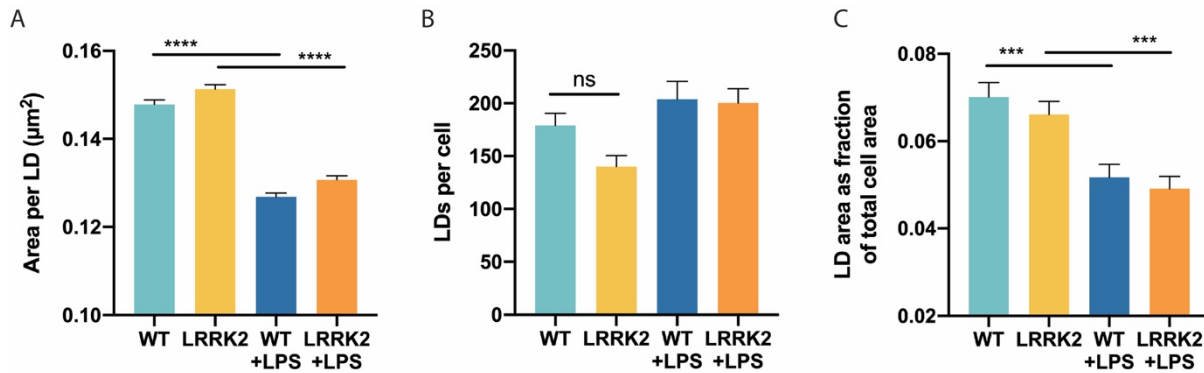


**Figure 22 - Biological repeat results for lipid droplet microscopy assay**

A second biological repeat of the LD microscopy assay shows that the relationships between wild-type and *LRRK2* G2019S microglia were replicated. The repeat experiment was carried out and analyzed as described in Figure 13. (a) Quantification of the area per lipid droplet, (b) number of lipid droplets per cell, and (c) lipid droplet area fraction across genotypes and LPS conditions. Statistical tests: one-way ANOVA with Tukey's post hoc test (a, b, c). \*\*\* $P < 0.001$ , \*\*\*\* $P < 0.0001$ , ns = not significant. Error bars are mean  $\pm$  standard error.

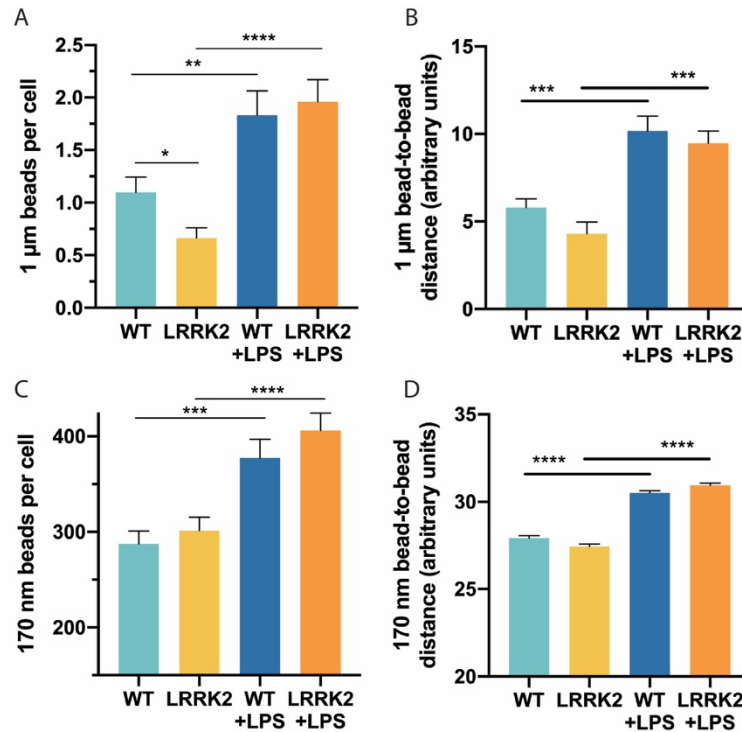


**Figure 25 - Biological repeat results for bead uptake assay**

A second biological repeat of the bead uptake microscopy assay shows that the relationships between wild-type and *LRRK2* G2019S microglia were replicated. The repeat experiment was carried out and analyzed as described in Figure 14. The (a) number of 1  $\mu\text{m}$  beads per cell, (b) 1  $\mu\text{m}$  bead-to-bead distance, (c) number of 170 nm beads per cell, and (d) 170 nm bead-to-bead distance were computed across all genotypes and LPS conditions. Statistical tests: one-way ANOVA with Tukey's post hoc test (a, b, c, d). \* $P < 0.05$ , \*\* $P < 0.01$ , \*\*\* $P < 0.001$ , \*\*\*\* $P < 0.0001$ . Error bars are mean  $\pm$  standard error.

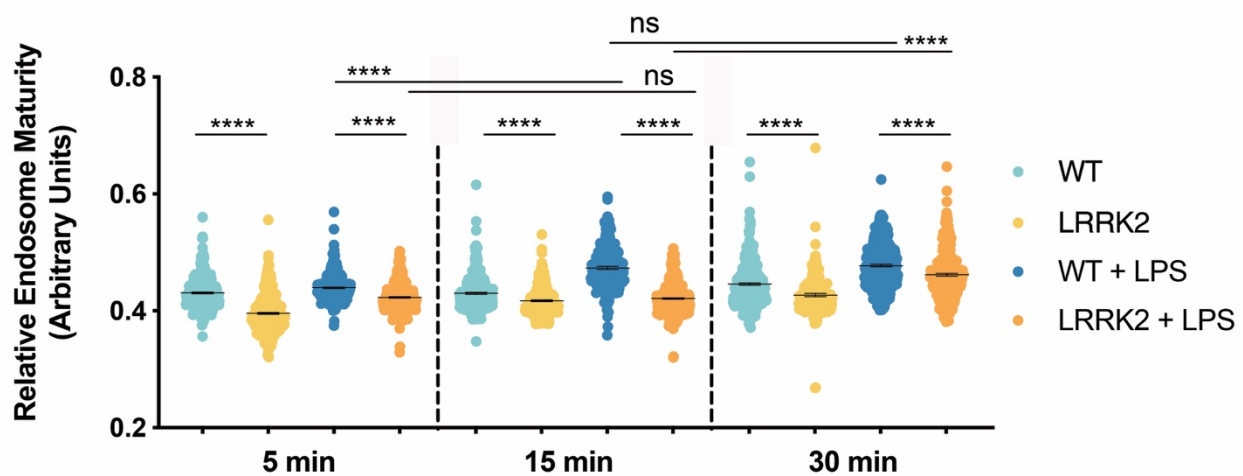


**Figure 24 - Biological repeat results for endosome maturation assay**

A second biological repeat of the endosome maturation assay shows that the relationships between wild-type and *LRRK2* G2019S microglia were replicated. The repeat experiment was carried and analyzed out as described in Figure 15. Calculating the TMR (pH-insensitive) to FITC (pH-sensitive) ratio in each cell generates endosome maturity indices, which are plotted across all time points, genotypes, and LPS conditions. Statistical tests: one-way ANOVA with Tukey's post hoc test (f). \*\* $P < 0.01$ , \*\*\* $P < 0.001$ , \*\*\*\* $P < 0.0001$ . Error bars are mean  $\pm$  standard error.

## 6.2 Image analysis code

### 6.2.1 Mitochondrial morphology analysis

#### 6.2.1.1 *Convert\_ND2\_to\_TIF.ijm (also used in bead uptake and endosome experiments)*

```
input = getDirectory("Choose Target Directory: ");
parent = File.getParent(input);
output4 = parent + "\\all_files_16bit\\";
list = getFileList(input);
File.makeDirectory(output4);
setBatchMode(true);
for (i = 0; i < list.length; i++) {
    filename=list[i];
    Matt4(input, filename);
}
function Matt4(input, filename) {
    L=lengthOf(filename);
    filebase=substring(filename,0,L-4); //it's an .nd2
    fileout = filebase + ".tif";
    run("Bio-Formats Importer", "open=" + input +filename + "
color_mode=Default view=Hyperstack stack_order=XYCZT");
    saveAs("Tiff", output4+fileout);
    imgID = getImageID();
    run("Close All");
    run("Clear Results");
}
```

#### 6.2.1.2 *split\_and\_save.ijm (also used in bead uptake and endosome experiments)*

```
input = getDirectory("Choose Target Directory: ");
parent = File.getParent(input);
output1 = parent + "\\all_files_16bit_C1\\";
output2 = parent + "\\all_files_16bit_C2\\";
output5 = parent + "\\all_files_8bit_C1\\";
output6 = parent + "\\all_files_8bit_C2\\";
output8 = parent + "\\all_files_8bit\\";
list = getFileList(input);
File.makeDirectory(output1);
File.makeDirectory(output2);
File.makeDirectory(output5);
File.makeDirectory(output6);

File.makeDirectory(output8);
setBatchMode(true);
for (i = 0; i < list.length; i++) {
    filename=list[i];
    Matt4(input, filename);
}
function Matt4(input, filename) {
    L=lengthOf(filename);
    filebase=substring(filename,0,L-4); //it's an .nd2
    fileout = filebase + ".tif";
```

```

        //run("Bio-Formats Importer", "open=" + input +filename + "
color_mode=Default view=Hyperstack stack_order=XYZCT");
        open(input+filename);
        imgID = getImageID();
        run("Duplicate...", "duplicate");
        imgID2 = getImageID();
        selectImage(imgID);
        //saveAs("Tiff", output4+fileout);
        imgID = getImageID();
        run("Split Channels");
//Get each 16-bit channel and duplicate. get the title of both copies.
//Saving changes the image/window title, and all images are saved with the
same name (but separate folders), so we need to wait until after merging to
save.
        selectImage("C1-" + fileout);
        c1=getTitle();
        saveAs("Tiff", output1+fileout);
        run("Close");

        selectImage("C2-" + fileout);
        c2=getTitle();
        saveAs("Tiff", output2+fileout);
        run("Close");
//Same as above, but convert to 8-bit first
        selectImage(imgID2);
        close("\\Others"); //this closes every image except the selected one
(e.g. close everything 16-bit so that we only have the duplicated 3-channel
image open)
        run("8-bit");
        saveAs("Tiff", output8+fileout);
        run("Split Channels");
        selectImage("C1-" + fileout);
        c1a = getTitle();
        saveAs("Tiff", output5+fileout);
        run("Close");
        selectImage("C2-" + fileout);
        c2a = getTitle();
        saveAs("Tiff", output6+fileout);
        run("Close");
        run("Close All");
        run("Clear Results");
}

```

### **6.2.1.3 process\_nuclear\_mask\_v3.ijm**

```

input = getDirectory("Choose experiment folder: ");
obj_pred = input + "Object_Predictions_nuclear\\";
output = input + "Live_nuclei\\";
output_ROI = input + "Live_ROI_points\\";
output_nuclear_ROI = input + "Live_ROI_full_nucleus\\"
fileList = getFileList(obj_pred);
File.makeDirectory(output);
File.makeDirectory(output_ROI);
File.makeDirectory(output_nuclear_ROI);
setBatchMode(true);
for (i = 0; i < fileList.length; i++) {

```

```

        filename=fileList[i];
        Matt1(input, filename);
    }
function Matt1(input, filename) {
    open(obj_pred+filename);
    L=lengthOf(filename);
    filebase=substring(filename,0,L-4);
    imageID = getTitle();
//multiply by 10 to get wider range, and then threshold around 10 (value of
live was 1 before x10)
    run("Multiply...", "value=10");
    setThreshold(5, 14);
    setOption("BlackBackground", true);
    run("Convert to Mask");
    run("Fill Holes");
    live_only = getImageID();
    saveAs("Tiff", output+filebase+".tif");
    run("Analyze Particles...", "display add");
    roiManager("Save", output_nuclear_ROI + filebase + ".zip");
    roiManager("Delete");
    roiManager("Reset");

    numberOfPoints = getValue("results.count");
    XM = newArray(numberOfPoints);
    YM = newArray(numberOfPoints);
        for (i=0; i<numberOfPoints; i++) {
            XM[i] = getResult("XM", i);
            YM[i] = getResult("YM",i);
        }
    makeSelection("point", XM, YM);
    roiManager("Add");
    roiManager("Save", output_ROI + filebase + ".roi");
    roiManager("Delete");
    roiManager("Reset");
    run("Close All");
    run("Clear Results");
}

```

#### **6.2.1.4 HDF5\_to\_8bit\_TIF.ijm (also used in endosome and LD experiments)**

```

dataDir = getDirectory("Choose Experiment Directory: ");
pixel_prob = dataDir + "Probabilities_cellMask\\";
output = dataDir + "cellMask_raw_TIFs\\";
fileList = getFileList(pixel_prob);
File.makeDirectory(output);
axisOrder = "yxc";
//inputDataset = "[/exported_data: (4152, 5328, 1) float32]";
inputDataset = "/exported_data";
// DO NOT SET BATCH MODE TO TRUE. It appears to mess up the Ilastik import
plugin.
//setBatchMode(true);
for (i = 0; i < fileList.length; i++) {
    // import image from the H5
    L=lengthOf(fileList[i]);
    filebase=substring(fileList[i],0,L-3);
    fileName = pixel_prob + fileList[i];

```

```

importArgs = "select=" + fileName + " datasetname=" + inputDataset + "
axisorder=" + axisOrder;
run("Import HDF5", importArgs);
imageID=getTitle();
newFile = output+filebase+".tif";
saveAs("Tiff", newFile);
run("Close All");
open(newFile);
run("Split Channels");
selectImage(1);
c1=getTitle();
selectImage(2);
c2=getTitle();
selectWindow(c2);
close();
selectWindow(c1);
run("8-bit");
//setMinAndMax(100, 5000)
saveAs("Tiff", output+filebase+".tif");
run("Close All");
}

```

### **6.2.1.5 Threshold\_8bit\_Prob\_CellMaskTom20\_v2.ijm**

```

input = getDirectory("Choose Experiment Directory: ");
output = input + "cellMask_thresholded\\";
masks = input + "cellMask_raw_TIFs\\";
fileList = getFileList(masks);
File.makeDirectory(output);
for (i = 0; i < fileList.length; i++) {
    filename=fileList[i];
    Matt1(masks, filename);
}
//setBatchMode(false);
function Matt1(masks, filename) {
    open(masks+filename);
    L=lengthOf(filename);
    filebase=substring(filename,0,L-4);
    setAutoThreshold("Default dark");
    run("Create Mask");
    originalMask = getImageID();
    run("Duplicate...", " ");
    smallMask = getImageID();
    run("Analyze Particles...", "size=4000-Infinity add");
    setForegroundColor(0,0,0);
    roiManager("Fill");
    imageCalculator("Subtract create", originalMask, smallMask);
    setForegroundColor(255, 255, 255);
    saveAs("Tiff", output+filebase+".tif");
    roiManager("Delete");
    roiManager("Reset");
    run("Close All");
}

```

### 6.2.1.6 *MattCellSplitter3\_leading\_zeros\_buffer.ijm (also used in endosome experiments)*

```
input = getDirectory("Choose Target Directory: ");
parent = File.getParent(input);
list = getFileList(input);
rois = parent + "//Live_ROI_points//";
File.makeDirectory(input+"Results/");
File.makeDirectory(input+"CellImages/");
setBatchMode(true);
for (i = 0; i < list.length; i++) {
    filename=list[i];
    MattCellMask(input, filename);
}
function MattCellMask(input, filename){
    //Define the file naming scheme:
    L=lengthOf(filename);
    filebase=substring(filename,0,L-4);
    // Open the image
    //run("Bio-Formats", "open=" + input +"Tifs/" + filename + "
autoscale color_mode=Default view=Hyperstack stack_order=XYCZT");
    open(input+filename);
    imageID=getTitle();
    h=getHeight();
    w=getWidth();
    roiManager("reset");
    roiManager("open", rois +filebase+".roi");
    roiManager("measure");
    Roi.getCoordinates(x,y);
    for (j=0; j<nResults; j++){
        imagelabel="_Data";
        makeRectangle(x[j]-338,y[j]-338,676,676);
        roiManager("Add");
        roiManager("Select", 1);
        run("Duplicate...", "duplicate");
        if (x[j]-338<=0){
            imagelabel=imagelabel+"_L";
        }
        if (y[j]-338<=0){
            imagelabel=imagelabel+"_T";
        }
        if (x[j]+338>=w){
            imagelabel=imagelabel+"_R";
        }
        if (y[j]+338>=h){
            imagelabel=imagelabel+"_B";
        }
        //*****only un-comment this line if you want to
change the LUTs for the split images.
        //However, if they are already 8bit, changing the
LUTS and saving wont reset the LUTs to the new value. Need to run "Apply
LUTs" before saving*****
        //setMinAndMax(257,1028);
        //run("8-bit");
        //run("Enhance Contrast", "saturated=0.35");
        jStr = toString(j);
        if (j<10){
```

```

        jZero = "000" + jStr;
    }
    else if (j<100){
        jZero = "00" + jStr;
    }
    else if (j<1000){
        jZero = "0" + jStr;
    }
    else {
        jZero = jStr;
    }
}
saveAs("Tiff",input+"CellImages/"+filebase+"_"+jZero+imagelabel+".tif");

        close();
        roiManager("select", 1);
        roiManager("delete");
    }
    selectWindow("Results");
    saveAs("text",input+"Results/"+filebase+"_results.txt");
    run("Close All");
    run("Clear Results");
    roiManager("Reset");
}

```

### 6.2.1.7 *MattCellAnalyzerGUI5.ijm*

```

//Dialog.setLocation(x,y)
dir1 = getDirectory("Choose Source Directory: ");
input = dir1 + "all_files_8bit_C1\\CellImages\\";
mask = dir1 + "cellMask_thresholded\\CellImages\\";
output1 = dir1 + "Correct\\";
output2 = dir1 + "Incorrect\\";
output3 = dir1 + "DilatedMasks\\";
output4 = dir1 + "Incorrect_no_mask\\";
list = getFileList(input);
File.makeDirectory(output1);
File.makeDirectory(output2);
File.makeDirectory(output3);
File.makeDirectory(output4);
for (i = 0; i < list.length; i++) {
    filename=list[i];
    MattGUI4(input, filename);
}
function MattGUI4(input, filename){
    L=lengthOf(filename);
    filebase=substring(filename,0,L-4);
    open(input+filename);
    print(filebase);
    imageID=getImageID();
    //Find the center of the original image and identify if it is in the
    expected place
    h=getHeight();
    w=getWidth();
    x=338;
    y=338;
    if(w!=676){

```



```

        left=indexOf(filebase,"_L");
        right=indexOf(filebase,"_R");
        if(left!=-1){
            x=w-338;
        }
    }
    if(h!=676){
        top=indexOf(filebase,"_T");
        bottom=indexOf(filebase,"_B");

        if(top!=-1){
            y=h-338;
        }
    }

    //Prep the image for viewer inspection
    run("Duplicate...", " ");
    run("RGB Color");
    w1=getTitle();
    open(mask+filename); //Cell masks and one-channel TOM20 cell images
both have the exact same name (different folders)
    imageID2=getImageID();
    //Test if the center pixel is in a cell mask
    selectImage(imageID2);
    Center=getPixel(x,y);
    //Continue with visualization
    run("Duplicate...", " ");
    w2=getTitle();
    run("8-bit");
    run("RGB Color");
    run("Combine...", "stack1="+w1+" stack2="+w2);
    setLocation(600,600);
    // If the center is not in a mask, throw it into a special folder
    if(Center==0){
        selectImage(imageID);
        saveAs("Tiff", output4+filename);
        run("Close All");
    }
    // If the center is in the mask:
    if(Center!=0){
        A=getNumber("Do you need to split cells? 1 - No 2 - Yes 3 - Discard:",
1);
        if(A==1){
            //Proceed with preparing the mask as usual
            newImage("Selection", "8-bit black", w, h, 1);
            tempID=getImageID();
            setPixel(x,y,255);
            selectImage(imageID2);
            run("Duplicate...", " ");
            tempID2=getImageID();
            run("8-bit");
            run("Multiply...", "value=255");
            run("32-bit");
            run("Subtract...", "value=255");
            run("Square");
            run("8-bit");
            run("Fill Holes");
        }
    }
}

```

```

roiManager("reset");
run("Analyze Particles...", "display add");

//close();
selectImage(tempID);
run("Clear Results");
numROIs=roiManager("count");
for (j=0; j<numROIs; j++){
    roiManager("select", j);
    run("Measure");
}
close();
selectImage(tempID2);
run("8-bit");
run("Multiply...", "value=255");
if(numROIs>1){
    MaxVals=Table.getColumn("Max");
    MaxIndex=Array.findMaxima(MaxVals, 1);
    ROIInum=MaxIndex[0];
}else{
    ROIInum=0;
}
roiManager("select", ROIInum);
run("Add...", "value=255");
run("Clear Outside");
makeRectangle(0, 0,w, h);
run("Subtract...", "value=200");
run("Multiply...", "value=8");
roiManager("deselect");
makeRectangle(0, 0,w, h);
run("Erode");
roiManager("reset");
saveAs("Tiff", output3+filename);
selectImage(imageID);
saveAs("Tiff", output1+filename);
run("Close All");
roiManager("reset");
}else if(A==2){
    //If more than once cell, ask user to select the one
that is intended

    roiManager("reset");
    setTool("freehand");
    waitForUser("Cell Selector", "Trace the cell that you
want to keep or divide.");
    roiManager("add");
    selectImage(imageID2);
    roiManager("select", 0);
    run("Clear Outside");
    makeRectangle(0, 0,w, h);
    run("Subtract...", "value=0.9");
    //Then proceed with preparing the mask as usual
    newImage("Selection", "8-bit black", w, h, 1);
    tempID=getImageID();
    setPixel(x,y,255);
    roiManager("reset");
    selectImage(imageID2);
    makeRectangle(0, 0,w, h);

```

```

run("Duplicate...", " ");
tempID2=getImageID();
run("8-bit");
//waitForUser;
run("Multiply...", "value=255");
run("32-bit");
run("Subtract...", "value=255");
run("Square");
run("8-bit");
run("Fill Holes");
//waitForUser;
roiManager("reset");
run("Analyze Particles...", "display add");
//waitForUser;
close();
selectImage(tempID);
run("Clear Results");
numROIs=roiManager("count");
for (j=0; j<numROIs; j++){
    roiManager("select", j);
    run("Measure");
}
close();
selectImage(imageID2);
run("8-bit");
run("Multiply...", "value=255");
if(numROIs>1){
    MaxVals=Table.getColumn("Max");
    MaxIndex=Array.findMaxima(MaxVals, 1);
    ROIInum=MaxIndex[0];
}else{
    ROIInum=0;
}
roiManager("select", ROIInum);
run("Add...", "value=255");
run("Clear Outside");
makeRectangle(0, 0,w, h);
run("Subtract...", "value=200");
run("Multiply...", "value=8");

roiManager("deselect");
makeRectangle(0, 0,w, h);

run("Erode");
roiManager("reset");
saveAs("Tiff", output3+filename);
selectImage(imageID);
saveAs("Tiff", output1+filename);
run("Close All");
roiManager("reset");
}else {
    selectImage(imageID);
    saveAs("Tiff", output2+filename);
run("Close All");
}
}

```

### 6.2.1.8 *MaskApply3\_1Channel.ijm*

```
//mask = getDirectory("Choose Dilated Mask Directory: ");
input = getDirectory("Choose Target Directory (should contain a CellImages
folder): ");
parent = File.getParent(input);
target = input + "CellImages\\";
mask = parent + "\\DilatedMasks_BlackEdge\\";
output = input + "CellMasked\\";
list = getFileList(mask);
File.makeDirectory(output);
setBatchMode(true);
for (i = 0; i < list.length; i++) {
    filename=list[i];
    Matt4(target, filename);
}
//setBatchMode(false);
function Matt4(target, filename) {
    L=lengthOf(filename);
    filebase=substring(filename,0,L-4);
    open(target+filename);
    c2=getImageID();
    open(mask+filename);
    run("Divide...", "value=255");
    c1=getImageID();
    imageCalculator("Multiply create", c2, c1);
    //selectImage(c2);
    //waitForUser("");
    saveAs("Tiff", output+filename);
    run("Close All");
    run("Clear Results");
}
}
```

### 6.2.1.9 *MaskApply3\_2Channel.ijm*

```
//mask = getDirectory("Choose Dilated Mask Directory: ");
input = getDirectory("Choose Target Directory (should contain a CellImages
folder): ");
parent = File.getParent(input);
target = input + "CellImages\\";
mask = parent + "\\DilatedMasks_BlackEdge\\";
output = input + "CellMasked\\";
list = getFileList(mask);
File.makeDirectory(output);
setBatchMode(true);
for (i = 0; i < list.length; i++) {
    filename=list[i];
    Matt4(target, filename);
}
//setBatchMode(false);
function Matt4(target, filename) {
    L=lengthOf(filename);
    filebase=substring(filename,0,L-4);
    open(target+filename);
    run("Split Channels");
}
```

```

selectImage(1);
c2=getTitle();
selectImage(2);
c3=getTitle();
//selectImage(3);
//c4=getTitle();
//selectImage(4);
//c5=getTitle();
open(mask+filename);
    run("Divide...", "value=255");
    c1=getTitle();
imageCalculator("Multiply", c2, c1);
imageCalculator("Multiply", c3, c1);
//imageCalculator("Multiply", c4, c1);
//imageCalculator("Multiply", c5, c1);
run("Merge Channels...", "c1="+c2+" c2="+c3+" create");
saveAs("Tiff", output+filename);

run("Close All");
run("Clear Results");
roiManager("Reset");
}

```

### **6.2.1.10 analyze\_mito\_masks\_for\_Matlab.ijm**

```

input = getDirectory("Choose cell-masked mito object predictions: ");
output1 = input + "MitoMask_tifs\\";
output1a = input + "MitoMask_rois\\";
output1b = input + "MitoMask_results\\";
fileList = getFileList(input);
File.makeDirectory(output1);
File.makeDirectory(output1a);
File.makeDirectory(output1b);
setBatchMode(true);
for (i = 0; i < fileList.length; i++) {
    filename=fileList[i];
    Matt1(input, filename);
}
function Matt1(input, filename) {
    open(input+filename);
    L=lengthOf(filename);
    filebase=substring(filename,0,L-4);
    run("Set Measurements...", "area mean min centroid center fit
integrated redirect=None decimal=3");
//Isolate the mitos, then save image to a separate file
parentID = getImageID();
run("Duplicate...", "duplicate");
run("Multiply...", "value=10");
setThreshold(8, 32);
run("Convert to Mask");
tubularID = getImageID();
saveAs("Tiff", output1+filebase+".tif");
//Save ROIs and analyze particles results table
selectImage(tubularID);

```

```

run("Analyze Particles...", "display exclude add");
if (roiManager("count") > 0){
    roiManager("Save", output1a + filebase + ".zip");
    roiManager("Reset");
    selectWindow("Results");
    saveAs("Results", output1b + filebase + ".csv");
}
run("Clear Results");
run("Close All");
run("Clear Results");
roiManager("Reset");
}

```

## 6.2.2 Lipid droplet microscopy analysis

### 6.2.2.1 *Threshold\_8bit\_Prob\_CellMask\_BODIPY\_v3.ijm*

```

input = getDirectory("Choose Experiment Directory: ");
masks = input + "cellMask_raw_TIFs_v2\\";
output = input + "cellMask_thresholded_v2\\";
fileList = getFileList(masks);
File.makeDirectory(output);
setBatchMode(true);
for (i = 0; i < fileList.length; i++) {
    filename=fileList[i];
    Matt1(masks, filename);
}
function Matt1(masks, filename) {
    open(masks+filename);
    L=lengthOf(filename);
    filebase=substring(filename,0,L-4);
    //run("Invert LUT");
    setAutoThreshold("Default dark");
    run("Create Mask");
    originalMask = getImageID();
    run("Duplicate...", " ");
    smallMask = getImageID();
    //run("Analyze Particles...", "size=50000-Infinity add");
    run("Analyze Particles...", "size=0-50000 add");
    //setForegroundColor(0,0,0);
    roiManager("Fill");
    run("Fill Holes");
    run("Invert LUT");
    //imageCalculator("Subtract create", originalMask, smallMask);
    //setForegroundColor(255,255,255);
    saveAs("Tiff", output+filebase+".tif");
    roiManager("Reset");
    run("Close All");
    run("Clear Results");
}

```

### 6.2.2.2 *Matt\_CellMask\_GUI\_LD\_v3.ijm*

```

exp_dir = getDirectory("Choose Experiment directory");

```

```

//input = exp_dir + "all_files_8bit_C1_saturated_for_CellMasking/";
input = exp_dir;
masks_dir = exp_dir + "cellMasks_for_GUI/";
output1 = exp_dir + "CellMaskGUI_correct_images/";
output2 = exp_dir + "CellMaskGUI_masks_preliminary/";
output3 = exp_dir + "CellMaskGUI_rejected_no_ROIs_traced_no_mask_found/";
output4 = exp_dir + "CellMaskGUI_rejected_bad_images/";
list = getFileList(masks_dir);
File.makeDirectory(output1);
File.makeDirectory(output2);
File.makeDirectory(output3);
File.makeDirectory(output4);
for (i = 0; i < list.length; i++) {
    filename=list[i];
    if (indexOf(filename, ".tif")>=0) {
        Matt4(input, filename);
    }
}
function Matt4(input, filename){
    L = lengthOf(filename);
    filebase=substring(filename,0,L-4);
    //orgIG is the original 8bit BODIPY image
    open(input+filename);
    orgID = getImageID();
    w = getWidth();
    h = getHeight();
    open(masks_dir+filename);
    maskID = getImageID();
    run("Duplicate...", "duplicate");
    maskTempID = getImageID();
    maskTempTitle = getTitle();
    selectImage(orgID);
    run("Duplicate...", "duplicate");
    orgTempID = getImageID();
    orgTempTitle = getTitle();
    run("Combine...", "stack1=" + orgTempTitle + " stack2=" +
maskTempTitle);
    combinedID = getImageID();
    combinedTitle = getTitle();
    makePoint(w/2, h/2);
    run("Add Selection...");
    makePoint(w/2+w, h/2);
    run("Add Selection...");
    setLocation(400,400);
    //NOTE: use doWand(x,y) at the center point of the image, then
roiManager("Add") to select the central(default) ROI/mask
    A=getNumber("Choose an option: 1 - keep single cell (the cell in
the middle, or only 1 cell in image) || 2 - Trace/split multiple cells
|| 3 - Reject: ", 1);
    //use doWand on the center point of the image to find the ROI.
Save only that mask, and apply it to the bodipy image and save
    if(A==1){
        roiManager("reset");
    }
}

```

```

selectImage(maskID);
centerPix=getPixel(w/2,h/2);
if(centerPix !=0){
selectImage(maskID);
doWand(w/2, h/2, 1, "8-connected");
roiManager("add");
run("Clear Outside");
run("Select None");
saveAs("tiff", output2 + filename);
selectImage(orgID);
saveAs("tiff", output1+ filename);
}
else {
    selectImage(maskID);
    saveAs("tiff", output2 + filename);
}
}
else if(A==2){
roiManager("reset");
setTool("freehand");
waitForUser("Cell Selector", "Trace the cell(s) that you
want to keep or divide. To keep an ROI, press [t].");
numROIs=roiManager("count");
if(numROIs==0){
    waitForUser("Cell Selector", "When you trace a cell,
don't forget to press [t].");
}
if (numROIs!=0){
for (j=0; j<numROIs; j++){
    selectImage(maskID);
    run("Select None");
    run("Duplicate...", "duplicate");
    mask_A2_tempID = getImageID();

    roiManager("select", j);
    run("Clear Outside");
    run("Select None");
    saveAs("tiff", output2+filebase + "_" +
toString(j)+".tif");
    run("Close");
    selectImage(orgID);
    saveAs("tiff", output1+filebase + "_" +
toString(j)+".tif");
}
}
else{
    selectImage(orgID);
    saveAs("tiff", output3 + filename);
}
}
else{
selectImage(orgID);

```



```

        saveAs("tiff", output4+filename);
    }
    run("Close All");
    run("Clear Results");
    roiManager("reset");
}

```

### 6.2.2.3 *process\_preliminary\_masks\_v2.ijm*

```

exp_dir = getDirectory("Choose Experiment directory");
prelim_masks = exp_dir + "CellMaskGUI_masks_preliminary_BlackEdge/";
list = getFileList(prelim_masks);
output1 = exp_dir + "CellMaskGUI_masks_finalized/";
File.makeDirectory(output1);
setBatchMode(true);
for (i = 0; i < list.length; i++) {
    filename=list[i];
    if (indexOf(filename, ".tif")>=0) {
        Matt4(prelim_masks, filename);
    }
}
function Matt4(prelim_masks, filename){
    open(prelim_masks + filename);
    run("Invert LUT");
    maskID = getImageID();
    w = getWidth();
    h=getHeight();
    run("Remove Overlay");
    run("Select None");
    roiManager("reset");
    run("Analyze Particles...", "display add");
    if (roiManager("count")>1){
        Area=newArray(roiManager("count"));
        for (j=0; j<roiManager("count");j++){
            roiManager("select", j);
            getStatistics(Area[j], mean, min, max, std, histogram);
        }
        AreaLarge = 0;
        for (j=0; j<(roiManager("count"));j++){
            if (Area[j]>AreaLarge){
                AreaLarge=Area[j];
                large = j;
            }
        }
        roiManager("select", large);
        run("Clear Outside");
        roiManager("select", large);
        roiManager("fill");
        saveAs("tiff", output1+filename);
    }
    else{
        open(prelim_masks + filename);
        saveAs("tiff", output1+filename);
    }
    run("Close All");
}

```

```

        run("Clear Results");
        roiManager("reset");
    }

```

#### 6.2.2.4 *convert\_ilastik\_8bit\_to\_LD\_mask.ijm*

```

input = getDirectory("Choose directory with Ilastik segmentation outputs
(TIFs): ");
dirName = File.getName(input);
parent = File.getParent(input);
output = parent + "\\\" + dirName + "_LD-Masks\\"";
list = getFileList(input);
File.makeDirectory(output);
setBatchMode(true);
for (i = 0; i < list.length; i++) {
    filename=list[i];
    if (indexOf(filename, ".tif")>=0) {
        Matt4(input, filename);
    }
}
function Matt4(input, filename) {
    roiManager("reset");
    open(input+filename);
    parentID = getImageID();
    run("Multiply...", "value=10");
    setThreshold(8, 12);
    run("Convert to Mask");
    run("Analyze Particles...", "size=0-30 add");
    setForegroundColor(0,0,0);
    roiManager("Fill");
    setForegroundColor(255,255,255);
    run("Remove Overlay");
    saveAs("Tiff", output+filename);
    run("Close All");
    run("Clear Results");
    roiManager("reset");
}

```

#### 6.2.2.5 *MaskApply3\_1Channel\_LDs\_all.ijm*

```

target = getDirectory("Choose directory that contains the images to be cell-
masked (e.g. LD masks, raw images): ");
dirName = File.getName(target);
parent = File.getParent(target);
parent2 = File.getParent(parent);
//changed this from "parent2" to "parent" for processing nuclear masks
//changed this from "parent" to "parent2" for processing LD masks
mask = parent2 + "\\CellMaskGUI_masks_finalized\\"";
output = parent + "\\\" + dirName + "_CellMasked\\"";
//changed this from "mask" to "target" for processing nuclear masks
//changed this from "target" to "mask" for processing LD masks
list = getFileList(mask);
File.makeDirectory(output);
setBatchMode(true);
for (i = 0; i < list.length; i++) {

```

```

        filename=list[i];
        if (indexOf(filename, ".tif")>=0) {
            Matt4(target, filename);
        }
    }
function Matt4(target, filename) {
    L=lengthOf(filename);
    outInd = indexOf(filename, "Out");
    filebase=substring(filename,0,outInd+3);
    open(target+filebase + ".tif");
    c2=getImageID();
    open(mask+filename);
    run("Divide...", "value=255");
    c1=getImageID();
    imageCalculator("Multiply create", c2, c1);
    saveAs("Tiff", output+filename);
    run("Close All");
    run("Clear Results");
    roiManager("reset");
}

```

### 6.2.2.6 *analyze\_LD\_masks\_for\_Matlab.ijm*

```

input = getDirectory("Choose LD object predictions: ");
parent = File.getParent(input);
output1 = parent + "\\FinalOutput_LD_tifs\\";
output2 = parent + "\\FinalOutput_LD_rois\\";
output3 = parent + "\\FinalOutput_LD_results\\";
File.makeDirectory(output1);
File.makeDirectory(output2);
File.makeDirectory(output3);
fileList = getFileList(input);
setBatchMode(true);
for (i = 0; i < fileList.length; i++) {
    filename=fileList[i];
    if (indexOf(filename, ".tif")>=0) {
        Matt1(input, filename);
    }
}
function Matt1(input, filename) {
    open(input+filename);
    L=lengthOf(filename);
    filebase=substring(filename,0,L-4);
    saveAs("tiff", output1 + filename);
    run("Set Measurements...", "area mean min centroid center fit
integrated redirect=None decimal=3");
    run("Analyze Particles...", "display exlude add");
    if (roiManager("count") > 0){
        roiManager("Save", output2 + filebase + ".zip");
        roiManager("Reset");
        selectWindow("Results");
        saveAs("Results", output3 + filebase + ".csv");
    }
    run("Close All");
    run("Clear Results");
    roiManager("Reset");
}

```

```
}
```

### 6.2.2.7 CellAreas\_LD\_v1.ijm

```
dir1 = getDirectory("Choose Cell Mask Directory: ");
parent = File.getParent(dir1);
list = getFileList(dir1);
setBatchMode(true);
for (i = 0; i < list.length; i++) {
    filename=list[i];
    Matt5(dir1, filename);
    setResult("Label", i, filename);
}
saveAs("Results", parent+"\\CellAreas.txt");
function Matt5(dir1, filename) {
    open(dir1+filename);
    run("Divide...", "value=255");
    run("Measure");
    close();
}
```

## 6.2.3 Bead uptake analysis

### 6.2.3.1 MattCellSplitter2.ijm

```
input = getDirectory("Choose Source Directory: ");
list = getFileList(input+"Tifs/");
File.makeDirectory(input+"Results/");
File.makeDirectory(input+"CellImages/");
setBatchMode(true);
for (i = 0; i < list.length; i++) {
    filename=list[i];
    MattCellMask(input, filename);
}
function MattCellMask(input, filename){
    //Define the file naming scheme:
    L=lengthOf(filename);
    filebase=substring(filename,0,L-4);
    // Open the image
    run("Bio-Formats", "open=" + input +"Tifs/"+ filename + "
autoscale color_mode=Default view=Hyperstack stack_order=XYZCT");
    imageID=getTitle();
    h=getHeight();
    w=getWidth();
    roiManager("reset");
    roiManager("open", input+"ROIs/"+filebase+"_cells.roi");
    roiManager("measure");
    Roi.getCoordinates(x,y);
    for (j=0; j<nResults; j++){
        imagelabel="_Data";
        makeRectangle(x[j]-338,y[j]-338,676,676);
        roiManager("Add");
        roiManager("Select", 1);
    }
}
```

```

        run("Duplicate...", "duplicate");
        if (x[j]-338<=0){
            imagelabel=imagelabel+"_L";
        }
        if (y[j]-338<=0){
            imagelabel=imagelabel+"_T";
        }
        if (x[j]+338>=w){
            imagelabel=imagelabel+"_R";
        }
        if (y[j]+338>=h){
            imagelabel=imagelabel+"_B";
        }
        saveAs("Tiff",input+"CellImages/"+filebase+"_"+toString(j)+imagelabel+"
.tif");
        close();
        roiManager("select", 1);
        roiManager("delete");
    }
    selectWindow("Results");
    saveAs("text",input+"Results/"+filebase+"_results.txt");
    run("Close All");
    run("Clear Results");
}

```

### 6.2.3.2 *PrepForNetworkLocal2.ijm*

```

dir1 = getDirectory("Choose Source Directory: ");
input = dir1 + "CellImages\\";
output = dir1 + "PMforSegmenter16000\\";
list = getFileList(input);
File.makeDirectory(output);
setBatchMode(true);

for (i = 0; i < list.length; i++) {
    filename=list[i];
    Matt1(input, filename);
}

function Matt1(input, filename) {
    open(input+filename);
    L=lengthOf(filename);
    filebase=substring(filename,0,L-4);
    run("Split Channels");
    selectImage(1);
    c1=getTitle();
    selectImage(2);
    c2=getTitle();
    selectImage(3);
    c3=getTitle();
    selectImage(4);
    c4=getTitle();
    //run("Merge Channels...", "c3="+c1+" c5="+c2+" c6="+c3+"
c7="+c4+" create keep ignore");
    //saveAs("Tiff", input+filebase+".tif");
    selectImage(4);
}

```

```

        setMinAndMax(0, 16000);
        //run("Enhance Contrast", "saturated=0.35");
        run("Yellow");
        run("8-bit");
        saveAs("Tiff", output+filebase+"_PM.tif");
        run("Close All");
    }

```

### 6.2.3.3 *MattCellAnalyzerGUI4\_updated.ijm*

```

dir1 = getDirectory("Choose Source Directory: ");
input = dir1 + "PMforSegmenter_unsat\\";
mask = dir1 + "Object_Predictions_unsat\\";
output1 = dir1 + "Correct_unsat\\";
output2 = dir1 + "Incorrect_unsat\\";
output3 = dir1 + "DilatedMasks\\";
list = getFileList(input);
File.makeDirectory(output1);
File.makeDirectory(output2);
File.makeDirectory(output3);

for (i = 0; i < list.length; i++) {
    filename=list[i];
    MattGUI4(input, filename);
}

function MattGUI4(input, filename){
    L=lengthOf(filename);
    filebase=substring(filename,0,L-4);
    open(input+filename);
    print(filebase);
    imageID=getImageID();
    //Find the center of the original image and identify if it is in the
    expected place
    h=getHeight();
    w=getWidth();
    x=338;
    y=338;
    if(w!=676){

        left=indexOf(filebase,"_L");
        right=indexOf(filebase,"_R");
        if(left!=-1){
            x=w-338;
        }
    }
    if(h!=676){
        top=indexOf(filebase,"_T");
        bottom=indexOf(filebase,"_B");

        if(top!=-1){
            y=h-338;
        }
    }
    //Prep the image for viewer inspection
    run("Duplicate...", " ");
}

```

```

run("RGB Color");
w1=getTitle();
open(mask+filebase+"_ObjectClass.tif");
imageID2=getImageID();
//Test if the center pixel is in a cell mask
selectImage(imageID2);
Center=getPixel(x,y);
//Continue with visualization
run("Duplicate...", " ");
w2=getTitle();
run("8-bit");
run("RGB Color");
run("Combine...", "stack1="+w1+" stack2="+w2);
setLocation(600,600);
// If the center is not in a mask:
if(Center==0){

    A=getNumber("ALERT ALERT ALERT
Is there a cell here? 1 - no 2 - yes:", 1);
    if(A==1){
        selectImage(imageID);
        saveAs("Tiff", output2+filename);
run("Close All");
//If not, save the image as incorrect so it can be thresholded
}else{
    // If so, correct the misplaced center
run("ROI Manager...");
roiManager("reset");
setTool("multipoint");
waitForUser("Cell Selector", "Put the dot back where it was
supposed to go. If you miss, just make another. Only the last is kept.");
roiManager("add");
roiManager("Select", 0);
Roi.getCoordinates(a,b);
//Check if it is one cell or more than one
B=getNumber("Number of cells in this mask?", 1);
if(B==1){
    //If one cell, proceed with selecting the mask and
saving it

        newImage("Selection", "8-bit black", w, h, 1);
tempID=getImageID();
setPixel(a[0],b[0],255);
selectImage(imageID2);
run("Duplicate...", " ");
tempID2=getImageID();
run("8-bit");
run("Multiply...", "value=255");
run("32-bit");
run("Subtract...", "value=255");
run("Square");
run("8-bit");
run("Fill Holes");
roiManager("reset");
run("Analyze Particles...", "display add");
selectImage(tempID);
run("Clear Results");
numROIs=roiManager("count");

```

```

for (j=0; j<numROIs; j++){
    roiManager("select", j);
    run("Measure");
}
close();
selectImage(imageID2);
run("8-bit");
run("Multiply...", "value=255");
if(numROIs>1){
    MaxVals=Table.getColumn("Max");
    MaxIndex=Array.findMaxima(MaxVals, 1);
    ROIInum=MaxIndex[0];
}else{
    ROIInum=0;
}
roiManager("select", ROIInum);
run("Add...", "value=255");
run("Clear Outside");
makeRectangle(0, 0,w, h);
run("Subtract...", "value=200");
run("Multiply...", "value=8");

roiManager("deselect");
makeRectangle(0, 0,w, h);

run("Erode");
roiManager("reset");
saveAs("Tiff", output3+filebase+"_Mask.tif");
selectImage(imageID);
saveAs("Tiff", output1+filename);
run("Close All");
roiManager("reset");
}else{
    //If more than once cell, ask user to select the one
that is intended
    roiManager("reset");
    setTool("freehand");
    waitForUser("Cell Selector", "Trace the cell that you
want to keep or divide.");
    roiManager("add");
    selectImage(imageID2);
    roiManager("select", 0);
    run("Clear Outside");
    makeRectangle(0, 0,w, h);
    run("Subtract...", "value=1");

    //Then proceed with preparing the mask as usual
newImage("Selection", "8-bit black", w, h, 1);
tempID=getImageID();
setPixel(a[0],b[0],255);
roiManager("reset");
selectImage(imageID2);
makeRectangle(0, 0,w, h);
run("Duplicate...", " ");
tempID2=getImageID();
run("8-bit");
//waitForUser;

```



```

run("Multiply...", "value=255");
run("32-bit");
run("Subtract...", "value=255");
run("Square");
run("8-bit");
run("Fill Holes");
roiManager("reset");
run("Analyze Particles...", "display add");
//waitForUser;
close();
selectImage(tempID);
run("Clear Results");
numROIs=roiManager("count");
for (j=0; j<numROIs; j++){
    roiManager("select", j);
    run("Measure");
}
close();
selectImage(imageID2);
run("8-bit");
run("Multiply...", "value=255");
if(numROIs>1){
    MaxVals=Table.getColumn("Max");
    MaxIndex=Array.findMaxima(MaxVals, 1);
    ROIInum=MaxIndex[0];
}else{
    ROIInum=0;
}
roiManager("select", ROIInum);
run("Add...", "value=255");
run("Clear Outside");
makeRectangle(0, 0, w, h);
run("Subtract...", "value=200");
run("Multiply...", "value=8");
roiManager("deselect");
makeRectangle(0, 0, w, h);
run("Erode");
roiManager("reset");
saveAs("Tiff", output3+filebase+"_Mask.tif");
selectImage(imageID);
saveAs("Tiff", output1+filename);
run("Close All");
roiManager("reset");
}
}

// If the center is in the mask:
if(Center!=0){
A=getNumber("Do you need to split cells? 1 - No 2 - Yes 3 - Discard:",
1);
    if(A==1){
        //Proceed with preparing the mask as usual
        newImage("Selection", "8-bit black", w, h, 1);
        tempID=getImageID();
        setPixel(x, y, 255);
        selectImage(imageID2);

```

```

run("Duplicate...", " ");
tempID2=getImageID();
run("8-bit");
run("Multiply...", "value=255");
run("32-bit");
run("Subtract...", "value=255");
run("Square");
run("8-bit");
run("Fill Holes");

roiManager("reset");
run("Analyze Particles...", "display add");
//close();
selectImage(tempID);
run("Clear Results");
numROIs=roiManager("count");
for (j=0; j<numROIs; j++){
    roiManager("select", j);
    run("Measure");
}
close();
selectImage(tempID2);
run("8-bit");
run("Multiply...", "value=255");
if(numROIs>1){
    MaxVals=Table.getColumn("Max");
    MaxIndex=Array.findMaxima(MaxVals, 1);
    ROIInum=MaxIndex[0];
}else{
    ROIInum=0;
}
roiManager("select", ROIInum);
run("Add...", "value=255");
run("Clear Outside");
makeRectangle(0, 0,w, h);
run("Subtract...", "value=200");
run("Multiply...", "value=8");
roiManager("deselect");
makeRectangle(0, 0,w, h);
run("Erode");
roiManager("reset");
saveAs("Tiff", output3+filebase+"_Mask.tif");
selectImage(imageID);
saveAs("Tiff", output1+filename);
run("Close All");
roiManager("reset");

}else if(A==2){

//If more than once cell, ask user to select the one
that is intended

roiManager("reset");
setTool("freehand");
waitForUser("Cell Selector", "Trace the cell that you
want to keep or divide.");
roiManager("add");
selectImage(imageID2);

```

```

roiManager("select", 0);
run("Clear Outside");
makeRectangle(0, 0,w, h);
run("Subtract...", "value=0.9");
//Then proceed with preparing the mask as usual
newImage("Selection", "8-bit black", w, h, 1);
tempID=getImageID();
setPixel(x,y,255);
roiManager("reset");
selectImage(imageID2);
makeRectangle(0, 0,w, h);
run("Duplicate...", " ");
tempID2=getImageID();
run("8-bit");
//waitForUser;
run("Multiply...", "value=255");
run("32-bit");
run("Subtract...", "value=255");
run("Square");
run("8-bit");
run("Fill Holes");
//waitForUser;
roiManager("reset");
run("Analyze Particles...", "display add");
//waitForUser;
close();
selectImage(tempID);
run("Clear Results");
numROIs=roiManager("count");
for (j=0; j<numROIs; j++){
    roiManager("select", j);
    run("Measure");
}
close();
selectImage(imageID2);
run("8-bit");
run("Multiply...", "value=255");
if(numROIs>1){
    MaxVals=Table.getColumn("Max");
    MaxIndex=Array.findMaxima(MaxVals, 1);
    ROIInum=MaxIndex[0];
}else{
    ROIInum=0;
}
roiManager("select", ROIInum);
run("Add...", "value=255");
run("Clear Outside");
makeRectangle(0, 0,w, h);
run("Subtract...", "value=200");
run("Multiply...", "value=8");

roiManager("deselect");
makeRectangle(0, 0,w, h);

run("Erode");
roiManager("reset");
saveAs("Tiff", output3+filebase+"_Mask.tif");

```

```

        selectImage(imageID);
        saveAs("Tiff", output1+filename);
        run("Close All");
        roiManager("reset");

    }else {
        selectImage(imageID);
        saveAs("Tiff", output2+filename);
        run("Close All");
    }
}
}

```

#### 6.2.3.4 *MaskApply2.ijm*

```

dir1 = getDirectory("Choose Source Directory: ");
output = dir1 + "MaskedData\\";
listn= getFileList(dir1+"DilatedMasks\\");
File.makeDirectory(output);
setBatchMode(true);
for (i = 0; i < list.length; i++) {
    filename=list[i];
    Matt4(dir1, filename);
}
function Matt4(dir1, filename) {
    L=lengthOf(filename);
    filebase=substring(filename,0,L-12);
    open(dir1+"CellImages\\"+filebase+".tif");
    run("Split Channels");
    selectImage(1);
    c2=getTitle();
    selectImage(2);
    c3=getTitle();
    selectImage(3);
    c4=getTitle();
    selectImage(4);
    c5=getTitle();
    open(dir1+"DilatedMasks\\"+filename);
    run("Divide...", "value=255");
    c1=getTitle();
    imageCalculator("Multiply", c2, c1);
    imageCalculator("Multiply", c3, c1);
    imageCalculator("Multiply", c4, c1);
    imageCalculator("Multiply", c5, c1);

    run("Merge Channels...", "c1="+c2+" c2="+c3+" c3="+c4+" c4="+c5+"
create");
    saveAs("Tiff", output+filebase+"_MaskData.tif");
    run("Close All");
}

```

#### 6.2.3.5 *RunTrackmate\_v2\_1um.py*

```

from fiji.plugin.trackmate import Model
from fiji.plugin.trackmate import Settings

```

```

from fiji.plugin.trackmate import TrackMate
from fiji.plugin.trackmate import SelectionModel
from fiji.plugin.trackmate import Logger
from fiji.plugin.trackmate.detection import LogDetectorFactory
from fiji.plugin.trackmate.tracking.sparselap import SparseLAPTrackerFactory
from fiji.plugin.trackmate.tracking import LAPUtils
from ij import IJ
import fiji.plugin.trackmate.visualization.hyperstack.HyperStackDisplayer as
HyperStackDisplayer
import fiji.plugin.trackmate.features.FeatureFilter as FeatureFilter
import sys
import fiji.plugin.trackmate.features.track.TrackDurationAnalyzer as
TrackDurationAnalyzer
import os
from ij import IJ, ImagePlus, ImageStack
import fiji.plugin.trackmate.Settings as Settings
import fiji.plugin.trackmate.Model as Model
import fiji.plugin.trackmate.SelectionModel as SelectionModel
import fiji.plugin.trackmate.TrackMate as TrackMate
import fiji.plugin.trackmate.Logger as Logger
import fiji.plugin.trackmate.detection.DetectorKeys as DetectorKeys
import fiji.plugin.trackmate.detection.DogDetectorFactory as
DogDetectorFactory
import fiji.plugin.trackmate.tracking.sparselap.SparseLAPTrackerFactory as
SparseLAPTrackerFactory
import fiji.plugin.trackmate.tracking.LAPUtils as LAPUtils
import fiji.plugin.trackmate.visualization.hyperstack.HyperStackDisplayer as
HyperStackDisplayer
import fiji.plugin.trackmate.features.FeatureFilter as FeatureFilter
import fiji.plugin.trackmate.features.FeatureAnalyzer as FeatureAnalyzer
import fiji.plugin.trackmate.action.ExportStatsToIJAction as
ExportStatsToIJAction
import fiji.plugin.trackmate.io.TmXmlReader as TmXmlReader
import fiji.plugin.trackmate.action.ExportTracksToXML as ExportTracksToXML
import fiji.plugin.trackmate.io.TmXmlWriter as TmXmlWriter
import fiji.plugin.trackmate.features.ModelFeatureUpdater as
ModelFeatureUpdater
import fiji.plugin.trackmate.features.SpotFeatureCalculator as
SpotFeatureCalculator

import fiji.plugin.trackmate.features.spot.SpotContrastAndSNRAnalyzer as
SpotContrastAndSNRAnalyzer
import fiji.plugin.trackmate.features.spot.SpotContrastAndSNRAnalyzerFactory
as SpotContrastAndSNRAnalyzerFactory
import fiji.plugin.trackmate.features.spot.SpotIntensityAnalyzer as
SpotIntensityAnalyzer
import fiji.plugin.trackmate.features.spot.SpotIntensityAnalyzerFactory as
SpotIntensityAnalyzerFactory
import fiji.plugin.trackmate.features.spot.SpotMorphologyAnalyzer as
SpotMorphologyAnalyzer
import fiji.plugin.trackmate.features.spot.SpotMorphologyAnalyzerFactory as
SpotMorphologyAnalyzerFactory
import fiji.plugin.trackmate.features.spot.SpotRadiusEstimator as
SpotRadiusEstimator
import fiji.plugin.trackmate.features.spot.SpotRadiusEstimatorFactory as
SpotRadiusEstimatorFactory

```

```

import fiji.plugin.trackmate.features.track.TrackSpeedStatisticsAnalyzer as
TrackSpeedStatisticsAnalyzer
import fiji.plugin.trackmate.util.TMUtils as TMUtils
import fiji.plugin.trackmate.action.ExportStatsToIJAction as
ExportStatsToIJAction
import fiji.plugin.trackmate.action.ExportAllSpotsStatsAction as
ExportAllSpotsStatsAction
import ntpath
from ij.gui import WaitForUserDialog
#Get directory
srcDir = IJ.getDirectory('Chose the directory with masked TIF files to be
analyzed')
parentDir = os.path.dirname(srcDir[:-1])
spotStatDir = parentDir + '/Spot_Statistics_lum'
#We want to put the results in a new directory called SpotStatDir in the
parent directory.
#Check whether the directory exists. Create it if not
if not os.path.exists(spotStatDir):
    os.makedirs(spotStatDir)
#iterate through the directory's .tif files
for root, directories, filenames in os.walk(srcDir):
    for filename in filenames:
        if '.tif' in filename:

            #get the full file path, and open it for trackmate to use
late
            fullFile = root+filename
            print fullFile
            imp = IJ.openImage(fullFile)
            filebase=ntpath.basename(filename)[:-4]
            #create the model and set the parameters. I've left in the
tracking stuff from the sample code, even though we don't use it.
            #most important things here are the detector settings,
which can be changed for different experiments/beads
            model = Model()
            model.setLogger(Logger.IJ_LOGGER)
            settings = Settings()
            settings.setFrom(imp)
            settings.detectorFactory = LogDetectorFactory()
            settings.detectorSettings = {
                'DO_SUBPIXEL_LOCALIZATION' : True,
                'RADIUS' : .5,
                'TARGET_CHANNEL' : 2,
                'THRESHOLD' : 500.,
                'DO_MEDIAN_FILTERING' : True,
            }

            #we threshold in the detector settings, so we don't use the
quality filter
            filter1 = FeatureFilter('QUALITY', 0, True)
            settings.addSpotFilter(filter1)
            settings.trackerFactory = SparseLAPTrackerFactory()
            settings.trackerSettings =
LAPUtils.getDefaultLAPSettingsMap()
            settings.trackerSettings['ALLOW_TRACK_SPLITTING'] = True
            settings.trackerSettings['ALLOW_TRACK_MERGING'] = True

```

```

settings.addSpotAnalyzerFactory(SpotIntensityAnalyzerFactory())

settings.addSpotAnalyzerFactory(SpotContrastAndSNRAnalyzerFactory())

settings.addSpotAnalyzerFactory(SpotMorphologyAnalyzerFactory())

settings.addSpotAnalyzerFactory(SpotRadiusEstimatorFactory())
    settings.addTrackAnalyzer(TrackDurationAnalyzer())
    filter2 = FeatureFilter('TRACK_DISPLACEMENT', 10, True)
    settings.addTrackFilter(filter2)

#create the trackmate, check it, and then execute the
processing
trackmate = TrackMate(model, settings)
ok = trackmate.checkInput()
if not ok:
    sys.exit(str(trackmate.getErrorMessage()))
ok = trackmate.process()
if not ok:
    continue
    #sys.exit(str(trackmate.getErrorMessage()))
#ExportAll... uses the selectionModel, so we generate one
and then execute the function. This generates an ImageJ results/table window,
#which we can select and then save as a CSV in the output
directory. Need to close everything before the next loop iteration.
selectionModel = SelectionModel(model)
#show the image for debugging/quality control
#displayer = HyperStackDisplayer(model, selectionModel,
imp)
    #displayer.render()
    #displayer.refresh()
    #myWait = WaitForUserDialog ("myTitle", "myMessage")
    #myWait.show()

ExportAllSpotsStatsAction(selectionModel).execute(trackmate)
    IJ.selectWindow('All Spots statistics')
    IJ.saveAs('Results', spotStatDir + '/' + filebase + '.csv')
    IJ.run('Close')
    IJ.run('Close All')
    IJ.run('Clear Results')

```

### 6.2.3.6 RunTrackmate\_v2\_170nm.py

```

from fiji.plugin.trackmate import Model
from fiji.plugin.trackmate import Settings
from fiji.plugin.trackmate import TrackMate
from fiji.plugin.trackmate import SelectionModel
from fiji.plugin.trackmate import Logger
from fiji.plugin.trackmate.detection import LogDetectorFactory
from fiji.plugin.trackmate.tracking.sparselap import SparseLAPTrackerFactory
from fiji.plugin.trackmate.tracking import LAPUtils
from ij import IJ
import fiji.plugin.trackmate.visualization.hyperstack.HyperStackDisplayer as
HyperStackDisplayer
import fiji.plugin.trackmate.features.FeatureFilter as FeatureFilter

```

```

import sys
import fiji.plugin.trackmate.features.track.TrackDurationAnalyzer as
TrackDurationAnalyzer
import os
from ij import IJ, ImagePlus, ImageStack
import fiji.plugin.trackmate.Settings as Settings
import fiji.plugin.trackmate.Model as Model
import fiji.plugin.trackmate.SelectionModel as SelectionModel
import fiji.plugin.trackmate.TrackMate as TrackMate
import fiji.plugin.trackmate.Logger as Logger
import fiji.plugin.trackmate.detection.DetectorKeys as DetectorKeys
import fiji.plugin.trackmate.detection.DogDetectorFactory as
DogDetectorFactory
import fiji.plugin.trackmate.tracking.sparselap.SparseLAPTrackerFactory as
SparseLAPTrackerFactory
import fiji.plugin.trackmate.tracking.LAPUtils as LAPUtils
import fiji.plugin.trackmate.visualization.hyperstack.HyperStackDisplayer as
HyperStackDisplayer
import fiji.plugin.trackmate.features.FeatureFilter as FeatureFilter
import fiji.plugin.trackmate.features.FeatureAnalyzer as FeatureAnalyzer
import fiji.plugin.trackmate.action.ExportStatsToIJAction as
ExportStatsToIJAction
import fiji.plugin.trackmate.io.TmXmlReader as TmXmlReader
import fiji.plugin.trackmate.action.ExportTracksToXML as ExportTracksToXML
import fiji.plugin.trackmate.io.TmXmlWriter as TmXmlWriter
import fiji.plugin.trackmate.features.ModelFeatureUpdater as
ModelFeatureUpdater
import fiji.plugin.trackmate.features.SpotFeatureCalculator as
SpotFeatureCalculator
import fiji.plugin.trackmate.features.spot.SpotContrastAndSNRAnalyzer as
SpotContrastAndSNRAnalyzer
import fiji.plugin.trackmate.features.spot.SpotContrastAndSNRAnalyzerFactory
as SpotContrastAndSNRAnalyzerFactory
import fiji.plugin.trackmate.features.spot.SpotIntensityAnalyzer as
SpotIntensityAnalyzer
import fiji.plugin.trackmate.features.spot.SpotIntensityAnalyzerFactory as
SpotIntensityAnalyzerFactory
import fiji.plugin.trackmate.features.spot.SpotMorphologyAnalyzer as
SpotMorphologyAnalyzer
import fiji.plugin.trackmate.features.spot.SpotMorphologyAnalyzerFactory as
SpotMorphologyAnalyzerFactory
import fiji.plugin.trackmate.features.spot.SpotRadiusEstimator as
SpotRadiusEstimator
import fiji.plugin.trackmate.features.spot.SpotRadiusEstimatorFactory as
SpotRadiusEstimatorFactory

import fiji.plugin.trackmate.features.track.TrackSpeedStatisticsAnalyzer as
TrackSpeedStatisticsAnalyzer
import fiji.plugin.trackmate.util.TMUtils as TMUtils
import fiji.plugin.trackmate.action.ExportStatsToIJAction as
ExportStatsToIJAction
import fiji.plugin.trackmate.action.ExportAllSpotsStatsAction as
ExportAllSpotsStatsAction
import ntpath
#Get directory
srcDir = IJ.getDirectory('Chose the directory with masked TIF files to be
analyzed')

```



```

parentDir = os.path.dirname(srcDir[:-1])
spotStatDir = parentDir + '/Spot_Statistics_170nm'
#We want to put the results in a new directory called SpotStatDir in the
parent directory.
#Check whether the directory exists. Create it if not
if not os.path.exists(spotStatDir):
    os.makedirs(spotStatDir)
#iterate through the directory's .tif files
for root, directories, filenames in os.walk(srcDir):
    for filename in filenames:
        if '.tif' in filename:
            #get the full file path, and open it for trackmate to use
late
            fullFile = root+filename
            #print fullFile
            imp = IJ.openImage(fullFile)
            filebase=ntpath.basename(filename)[:-4]
            #create thenmodel and set the parameters. I've left in the
tracking stuff from the sample code, even though we don't use it.
            #most important things here are the detector settings,
which can be changed for different experiments/beads
            model = Model()
            model.setLogger(Logger.IJ_LOGGER)
            settings = Settings()
            settings.setFrom(imp)
            settings.detectorFactory = LogDetectorFactory()
            settings.detectorSettings = {
                'DO_SUBPIXEL_LOCALIZATION' : True,
                'RADIUS' : .25,
                'TARGET_CHANNEL' : 3,
                'THRESHOLD' : 125.,
                'DO_MEDIAN_FILTERING' : True,
            }
            #we threshold in the detector settings, so we don't use the
quality filter
            filter1 = FeatureFilter('QUALITY', 0, True)
            settings.addSpotFilter(filter1)
            settings.trackerFactory = SparseLAPTrackerFactory()
            settings.trackerSettings =
LAPUtils.getDefaultLAPSettingsMap()
            settings.trackerSettings['ALLOW_TRACK_SPLITTING'] = True
            settings.trackerSettings['ALLOW_TRACK_MERGING'] = True

            settings.addSpotAnalyzerFactory(SpotIntensityAnalyzerFactory())

            settings.addSpotAnalyzerFactory(SpotContrastAndSNRAnalyzerFactory())

            settings.addSpotAnalyzerFactory(SpotMorphologyAnalyzerFactory())

            settings.addSpotAnalyzerFactory(SpotRadiusEstimatorFactory())
            settings.addTrackAnalyzer(TrackDurationAnalyzer())
            filter2 = FeatureFilter('TRACK_DISPLACEMENT', 10, True)
            settings.addTrackFilter(filter2)

            #create the trackmate, check it, and then execute the
processing
            trackmate = TrackMate(model, settings)

```

```

        ok = trackmate.checkInput()
        if not ok:
            sys.exit(str(trackmate.getErrorMessage()))
        ok = trackmate.process()
        if not ok:
            sys.exit(str(trackmate.getErrorMessage()))

        #ExportAll... uses the selectionModel, so we generate one
and then execute the function. This generates an ImageJ results/table window,
        #which we can select and then save as a CSV in the output
directory. Need to close everything before the next loop iteration.
        selectionModel = SelectionModel(model)

        ExportAllSpotsStatsAction(selectionModel).execute(trackmate)
        IJ.selectWindow('All Spots statistics')
        IJ.saveAs('Results', spotStatDir + '/' + filebase + '.csv')
        IJ.run('Close')
        IJ.run('Close All')
        IJ.run('Clear Results')

```

### 6.2.3.7 *CellAreas.ijm*

```

dir1 = getDirectory("Choose Source Directory: ");
list = getFileList(dir1+"DilatedMasks\\");
setBatchMode(true);
for (i = 0; i < list.length; i++) {
    filename=list[i];
    Matt5(dir1, filename);
    setResult("Label", i, filename);
}
saveAs("Results", dir1+"CellAreas.txt");
function Matt5(dir1, filename) {
    open(dir1+"DilatedMasks\\"+filename);
    run("Divide...", "value=255");
    run("Measure");
    close();
}

```

### 6.2.3.8 *isolate\_and\_analyze\_live\_nuclear\_masks.ijm*

```

input = getDirectory("Choose directory containing nuclear object predictions:
");
dirName = File.getName(input);
parent = File.getParent(input);
parent2 = File.getParent(parent);
output = parent + "\\\" + dirName + "_live_nuclei_masks\\";
output2 = parent2 + "\\cellMasked_nuclear_results\\";
output3 = parent2 + "\\cellMasked_nuclear_rois\\";
fileList = getFileList(input);
File.makeDirectory(output);
File.makeDirectory(output2);
File.makeDirectory(output3);

setBatchMode(true);
for (i = 0; i < fileList.length; i++) {

```

```

        filename=fileList[i];
        if (indexOf(filename, ".tif")>=0) {
            Matt1(input, filename);
        }
    }

function Matt1(input, filename) {
    L=lengthOf(filename);
    filebase=substring(filename,0,L-4);
    filebase = filebase + "_MaskData";
    open(input + filename);
    run("Multiply...", "value=10");
    setThreshold(5, 14);
    run("Convert to Mask");
    saveAs("tiff", output + filebase + ".tif");
    run("Analyze Particles...", "display add");
    if (roiManager("count") > 0){
        roiManager("Save", output3 + filebase + ".zip");
        roiManager("Reset");
        selectWindow("Results");
        saveAs("Results", output2 + filebase + ".csv");
    }
    run("Close All");
    run("Clear Results");
    roiManager("reset");
}

```

## 6.2.4 Endosome maturation microscopy

### 6.2.4.1 *process\_nuclear\_mask\_v4\_endo.ijm*

```

input = getDirectory("Choose experiment folder: ");
obj_pred = input + "Object_Predictions_nuclear\\";
output = input + "Object_Predictions_nuclear_masks\\";
output_ROI = input + "Live_ROI_points\\";
output_nuclear_ROI = input + "Live_ROI_full_nucleus\\"
fileList = getFileList(obj_pred);
File.makeDirectory(output);
File.makeDirectory(output_ROI);
File.makeDirectory(output_nuclear_ROI);
setBatchMode(true);
for (i = 0; i < fileList.length; i++) {
    filename=fileList[i];
    Matt1(input, filename);
}
function Matt1(input, filename) {
    open(obj_pred+filename);
    L=lengthOf(filename);
    filebase=substring(filename,0,L-4);
    imageID = getTitle();
    //multiply by 10 to get better dynamic range, and then threshold around 10
    (value of live was 1 before x10)
    run("Multiply...", "value=10");
}

```

```

setThreshold(5, 14);
setOption("BlackBackground", true);
run("Convert to Mask");
run("Fill Holes");
live_only = getImageID();
saveAs("Tiff", output+filebase+".tif");
run("Analyze Particles...", "display add");
roiManager("Save", output_nuclear_ROI + filebase + ".zip");
roiManager("Delete");
roiManager("Reset");
numberOfPoints = getValue("results.count");
XM = newArray(numberOfPoints);
YM = newArray(numberOfPoints);
    for (i=0; i<numberOfPoints; i++) {
        XM[i] = getResult("XM", i);
        YM[i] = getResult("YM", i);
    }
makeSelection("point", XM, YM);
roiManager("Add");
roiManager("Save", output_ROI + filebase + ".roi");
roiManager("Delete");
roiManager("Reset");
run("Close All");
run("Clear Results");
}

```

#### **6.2.4.2 Threshold\_8bit\_Prob\_CellMaskTMR\_v2.ijm**

```

input = getDirectory("Choose Experiment Directory: ");
output = input + "cellMask_thresholded\\";
masks = input + "cellMask_raw_TIFs\\";
fileList = getFileList(masks);
File.makeDirectory(output);
for (i = 0; i < fileList.length; i++) {
    filename=fileList[i];
    Matt1(masks, filename);
}
function Matt1(masks, filename) {
    open(masks+filename);
    L=lengthOf(filename);
    filebase=substring(filename,0,L-4);
    setAutoThreshold("Default dark");
    run("Create Mask");
    originalMask = getImageID();
    run("Duplicate...", " ");
    smallMask = getImageID();
    run("Analyze Particles...", "size=4000-Infinity add");
    setForegroundColor(0,0,0);
    roiManager("Fill");
    imageCalculator("Subtract create", originalMask, smallMask);
    setForegroundColor(255,255,255);
    saveAs("Tiff", output+filebase+".tif");
    roiManager("Delete");
    roiManager("Reset");
    run("Close All");
}

```

```
}
```

### 6.2.4.3 *MattCellAnalyzerGUI6\_endo\_8bit.ijm*

```
dir1 = getDirectory("Choose Source Directory: ");
input = dir1 + "all_files_8bit_C1+C2_sat\\CellImages\\";
mask = dir1 + "cellMask_thresholded\\CellImages\\";
output1 = dir1 + "Correct\\";
output2 = dir1 + "Incorrect\\";
output3 = dir1 + "DilatedMasks\\";
output4 = dir1 + "Incorrect_no_mask\\";
output5 = dir1 + "Incorrect_overlapping_masks\\";
list = getFileList(input);
File.makeDirectory(output1);
File.makeDirectory(output2);
File.makeDirectory(output3);
File.makeDirectory(output4);
File.makeDirectory(output5);
for (i = 0; i < list.length; i++) {
    filename=list[i];
    MattGUI4(input, filename);
}
function MattGUI4(input, filename){
    L=lengthOf(filename);
    filebase=substring(filename,0,L-4);
    open(input+filename);
    iStr = ""+ i;
    lenStr = "" + list.length;
    currCt = iStr + " of " + lenStr;
    print(filebase + " " + currCt);
    imageID=getImageID();
    //Find the center of the original image and identify if it is in the
    expected place
    h=getHeight();
    w=getWidth();
    x=338;
    y=338;
    if(w!=676){
        left=indexOf(filebase,"_L");
        right=indexOf(filebase,"_R");

        if(left!=-1){
            x=w-338;
        }
    }
    if(h!=676){
        top=indexOf(filebase,"_T");
        bottom=indexOf(filebase,"_B");

        if(top!=-1){
            y=h-338;
        }
    }
    //Prep the image for viewer inspection
    run("Duplicate...", " ");
    run("RGB Color");
}
```

```

w1=getTitle();
open(mask+filename);
imageID2=getImageID();
//Test if the center pixel is in a cell mask
selectImage(imageID2);
Center=getPixel(x,y);
//Continue with visualization
run("Duplicate...", " ");
w2=getTitle();
run("8-bit");
run("RGB Color");
run("Combine...", "stack1="+w1+" stack2="+w2);
makePoint(x, y);
run("Add Selection...");
makePoint(w+x, y);
run("Add Selection...");
setLocation(400,400);
setLocation(600,600);
// If the center is not in a mask:
if(Center==0){
    selectImage(imageID);
    saveAs("Tiff", output4+filename);
    run("Close All");
}
// If the center is in the mask:
if(Center!=0){
    A=getNumber("Do you need to split cells? 1 - No || 2 - Yes || 3 -
Discard || 4 - Overlapping Masks || :", 1);
    if(A==1){
        //Proceed with preparing the mask as usual
        newImage("Selection", "8-bit black", w, h, 1);
        tempID=getImageID();
        setPixel(x,y,255);
        selectImage(imageID2);
        run("Duplicate...", " ");
        tempID2=getImageID();
        run("8-bit");
        run("Multiply...", "value=255");
        run("32-bit");
        run("Subtract...", "value=255");
        run("Square");
        run("8-bit");
        run("Fill Holes");
        roiManager("reset");
        run("Analyze Particles...", "display add");
        //close();
        selectImage(tempID);
        run("Clear Results");
        numROIs=roiManager("count");
        for (j=0; j<numROIs; j++){
            roiManager("select", j);
            run("Measure");
        }
        close();
        selectImage(tempID2);
        run("8-bit");
        run("Multiply...", "value=255");
    }
}

```

```

if(numROIs>1){
    MaxVals=Table.getColumn("Max");
    MaxIndex=Array.findMaxima(MaxVals, 1);
    ROIInum=MaxIndex[0];
}else{
    ROIInum=0;
}
roiManager("select", ROIInum);
run("Add...", "value=255");
run("Clear Outside");
makeRectangle(0, 0,w, h);
run("Subtract...", "value=200");
run("Multiply...", "value=8");
roiManager("deselect");
makeRectangle(0, 0,w, h);
run("Erode");
roiManager("reset");
saveAs("Tiff", output3+filebase+"_Mask.tif");
selectImage(imageID);
saveAs("Tiff", output1+filename);
run("Close All");
roiManager("reset");
}else if(A==2){
    //If more than once cell, ask user to select the one
that is intended

    roiManager("reset");
    setTool("freehand");
    waitForUser("Cell Selector", "Trace the cell that you
want to keep or divide.");
    roiManager("add");
    selectImage(imageID2);
    roiManager("select", 0);
    run("Clear Outside");
    makeRectangle(0, 0,w, h);
    run("Subtract...", "value=80");
    //Then proceed with preparing the mask as usual
    newImage("Selection", "8-bit black", w, h, 1);
    tempID=getImageID();
    setPixel(x,y,255);
    roiManager("reset");
    selectImage(imageID2);
    makeRectangle(0, 0,w, h);
    run("Duplicate...", " ");
    tempID2=getImageID();
    run("8-bit");
    //waitForUser;
    run("Multiply...", "value=255");
    run("32-bit");
    run("Subtract...", "value=255");
    run("Square");
    run("8-bit");
    run("Fill Holes");
    //waitForUser;
    roiManager("reset");
    run("Analyze Particles...", "display add");
    //waitForUser;
    close();

```

```

        selectImage(tempID);
        run("Clear Results");
        numROIs=roiManager("count");
        for (j=0; j<numROIs; j++){
            roiManager("select", j);
            run("Measure");
        }
        close();
        selectImage(imageID2);
        run("8-bit");
        run("Multiply...", "value=255");
        if(numROIs>1){
            MaxVals=Table.getColumn("Max");
            MaxIndex=Array.findMaxima(MaxVals, 1);
            ROIInum=MaxIndex[0];
        }else{
            ROIInum=0;
        }
        roiManager("select", ROIInum);
        run("Add...", "value=255");
        run("Clear Outside");
        makeRectangle(0, 0,w, h);
        run("Subtract...", "value=200");
        run("Multiply...", "value=8");
        roiManager("deselect");
        makeRectangle(0, 0,w, h);

        run("Erode");
        roiManager("reset");
        saveAs("Tiff", output3+filebase+"_Mask.tif");
        selectImage(imageID);
        saveAs("Tiff", output1+filename);
        run("Close All");
        roiManager("reset");
    }else if(A==4){
        selectImage(imageID);
        saveAs("Tiff", output5+filename);
        run("Close All");
    }else {
        selectImage(imageID);
        saveAs("Tiff", output2+filename);
        run("Close All");
    }
}
}

```

#### 6.2.4.4 MaskApply3\_3Channel.ijm

```

input = getDirectory("Choose Target Directory (should contain a CellImages
folder): ");
parent = File.getParent(input);
target = input + "CellImages\\";
mask = parent + "\\DilatedMasks_BlackEdge\\";
output = input + "CellMasked\\";
list = getFileList(mask);
File.makeDirectory(output);

```



```

setBatchMode(true);

for (i = 0; i < list.length; i++) {
    filename=list[i];
    Matt4(target, filename);
}
function Matt4(target, filename) {
    L=lengthOf(filename);
    filebase=substring(filename,0,L-9);
    open(target+filebase + ".tif");
    run("Split Channels");
    selectImage(1);
    c2=getTitle();
    selectImage(2);
    c3=getTitle();
    selectImage(3);
    c4=getTitle();
    open(mask+filename);
    run("Divide...", "value=255");
    c1=getTitle();
    imageCalculator("Multiply", c2, c1);
    imageCalculator("Multiply", c3, c1);
    imageCalculator("Multiply", c4, c1);
    run("Merge Channels...", "c1="+c2+" c2="+c3+ " c3="+c4+" create");
    saveAs("Tiff", output+filename);
    run("Close All");
    run("Clear Results");
    roiManager("Reset");
}

```

#### **6.2.4.5 Endosome\_analysis\_for\_matlab.ijm**

```

dir1=getDirectory("Choose a Directory");
dirName = File.getName(dir1);
parent = File.getParent(dir1) + "\\";
output=parent+dirName + "_endo_ratios\\";
File.makeDirectory(output);
filelist = getFileList(dir1);
setBatchMode(true);
for (i = 0; i < lengthOf(filelist); i++) {
    if (endsWith(filelist[i], ".tif")) {
        open(dir1 + File.separator + filelist[i]);
        filename=filelist[i];
        L=lengthOf(filename);
        filebase=substring(filename,0,L-4);
        run("Split Channels");
        selectImage(1);
        ch1=getTitle();
        selectImage(2);
        ch2=getTitle();
        selectImage(3);
        ch3=getTitle();
        imageCalculator("Add create", ch1, ch2);
        imageCalculator("Add create", ch1, ch2);
        setThreshold(1,65335);
        setOption("BlackBackground", false);
    }
}

```

```

run("Convert to Mask");
rename("Mask");
roiManager("reset");
run("Analyze Particles...", "add");
close();
roiManager("select", 0);
roiManager("rename", "Cell");
imageCalculator("Divide create float", ch2, ch1);
saveAs("Tiff", output+filebase+"_Ratio.tif");
run("Set Measurements...", "integrated display redirect=None
decimal=3");
run("Merge Channels...", "c1="+ch1+" c2="+ch2+" create");
roiManager("select", 0);
run("Measure");
run("Next Slice [>]");
roiManager("select", 0);
run("Measure");
run("Close All");
}
}
saveAs("Results", parent+dirName+"_endo_ratio_vals.csv");
run("Close All");
run("Clear Results");
roiManager("reset");

```

## 7 REFERENCES

1. Kalia LV, Lang AE. Parkinson's disease. *Lancet* (London, England). 2015;386(9996):896-912. doi: 10.1016/S0140-6736(14)61393-3. PubMed PMID: 25904081.
2. Klein C, Westenberger A. Genetics of Parkinson's disease. *Cold Spring Harbor perspectives in medicine*. 2012;2(1):a008888-a. doi: 10.1101/cshperspect.a008888. PubMed PMID: 22315721; PubMed Central PMCID: PMC3253033.
3. Taymans J-M, Nkiliza A, Chartier-Harlin M-C. Deregulation of protein translation control, a potential game-changing hypothesis for Parkinson's disease pathogenesis. *Trends in molecular medicine*. 2015;21(8):466-72. doi: 10.1016/j.molmed.2015.05.004. PubMed PMID: 26091824.
4. Greggio E. Role of LRRK2 kinase activity in the pathogenesis of Parkinson's disease. *Biochemical Society Transactions*. 2012;40(5):1058-62. doi: 10.1042/BST20120054. PubMed PMID: 22988865.
5. Steger M, Tonelli F, Ito G, Davies P, Trost M, Vetter M, et al. Phosphoproteomics reveals that Parkinson's disease kinase LRRK2 regulates a subset of Rab GTPases. *eLife*. 2016;5:809. doi: 10.7554/eLife.12813. PubMed PMID: 26824392; PubMed Central PMCID: PMC4769169.
6. Bélanger M, Magistretti PJ. The role of astroglia in neuroprotection. *Dialogues in clinical neuroscience*. 2009;11(3):281-95. PubMed PMID: 19877496; PubMed Central PMCID: PMC3181926.
7. Heneka MT, Rodríguez JJ, Verkhratsky A. Neuroglia in neurodegeneration. *Brain Research Reviews*. 2010;63(1-2):189-211. doi: 10.1016/j.brainresrev.2009.11.004. PubMed PMID: 11715894136935064782related:zqQY4qQ3l6IJ.
8. Liu B, Teschemacher AG, Kasparov S. Astroglia as a cellular target for neuroprotection and treatment of neuro-psychiatric disorders. *Glia*. 2017;65(8):1205-26. doi: 10.1002/glia.23136. PubMed PMID: 28300322.
9. Liddel SA, Guttenplan KA, Clarke LE, Bennett FC, Bohlen CJ, Schirmer L, et al. Neurotoxic reactive astrocytes are induced by activated microglia. *Nature*. 2017;541(7638):481-7. doi: 10.1038/nature21029. PubMed PMID: 28099414; PubMed Central PMCID: PMC5404890.
10. Casano Alessandra M, Peri F. Microglia: Multitasking Specialists of the Brain. *Developmental Cell*. 2015;32(4):469-77. doi: <https://doi.org/10.1016/j.devcel.2015.01.018>.
11. Kierdorf K, Erny D, Goldmann T, Sander V, Schulz C, Perdiguero EG, et al. Microglia emerge from erythromyeloid precursors via Pu.1- and Irf8-dependent pathways. *Nat Neurosci*. 2013;16(3):273-80. Epub 2013/01/22. doi: 10.1038/nn.3318. PubMed PMID: 23334579.
12. Gomez Perdiguero E, Klapproth K, Schulz C, Busch K, Azzoni E, Crozet L, et al. Tissue-resident macrophages originate from yolk-sac-derived erythro-myeloid progenitors. *Nature*. 2015;518(7540):547-51. Epub 2014/12/04. doi: 10.1038/nature13989. PubMed PMID: 25470051; PubMed Central PMCID: PMC35997177.
13. Hoeffel G, Wang Y, Greter M, See P, Teo P, Malleret B, et al. Adult Langerhans cells derive predominantly from embryonic fetal liver monocytes with a minor contribution of yolk sac-derived macrophages. *J Exp Med*. 2012;209(6):1167-81. Epub 2012/05/09. doi: 10.1084/jem.20120340. PubMed PMID: 22565823; PubMed Central PMCID: PMC3371735.

14. Naito M, Hasegawa G, Ebe Y, Yamamoto T. Differentiation and function of Kupffer cells. *Med Electron Microsc.* 2004;37(1):16-28. Epub 2004/04/02. doi: 10.1007/s00795-003-0228-x. PubMed PMID: 15057601.
15. Hickman S, Izzy S, Sen P, Morsett L, El Khoury J. Microglia in neurodegeneration. *Nat Neurosci.* 2018;21(10):1359-69. Epub 2018/09/28. doi: 10.1038/s41593-018-0242-x. PubMed PMID: 30258234; PubMed Central PMCID: PMC6817969.
16. Salter MW, Beggs S. Sublime microglia: expanding roles for the guardians of the CNS. *Cell.* 2014;158(1):15-24. Epub 2014/07/06. doi: 10.1016/j.cell.2014.06.008. PubMed PMID: 24995975.
17. Calcia MA, Bonsall DR, Bloomfield PS, Selvaraj S, Barichello T, Howes OD. Stress and neuroinflammation: a systematic review of the effects of stress on microglia and the implications for mental illness. *Psychopharmacology (Berl).* 2016;233(9):1637-50. Epub 2016/02/06. doi: 10.1007/s00213-016-4218-9. PubMed PMID: 26847047; PubMed Central PMCID: PMC6817969.
18. Shabab T, Khanabdali R, Moghadamtousi SZ, Kadir HA, Mohan G. Neuroinflammation pathways: a general review. *Int J Neurosci.* 2017;127(7):624-33. Epub 2016/07/15. doi: 10.1080/00207454.2016.1212854. PubMed PMID: 27412492.
19. de la Rosa EJ, de Pablo F. Cell death in early neural development: beyond the neurotrophic theory. *Trends Neurosci.* 2000;23(10):454-8. Epub 2000/09/28. doi: 10.1016/s0166-2236(00)01628-3. PubMed PMID: 11006461.
20. Oppenheim RW. Cell Death During Development of the Nervous System. *Annual Review of Neuroscience.* 1991;14(1):453-501. doi: 10.1146/annurev.ne.14.030191.002321.
21. Hirayama D, Iida T, Nakase H. The Phagocytic Function of Macrophage-Enforcing Innate Immunity and Tissue Homeostasis. *Int J Mol Sci.* 2017;19(1). Epub 2017/12/30. doi: 10.3390/ijms19010092. PubMed PMID: 29286292; PubMed Central PMCID: PMC5796042.
22. Neumann H, Kotter MR, Franklin RJ. Debris clearance by microglia: an essential link between degeneration and regeneration. *Brain.* 2009;132(Pt 2):288-95. Epub 2008/06/24. doi: 10.1093/brain/awn109. PubMed PMID: 18567623; PubMed Central PMCID: PMC2640215.
23. Liu Y, Yang X, Guo C, Nie P, Liu Y, Ma J. Essential role of MFG-E8 for phagocytic properties of microglial cells. *PLoS One.* 2013;8(2):e55754. Epub 2013/02/14. doi: 10.1371/journal.pone.0055754. PubMed PMID: 23405209; PubMed Central PMCID: PMC3565973.
24. Gyoneva S, Orr AG, Traynelis SF. Differential regulation of microglial motility by ATP/ADP and adenosine. *Parkinsonism Relat Disord.* 2009;15 Suppl 3:S195-9. Epub 2010/01/30. doi: 10.1016/s1353-8020(09)70813-2. PubMed PMID: 20082989.
25. Chen J, Zhao Y, Liu Y. The role of nucleotides and purinergic signaling in apoptotic cell clearance - implications for chronic inflammatory diseases. *Front Immunol.* 2014;5:656. Epub 2015/01/08. doi: 10.3389/fimmu.2014.00656. PubMed PMID: 25566266; PubMed Central PMCID: PMC4274988.
26. Stock C, Schilling T, Schwab A, Eder C. Lysophosphatidylcholine stimulates IL-1beta release from microglia via a P2X7 receptor-independent mechanism. *J Immunol.* 2006;177(12):8560-8. Epub 2006/12/05. doi: 10.4049/jimmunol.177.12.8560. PubMed PMID: 17142754.

27. Hochreiter-Hufford A, Ravichandran KS. Clearing the dead: apoptotic cell sensing, recognition, engulfment, and digestion. *Cold Spring Harb Perspect Biol.* 2013;5(1):a008748. Epub 2013/01/04. doi: 10.1101/cshperspect.a008748. PubMed PMID: 23284042; PubMed Central PMCID: PMC3579390.
28. Sokolowski JD, Chabanon-Hicks CN, Han CZ, Heffron DS, Mandell JW. Fractalkine is a "find-me" signal released by neurons undergoing ethanol-induced apoptosis. *Front Cell Neurosci.* 2014;8:360. Epub 2014/11/27. doi: 10.3389/fncel.2014.00360. PubMed PMID: 25426022; PubMed Central PMCID: PMC34224129.
29. Mazaheri F, Snaidero N, Kleinberger G, Madore C, Daria A, Werner G, et al. TREM2 deficiency impairs chemotaxis and microglial responses to neuronal injury. *EMBO Rep.* 2017;18(7):1186-98. Epub 2017/05/10. doi: 10.15252/embr.201743922. PubMed PMID: 28483841; PubMed Central PMCID: PMC5494532.
30. Hadas S, Spira M, Hanisch UK, Reichert F, Rotshenker S. Complement receptor-3 negatively regulates the phagocytosis of degenerated myelin through tyrosine kinase Syk and cofilin. *J Neuroinflammation.* 2012;9:166. Epub 2012/07/11. doi: 10.1186/1742-2094-9-166. PubMed PMID: 22776089; PubMed Central PMCID: PMC3418574.
31. Fricker M, Oliva-Martín MJ, Brown GC. Primary phagocytosis of viable neurons by microglia activated with LPS or A $\beta$  is dependent on calreticulin/LRP phagocytic signalling. *J Neuroinflammation.* 2012;9:196. Epub 2012/08/15. doi: 10.1186/1742-2094-9-196. PubMed PMID: 22889139; PubMed Central PMCID: PMC3481398.
32. Lannes N, Eppler E, Etemad S, Yotovskii P, Filgueira L. Microglia at center stage: a comprehensive review about the versatile and unique residential macrophages of the central nervous system. *Oncotarget.* 2017;8(69):114393-413. Epub 2018/01/27. doi: 10.18632/oncotarget.23106. PubMed PMID: 29371994; PubMed Central PMCID: PMC5768411.
33. Brown GC, Neher JJ. Microglial phagocytosis of live neurons. *Nat Rev Neurosci.* 2014;15(4):209-16. Epub 2014/03/22. doi: 10.1038/nrn3710. PubMed PMID: 24646669.
34. Neher JJ, Neniskyte U, Zhao J-W, Bal-Price A, Tolkovsky AM, Brown GC. Inhibition of microglial phagocytosis is sufficient to prevent inflammatory neuronal death. *Journal of immunology (Baltimore, Md : 1950).* 2011;186(8):4973-83. doi: 10.4049/jimmunol.1003600. PubMed PMID: 21402900.
35. Hickman SE, Kingery ND, Ohsumi TK, Borowsky ML, Wang LC, Means TK, et al. The microglial sensome revealed by direct RNA sequencing. *Nat Neurosci.* 2013;16(12):1896-905. Epub 2013/10/29. doi: 10.1038/nn.3554. PubMed PMID: 24162652; PubMed Central PMCID: PMC3840123.
36. Lyman M, Lloyd DG, Ji X, Vizcaychipi MP, Ma D. Neuroinflammation: the role and consequences. *Neurosci Res.* 2014;79:1-12. Epub 2013/10/23. doi: 10.1016/j.neures.2013.10.004. PubMed PMID: 24144733.
37. Brown GC, Vilalta A. How microglia kill neurons. *Brain Res.* 2015;1628(Pt B):288-97. Epub 2015/09/06. doi: 10.1016/j.brainres.2015.08.031. PubMed PMID: 26341532.
38. Biber K, Owens T, Boddeke E. What is microglia neurotoxicity (Not)? *Glia.* 2014;62(6):841-54. Epub 2014/03/05. doi: 10.1002/glia.22654. PubMed PMID: 24590682.

39. Liu B, Hong JS. Role of microglia in inflammation-mediated neurodegenerative diseases: mechanisms and strategies for therapeutic intervention. *J Pharmacol Exp Ther.* 2003;304(1):1-7. Epub 2002/12/20. doi: 10.1124/jpet.102.035048. PubMed PMID: 12490568.
40. Zhang J-M, An J. Cytokines, inflammation, and pain. *Int Anesthesiol Clin.* 2007;45(2):27-37. doi: 10.1097/AIA.0b013e318034194e. PubMed PMID: 17426506.
41. Kingham PJ, Pocock JM. Microglial secreted cathepsin B induces neuronal apoptosis. *J Neurochem.* 2001;76(5):1475-84. Epub 2001/03/10. doi: 10.1046/j.1471-4159.2001.00146.x. PubMed PMID: 11238732.
42. Taylor DL, Jones F, Kubota ESFCS, Pocock JM. Stimulation of Microglial Metabotropic Glutamate Receptor mGlu2 Triggers Tumor Necrosis Factor  $\alpha$ -Induced Neurotoxicity in Concert with Microglial-Derived Fas Ligand. *The Journal of Neuroscience.* 2005;25(11):2952. doi: 10.1523/JNEUROSCI.4456-04.2005.
43. Mander P, Brown GC. Activation of microglial NADPH oxidase is synergistic with glial iNOS expression in inducing neuronal death: a dual-key mechanism of inflammatory neurodegeneration. *J Neuroinflammation.* 2005;2:20. Epub 2005/09/15. doi: 10.1186/1742-2094-2-20. PubMed PMID: 16156895; PubMed Central PMCID: PMC1232863.
44. Chhor V, Le Charpentier T, Lebon S, Oré MV, Celador IL, Jossierand J, et al. Characterization of phenotype markers and neuronotoxic potential of polarised primary microglia in vitro. *Brain Behav Immun.* 2013;32:70-85. Epub 2013/03/05. doi: 10.1016/j.bbi.2013.02.005. PubMed PMID: 23454862; PubMed Central PMCID: PMC3694309.
45. Venegas C, Kumar S, Franklin BS, Dierkes T, Brinkschulte R, Tejera D, et al. Microglia-derived ASC specks cross-seed amyloid- $\beta$  in Alzheimer's disease. *Nature.* 2017;552(7685):355-61. Epub 2018/01/03. doi: 10.1038/nature25158. PubMed PMID: 29293211.
46. Villemagne VL, Doré V, Bourgeat P, Burnham SC, Laws S, Salvado O, et al. A $\beta$ -amyloid and Tau Imaging in Dementia. *Semin Nucl Med.* 2017;47(1):75-88. Epub 2016/12/19. doi: 10.1053/j.semnuclmed.2016.09.006. PubMed PMID: 27987560.
47. Oddo S, Caccamo A, Kitazawa M, Tseng BP, LaFerla FM. Amyloid deposition precedes tangle formation in a triple transgenic model of Alzheimer's disease. *Neurobiol Aging.* 2003;24(8):1063-70. Epub 2003/12/04. doi: 10.1016/j.neurobiolaging.2003.08.012. PubMed PMID: 14643377.
48. Ransohoff RM, El Khoury J. Microglia in Health and Disease. *Cold Spring Harb Perspect Biol.* 2015;8(1):a020560. Epub 2015/09/12. doi: 10.1101/cshperspect.a020560. PubMed PMID: 26354893; PubMed Central PMCID: PMC4691795.
49. Apolloni S, Amadio S, Montilli C, Volonté C, D'Ambrosi N. Ablation of P2X7 receptor exacerbates gliosis and motoneuron death in the SOD1-G93A mouse model of amyotrophic lateral sclerosis. *Hum Mol Genet.* 2013;22(20):4102-16. Epub 2013/06/06. doi: 10.1093/hmg/ddt259. PubMed PMID: 23736299.
50. Yamanaka K, Boillee S, Roberts EA, Garcia ML, McAlonis-Downes M, Mikse OR, et al. Mutant SOD1 in cell types other than motor neurons and oligodendrocytes accelerates onset of disease in ALS mice. *Proc Natl Acad Sci U S A.* 2008;105(21):7594-9. Epub 2008/05/22. doi: 10.1073/pnas.0802556105. PubMed PMID: 18492803; PubMed Central PMCID: PMC2396671.

51. Crotti A, Benner C, Kerman BE, Gosselin D, Lagier-Tourenne C, Zuccato C, et al. Mutant Huntingtin promotes autonomous microglia activation via myeloid lineage-determining factors. *Nat Neurosci*. 2014;17(4):513-21. Epub 2014/03/04. doi: 10.1038/nn.3668. PubMed PMID: 24584051; PubMed Central PMCID: PMC4113004.
52. Sorce S, Nuvolone M, Keller A, Falsig J, Varol A, Schwarz P, et al. The role of the NADPH oxidase NOX2 in prion pathogenesis. *PLoS Pathog*. 2014;10(12):e1004531. Epub 2014/12/17. doi: 10.1371/journal.ppat.1004531. PubMed PMID: 25502554; PubMed Central PMCID: PMC4263757 adherence to all PLOS Pathogens policies on sharing data and materials.
53. Gerhard A, Pavese N, Hotton G, Turkheimer F, Es M, Hammers A, et al. In vivo imaging of microglial activation with [11C](R)-PK11195 PET in idiopathic Parkinson's disease. *Neurobiol Dis*. 2006;21(2):404-12. Epub 2005/09/27. doi: 10.1016/j.nbd.2005.08.002. PubMed PMID: 16182554.
54. McGeer PL, Itagaki S, Boyes BE, McGeer EG. Reactive microglia are positive for HLA-DR in the substantia nigra of Parkinson's and Alzheimer's disease brains. *Neurology*. 1988;38(8):1285-91. Epub 1988/08/01. doi: 10.1212/wnl.38.8.1285. PubMed PMID: 3399080.
55. Su X, Maguire-Zeiss KA, Giuliano R, Prifti L, Venkatesh K, Federoff HJ. Synuclein activates microglia in a model of Parkinson's disease. *Neurobiol Aging*. 2008;29(11):1690-701. Epub 2007/06/01. doi: 10.1016/j.neurobiolaging.2007.04.006. PubMed PMID: 17537546; PubMed Central PMCID: PMC2621109.
56. Croisier E, Moran LB, Dexter DT, Pearce RK, Graeber MB. Microglial inflammation in the parkinsonian substantia nigra: relationship to alpha-synuclein deposition. *J Neuroinflammation*. 2005;2:14. Epub 2005/06/07. doi: 10.1186/1742-2094-2-14. PubMed PMID: 15935098; PubMed Central PMCID: PMC1177985.
57. Stefanis L.  $\alpha$ -Synuclein in Parkinson's disease. *Cold Spring Harbor perspectives in medicine*. 2012;2(2):a009399-a. doi: 10.1101/cshperspect.a009399. PubMed PMID: 22355802.
58. Xu L, Pu J. Alpha-Synuclein in Parkinson's Disease: From Pathogenetic Dysfunction to Potential Clinical Application. *Parkinsons Dis*. 2016;2016:1720621-. Epub 2016/08/17. doi: 10.1155/2016/1720621. PubMed PMID: 27610264.
59. Shulman JM, De Jager PL, Feany MB. Parkinson's disease: genetics and pathogenesis. *Annual review of pathology*. 2011;6(1):193-222. doi: 10.1146/annurev-pathol-011110-130242. PubMed PMID: 21034221.
60. Haugarvoll K, Wszolek ZK. Clinical features of LRRK2 parkinsonism. *Parkinsonism Relat Disord*. 2009;15 Suppl 3:S205-8. Epub 2010/01/30. doi: 10.1016/s1353-8020(09)70815-6. PubMed PMID: 20082991.
61. Berwick DC, Heaton GR, Azeggagh S, Harvey K. LRRK2 Biology from structure to dysfunction: research progresses, but the themes remain the same. *Molecular Neurodegeneration*. 2019;14(1):49. doi: 10.1186/s13024-019-0344-2.
62. Cookson MR. LRRK2 Pathways Leading to Neurodegeneration. *Curr Neurol Neurosci Rep*. 2015;15(7):42. Epub 2015/05/27. doi: 10.1007/s11910-015-0564-y. PubMed PMID: 26008812; PubMed Central PMCID: PMC45839465.
63. Nixon-Abell J, Berwick DC, Harvey K. L'RRK de Triomphe: a solution for LRRK2 GTPase activity? *Biochem Soc Trans*. 2016;44(6):1625-34. Epub 2016/12/04. doi: 10.1042/bst20160240. PubMed PMID: 27913671.

64. Sheng Z, Zhang S, Bustos D, Kleinheinz T, Le Pichon CE, Dominguez SL, et al. Ser1292 autophosphorylation is an indicator of LRRK2 kinase activity and contributes to the cellular effects of PD mutations. *Sci Transl Med*. 2012;4(164):164ra1. Epub 2012/12/18. doi: 10.1126/scitranslmed.3004485. PubMed PMID: 23241745.
65. Steger M, Diez F, Dhekne HS, Lis P, Nirujogi RS, Karayel O, et al. Systematic proteomic analysis of LRRK2-mediated Rab GTPase phosphorylation establishes a connection to ciliogenesis. *Elife*. 2017;6. Epub 2017/11/11. doi: 10.7554/eLife.31012. PubMed PMID: 29125462; PubMed Central PMCID: PMC5695910.
66. Madero-Pérez J, Fdez E, Fernández B, Lara Ordóñez AJ, Blanca Ramírez M, Gómez-Suaga P, et al. Parkinson disease-associated mutations in LRRK2 cause centrosomal defects via Rab8a phosphorylation. *Mol Neurodegener*. 2018;13(1):3. Epub 2018/01/24. doi: 10.1186/s13024-018-0235-y. PubMed PMID: 29357897; PubMed Central PMCID: PMC5778812.
67. Greggio E, Cookson MR. Leucine-rich repeat kinase 2 mutations and Parkinson's disease: three questions. *ASN Neuro*. 2009;1(1). Epub 2009/07/03. doi: 10.1042/an20090007. PubMed PMID: 19570025; PubMed Central PMCID: PMC2695577.
68. Tong Y, Yamaguchi H, Giaime E, Boyle S, Kopan R, Kelleher RJ, 3rd, et al. Loss of leucine-rich repeat kinase 2 causes impairment of protein degradation pathways, accumulation of alpha-synuclein, and apoptotic cell death in aged mice. *Proc Natl Acad Sci U S A*. 2010;107(21):9879-84. Epub 2010/05/12. doi: 10.1073/pnas.1004676107. PubMed PMID: 20457918; PubMed Central PMCID: PMC2906862.
69. Manzoni C, Mamais A, Dihanich S, Abeti R, Soutar MPM, Plun-Favreau H, et al. Inhibition of LRRK2 kinase activity stimulates macroautophagy. *Biochim Biophys Acta*. 2013;1833(12):2900-10. Epub 2013/08/07. doi: 10.1016/j.bbamcr.2013.07.020. PubMed PMID: 23916833; PubMed Central PMCID: PMC3898616.
70. Saez-Atienzar S, Bonet-Ponce L, Blesa JR, Romero FJ, Murphy MP, Jordan J, et al. The LRRK2 inhibitor GSK2578215A induces protective autophagy in SH-SY5Y cells: involvement of Drp-1-mediated mitochondrial fission and mitochondrial-derived ROS signaling. *Cell Death Dis*. 2014;5(8):e1368. Epub 2014/08/15. doi: 10.1038/cddis.2014.320. PubMed PMID: 25118928; PubMed Central PMCID: PMC4454299.
71. Manzoni C, Mamais A, Roosen DA, Dihanich S, Soutar MP, Plun-Favreau H, et al. mTOR independent regulation of macroautophagy by Leucine Rich Repeat Kinase 2 via Beclin-1. *Sci Rep*. 2016;6:35106. Epub 2016/10/13. doi: 10.1038/srep35106. PubMed PMID: 27731364; PubMed Central PMCID: PMC5059726.
72. Schapansky J, Nardozi JD, Felizia F, LaVoie MJ. Membrane recruitment of endogenous LRRK2 precedes its potent regulation of autophagy. *Hum Mol Genet*. 2014;23(16):4201-14. Epub 2014/04/01. doi: 10.1093/hmg/ddu138. PubMed PMID: 24682598; PubMed Central PMCID: PMC4103671.
73. Cherra SJ, 3rd, Kulich SM, Uechi G, Balasubramani M, Mountzouris J, Day BW, et al. Regulation of the autophagy protein LC3 by phosphorylation. *J Cell Biol*. 2010;190(4):533-9. Epub 2010/08/18. doi: 10.1083/jcb.201002108. PubMed PMID: 20713600; PubMed Central PMCID: PMC2928022.
74. Plowey ED, Cherra SJ, 3rd, Liu YJ, Chu CT. Role of autophagy in G2019S-LRRK2-associated neurite shortening in differentiated SH-SY5Y cells. *J Neurochem*. 2008;105(3):1048-56. Epub



2008/01/10. doi: 10.1111/j.1471-4159.2008.05217.x. PubMed PMID: 18182054; PubMed Central PMCID: PMCPMC2361385.

75. Gómez-Suaga P, Luzón-Toro B, Churamani D, Zhang L, Bloor-Young D, Patel S, et al. Leucine-rich repeat kinase 2 regulates autophagy through a calcium-dependent pathway involving NAADP. *Hum Mol Genet.* 2012;21(3):511-25. Epub 2011/10/21. doi: 10.1093/hmg/ddr481. PubMed PMID: 22012985; PubMed Central PMCID: PMCPMC3259011.
76. Manzoni C, Mamais A, Dihanich S, McGoldrick P, Devine MJ, Zerle J, et al. Pathogenic Parkinson's disease mutations across the functional domains of LRRK2 alter the autophagic/lysosomal response to starvation. *Biochem Biophys Res Commun.* 2013;441(4):862-6. Epub 2013/11/12. doi: 10.1016/j.bbrc.2013.10.159. PubMed PMID: 24211199; PubMed Central PMCID: PMCPMC3858825.
77. Schapansky J, Khasnavis S, DeAndrade MP, Nardozi JD, Falkson SR, Boyd JD, et al. Familial knockin mutation of LRRK2 causes lysosomal dysfunction and accumulation of endogenous insoluble  $\alpha$ -synuclein in neurons. *Neurobiol Dis.* 2018;111:26-35. Epub 2017/12/17. doi: 10.1016/j.nbd.2017.12.005. PubMed PMID: 29246723; PubMed Central PMCID: PMCPMC5803451.
78. Shin N, Jeong H, Kwon J, Heo HY, Kwon JJ, Yun HJ, et al. LRRK2 regulates synaptic vesicle endocytosis. *Exp Cell Res.* 2008;314(10):2055-65. Epub 2008/05/01. doi: 10.1016/j.yexcr.2008.02.015. PubMed PMID: 18445495.
79. Arranz AM, Delbroek L, Van Kolen K, Guimarães MR, Mandemakers W, Daneels G, et al. LRRK2 functions in synaptic vesicle endocytosis through a kinase-dependent mechanism. *J Cell Sci.* 2015;128(3):541-52. Epub 2014/12/17. doi: 10.1242/jcs.158196. PubMed PMID: 25501810.
80. Matta S, Van Kolen K, da Cunha R, van den Bogaart G, Mandemakers W, Miskiewicz K, et al. LRRK2 controls an EndoA phosphorylation cycle in synaptic endocytosis. *Neuron.* 2012;75(6):1008-21. Epub 2012/09/25. doi: 10.1016/j.neuron.2012.08.022. PubMed PMID: 22998870.
81. Cirnaru MD, Marte A, Belluzzi E, Russo I, Gabrielli M, Longo F, et al. LRRK2 kinase activity regulates synaptic vesicle trafficking and neurotransmitter release through modulation of LRRK2 macro-molecular complex. *Front Mol Neurosci.* 2014;7:49. Epub 2014/06/07. doi: 10.3389/fnmol.2014.00049. PubMed PMID: 24904275; PubMed Central PMCID: PMCPMC4034499.
82. Gómez-Suaga P, Rivero-Ríos P, Fdez E, Blanca Ramírez M, Ferrer I, Aiausti A, et al. LRRK2 delays degradative receptor trafficking by impeding late endosomal budding through decreasing Rab7 activity. *Hum Mol Genet.* 2014;23(25):6779-96. Epub 2014/08/01. doi: 10.1093/hmg/ddu395. PubMed PMID: 25080504.
83. Rivero-Ríos P, Romo-Lozano M, Madero-Pérez J, Thomas AP, Biosa A, Greggio E, et al. The G2019S variant of leucine-rich repeat kinase 2 (LRRK2) alters endolysosomal trafficking by impairing the function of the GTPase RAB8A. *J Biol Chem.* 2019;294(13):4738-58. Epub 2019/02/03. doi: 10.1074/jbc.RA118.005008. PubMed PMID: 30709905; PubMed Central PMCID: PMCPMC6442034.
84. Eguchi T, Kuwahara T, Sakurai M, Komori T, Fujimoto T, Ito G, et al. LRRK2 and its substrate Rab GTPases are sequentially targeted onto stressed lysosomes and maintain their homeostasis. *Proc Natl Acad Sci U S A.* 2018;115(39):E9115-e24. Epub 2018/09/14. doi:

- 10.1073/pnas.1812196115. PubMed PMID: 30209220; PubMed Central PMCID: PMC6166828.
85. Dodson MW, Zhang T, Jiang C, Chen S, Guo M. Roles of the *Drosophila* LRRK2 homolog in Rab7-dependent lysosomal positioning. *Hum Mol Genet.* 2012;21(6):1350-63. Epub 2011/12/16. doi: 10.1093/hmg/ddr573. PubMed PMID: 22171073; PubMed Central PMCID: PMC6166828.
86. Härtlova A, Herbst S, Peltier J, Rodgers A, Bilkei-Gorzo O, Fearn A, et al. LRRK2 is a negative regulator of *Mycobacterium tuberculosis* phagosome maturation in macrophages. *Embo j.* 2018;37(12). Epub 2018/05/24. doi: 10.15252/emboj.201798694. PubMed PMID: 29789389; PubMed Central PMCID: PMC6003659.
87. Kim KS, Marcogliese PC, Yang J, Callaghan SM, Resende V, Abdel-Messih E, et al. Regulation of myeloid cell phagocytosis by LRRK2 via WAVE2 complex stabilization is altered in Parkinson's disease. *Proceedings of the National Academy of Sciences.* 2018;115(22):E5164. doi: 10.1073/pnas.1718946115.
88. Marker DF, Puccini JM, Mockus TE, Barbieri J, Lu S-M, Gelbard HA. LRRK2 kinase inhibition prevents pathological microglial phagocytosis in response to HIV-1 Tat protein. *Journal of Neuroinflammation.* 2012;9(1):261. doi: 10.1186/1742-2094-9-261.
89. Yu M, Arshad M, Wang W, Zhao D, Xu L, Zhou L. LRRK2 mediated Rab8a phosphorylation promotes lipid storage. *Lipids Health Dis.* 2018;17(1):34. Epub 2018/02/28. doi: 10.1186/s12944-018-0684-x. PubMed PMID: 29482628; PubMed Central PMCID: PMC5828482.
90. Baptista MA, Dave KD, Frasier MA, Sherer TB, Greeley M, Beck MJ, et al. Loss of leucine-rich repeat kinase 2 (LRRK2) in rats leads to progressive abnormal phenotypes in peripheral organs. *PLoS One.* 2013;8(11):e80705. Epub 2013/11/19. doi: 10.1371/journal.pone.0080705. PubMed PMID: 24244710; PubMed Central PMCID: PMC3828242 entirely service organization. WIL Research has no financial or any other competing interests in the results of the studies reported in this manuscript and this does not alter our adherence to all the PLOS ONE policies on sharing data and materials.
91. Ng CH, Mok SZ, Koh C, Ouyang X, Fivaz ML, Tan EK, et al. Parkin protects against LRRK2 G2019S mutant-induced dopaminergic neurodegeneration in *Drosophila*. *J Neurosci.* 2009;29(36):11257-62. Epub 2009/09/11. doi: 10.1523/jneurosci.2375-09.2009. PubMed PMID: 19741132; PubMed Central PMCID: PMC2771772.
92. Karuppagounder SS, Xiong Y, Lee Y, Lawless MC, Kim D, Nordquist E, et al. LRRK2 G2019S transgenic mice display increased susceptibility to 1-methyl-4-phenyl-1,2,3,6-tetrahydropyridine (MPTP)-mediated neurotoxicity. *J Chem Neuroanat.* 2016;76(Pt B):90-7. Epub 2016/01/26. doi: 10.1016/j.jchemneu.2016.01.007. PubMed PMID: 26808467; PubMed Central PMCID: PMC4958044.
93. Nguyen HN, Byers B, Cord B, Shcheglovitov A, Byrne J, Gujar P, et al. LRRK2 mutant iPSC-derived DA neurons demonstrate increased susceptibility to oxidative stress. *Cell Stem Cell.* 2011;8(3):267-80. Epub 2011/03/03. doi: 10.1016/j.stem.2011.01.013. PubMed PMID: 21362567; PubMed Central PMCID: PMC3578553.
94. Cooper O, Seo H, Andrabi S, Guardia-Laguarta C, Graziotto J, Sundberg M, et al. Pharmacological rescue of mitochondrial deficits in iPSC-derived neural cells from patients with familial Parkinson's disease. *Sci Transl Med.* 2012;4(141):141ra90. Epub 2012/07/06. doi:

- 10.1126/scitranslmed.3003985. PubMed PMID: 22764206; PubMed Central PMCID: PMC3462009.
95. Mortiboys H, Furnston R, Bronstad G, Aasly J, Elliott C, Bandmann O. UDCA exerts beneficial effect on mitochondrial dysfunction in LRRK2(G2019S) carriers and in vivo. *Neurology*. 2015;85(10):846-52. Epub 2015/08/09. doi: 10.1212/wnl.0000000000001905. PubMed PMID: 26253449; PubMed Central PMCID: PMC4560055.
96. Yue M, Hinkle KM, Davies P, Trushina E, Fiesel FC, Christenson TA, et al. Progressive dopaminergic alterations and mitochondrial abnormalities in LRRK2 G2019S knock-in mice. *Neurobiol Dis*. 2015;78:172-95. Epub 2015/04/04. doi: 10.1016/j.nbd.2015.02.031. PubMed PMID: 25836420; PubMed Central PMCID: PMC4526103.
97. Smith GA, Jansson J, Rocha EM, Osborn T, Hallett PJ, Isacson O. Fibroblast Biomarkers of Sporadic Parkinson's Disease and LRRK2 Kinase Inhibition. *Mol Neurobiol*. 2016;53(8):5161-77. Epub 2015/09/25. doi: 10.1007/s12035-015-9435-4. PubMed PMID: 26399642; PubMed Central PMCID: PMC45012155.
98. Grünewald A, Arns B, Meier B, Brockmann K, Tadic V, Klein C. Does uncoupling protein 2 expression qualify as marker of disease status in LRRK2-associated Parkinson's disease? *Antioxid Redox Signal*. 2014;20(13):1955-60. Epub 2013/11/21. doi: 10.1089/ars.2013.5737. PubMed PMID: 24251413; PubMed Central PMCID: PMC3993019.
99. Hsieh CH, Shaltouki A, Gonzalez AE, Bettencourt da Cruz A, Burbulla LF, St Lawrence E, et al. Functional Impairment in Miro Degradation and Mitophagy Is a Shared Feature in Familial and Sporadic Parkinson's Disease. *Cell Stem Cell*. 2016;19(6):709-24. Epub 2016/09/13. doi: 10.1016/j.stem.2016.08.002. PubMed PMID: 27618216; PubMed Central PMCID: PMC5135570.
100. Gloeckner CJ, Kinkl N, Schumacher A, Braun RJ, O'Neill E, Meitinger T, et al. The Parkinson disease causing LRRK2 mutation I2020T is associated with increased kinase activity. *Hum Mol Genet*. 2006;15(2):223-32. Epub 2005/12/03. doi: 10.1093/hmg/ddi439. PubMed PMID: 16321986.
101. Biskup S, Moore DJ, Celsi F, Higashi S, West AB, Andrabi SA, et al. Localization of LRRK2 to membranous and vesicular structures in mammalian brain. *Ann Neurol*. 2006;60(5):557-69. Epub 2006/11/23. doi: 10.1002/ana.21019. PubMed PMID: 17120249.
102. Law BM, Spain VA, Leinster VH, Chia R, Beilina A, Cho HJ, et al. A direct interaction between leucine-rich repeat kinase 2 and specific  $\beta$ -tubulin isoforms regulates tubulin acetylation. *J Biol Chem*. 2014;289(2):895-908. Epub 2013/11/28. doi: 10.1074/jbc.M113.507913. PubMed PMID: 24275654; PubMed Central PMCID: PMC3887213.
103. Pellegrini L, Hauser DN, Li Y, Mamais A, Beilina A, Kumaran R, et al. Proteomic analysis reveals co-ordinated alterations in protein synthesis and degradation pathways in LRRK2 knockout mice. *Hum Mol Genet*. 2018;27(18):3257-71. Epub 2018/06/20. doi: 10.1093/hmg/ddy232. PubMed PMID: 29917075; PubMed Central PMCID: PMC6121185.
104. Godena VK, Brookes-Hocking N, Moller A, Shaw G, Oswald M, Sancho RM, et al. Increasing microtubule acetylation rescues axonal transport and locomotor deficits caused by LRRK2 Roc-COR domain mutations. *Nat Commun*. 2014;5:5245. Epub 2014/10/16. doi: 10.1038/ncomms6245. PubMed PMID: 25316291; PubMed Central PMCID: PMC4208097.

105. Madero-Pérez J, Fernández B, Lara Ordóñez AJ, Fdez E, Lobbestael E, Baekelandt V, et al. RAB7L1-Mediated Relocalization of LRRK2 to the Golgi Complex Causes Centrosomal Deficits via RAB8A. *Front Mol Neurosci*. 2018;11:417. Epub 2018/11/30. doi: 10.3389/fnmol.2018.00417. PubMed PMID: 30483055; PubMed Central PMCID: PMC6243087.
106. Gillardon F, Schmid R, Draheim H. Parkinson's disease-linked leucine-rich repeat kinase 2(R1441G) mutation increases proinflammatory cytokine release from activated primary microglial cells and resultant neurotoxicity. *Neuroscience*. 2012;208:41-8. Epub 2012/02/22. doi: 10.1016/j.neuroscience.2012.02.001. PubMed PMID: 22342962.
107. Moehle MS, Webber PJ, Tse T, Sukar N, Standaert DG, DeSilva TM, et al. LRRK2 inhibition attenuates microglial inflammatory responses. *J Neurosci*. 2012;32(5):1602-11. Epub 2012/02/04. doi: 10.1523/jneurosci.5601-11.2012. PubMed PMID: 22302802; PubMed Central PMCID: PMC3532034.
108. Fan Y, Howden AJM, Sarhan AR, Lis P, Ito G, Martinez TN, et al. Interrogating Parkinson's disease LRRK2 kinase pathway activity by assessing Rab10 phosphorylation in human neutrophils. *Biochemical Journal*. 2018;475(1):23-44. doi: 10.1042/BCJ20170803.
109. Thévenet J, Pescini Gobert R, Hooft van Huijsduijnen R, Wiessner C, Sagot YJ. Regulation of LRRK2 expression points to a functional role in human monocyte maturation. *PLoS One*. 2011;6(6):e21519. Epub 2011/07/09. doi: 10.1371/journal.pone.0021519. PubMed PMID: 21738687; PubMed Central PMCID: PMC3124520 alter the authors' adherence to all the PLoS ONE policies on sharing data and materials.
110. Liu Z, Lee J, Krummey S, Lu W, Cai H, Lenardo MJ. The kinase LRRK2 is a regulator of the transcription factor NFAT that modulates the severity of inflammatory bowel disease. *Nat Immunol*. 2011;12(11):1063-70. Epub 2011/10/11. doi: 10.1038/ni.2113. PubMed PMID: 21983832; PubMed Central PMCID: PMC4140245.
111. Gardet A, Benita Y, Li C, Sands BE, Ballester I, Stevens C, et al. LRRK2 is involved in the IFN-gamma response and host response to pathogens. *J Immunol*. 2010;185(9):5577-85. Epub 2010/10/06. doi: 10.4049/jimmunol.1000548. PubMed PMID: 20921534; PubMed Central PMCID: PMC3156100.
112. Dzamko N, Inesta-Vaquera F, Zhang J, Xie C, Cai H, Arthur S, et al. The IkappaB kinase family phosphorylates the Parkinson's disease kinase LRRK2 at Ser935 and Ser910 during Toll-like receptor signaling. *PLoS One*. 2012;7(6):e39132. Epub 2012/06/23. doi: 10.1371/journal.pone.0039132. PubMed PMID: 22723946; PubMed Central PMCID: PMC3377608 pharmaceutical companies supporting the Division of Signal Transduction Therapy Unit (AstraZeneca, Boehringer-Ingelheim, GlaxoSmithKline, Janssen Pharmaceutica; Merck KgaA and Pfizer) for financial support. I can also confirm that this does not alter our adherence to all the PLoS ONE policies on sharing data and materials.
113. Liu W, Liu X, Li Y, Zhao J, Liu Z, Hu Z, et al. LRRK2 promotes the activation of NLRC4 inflammasome during Salmonella Typhimurium infection. *J Exp Med*. 2017;214(10):3051-66. Epub 2017/08/20. doi: 10.1084/jem.20170014. PubMed PMID: 28821568; PubMed Central PMCID: PMC5626397.
114. Weindel CG, Bell SL, Vail KJ, West KO, Patrick KL, Watson RO. LRRK2 maintains mitochondrial homeostasis and regulates innate immune responses to Mycobacterium tuberculosis. *Elife*. 2020;9. Epub 2020/02/15. doi: 10.7554/eLife.51071. PubMed PMID: 32057291; PubMed Central PMCID: PMC7159881.

115. Russo I, Berti G, Plotegher N, Bernardo G, Filograna R, Bubacco L, et al. Leucine-rich repeat kinase 2 positively regulates inflammation and down-regulates NF- $\kappa$ B p50 signaling in cultured microglia cells. *J Neuroinflammation*. 2015;12:230. Epub 2015/12/10. doi: 10.1186/s12974-015-0449-7. PubMed PMID: 26646749; PubMed Central PMCID: PMC4673731.
116. Araki M, Ito G, Tomita T. Physiological and pathological functions of LRRK2: implications from substrate proteins. *Neuronal Signaling*. 2018;2(4). doi: 10.1042/NS20180005.
117. Matikainen-Ankney BA, Kezunovic N, Mesias RE, Tian Y, Williams FM, Huntley GW, et al. Altered Development of Synapse Structure and Function in Striatum Caused by Parkinson's Disease-Linked LRRK2-G2019S Mutation. *Journal of Neuroscience*. 2016;36(27):7128-41. doi: 10.1523/JNEUROSCI.3314-15.2016. PubMed PMID: 27383589; PubMed Central PMCID: PMC4938860.
118. Bohlen CJ, Bennett FC, Tucker AF, Collins HY, Mulinyawe SB, Barres BA. Diverse Requirements for Microglial Survival, Specification, and Function Revealed by Defined-Medium Cultures. *Neuron*. 2017;94(4):759-73.e8. doi: 10.1016/j.neuron.2017.04.043. PubMed PMID: 0FCA9A75-3AE5-404A-9967-BE01855D8D34.
119. di Domenico A, Carola G, Calatayud C, Pons-Espinal M, Muñoz JP, Richaud-Patin Y, et al. Patient-Specific iPSC-Derived Astrocytes Contribute to Non-Cell-Autonomous Neurodegeneration in Parkinson's Disease. *Stem Cell Reports*. 2019;12(2):213-29. doi: 10.1016/j.stemcr.2018.12.011. PubMed PMID: 30639209; PubMed Central PMCID: PMC6372974.
120. Rottet S, Besagni C, Kessler F. The role of plastoglobules in thylakoid lipid remodeling during plant development. *Biochimica et Biophysica Acta (BBA) - Bioenergetics*. 2015;1847(9):889-99. doi: <https://doi.org/10.1016/j.bbabi.2015.02.002>.
121. Vishnevetsky M, Ovadis M, Vainstein A. Carotenoid sequestration in plants: the role of carotenoid-associated proteins. *Trends in Plant Science*. 1999;4(6):232-5. doi: [https://doi.org/10.1016/S1360-1385\(99\)01414-4](https://doi.org/10.1016/S1360-1385(99)01414-4).
122. Deruère J, Römer S, Harlingue A, Backhaus RA, Kuntz M, Camara B. Fibril assembly and carotenoid overaccumulation in chromoplasts: a model for supramolecular lipoprotein structures. *The Plant Cell*. 1994;6(1):119. doi: 10.1105/tpc.6.1.119.
123. Liu L. Ultrastructural study on dynamics of lipid bodies and plastids during ripening of chili pepper fruits. *Micron*. 2013;46:43-50. Epub 2013/01/08. doi: 10.1016/j.micron.2012.12.004. PubMed PMID: 23290710.
124. Abud EM, Ramirez RN, Martinez ES, Healy LM, Nguyen CHH, Newman SA, et al. iPSC-Derived Human Microglia-like Cells to Study Neurological Diseases. *Neuron*. 2017;94(2):278-93.e9. doi: 10.1016/j.neuron.2017.03.042. PubMed PMID: 10.1016/j.neuron.2017.03.042.
125. Kriks S, Shim J-w, Piao J, Ganat YM, Wakeman DR, Xie Z, et al. Dopamine neurons derived from human ES cells efficiently engraft in animal models of Parkinson's disease. *Nature*. 2011;480(7378):547-51. doi: 10.1038/nature10648. PubMed PMID: 22056989; PubMed Central PMCID: PMC3245796.
126. Bennett ML, Bennett FC, Liddel SA, Ajami B, Zamanian JL, Fernhoff NB, et al. New tools for studying microglia in the mouse and human CNS. *Proceedings of the National Academy of Sciences of the United States of America*. 2016;113(12):E1738-46. doi:

- 10.1073/pnas.1525528113. PubMed PMID: 26884166; PubMed Central PMCID: PMC4812770.
127. Montilla A, Zabala A, Matute C, Domercq M. Functional and Metabolic Characterization of Microglia Culture in a Defined Medium. *Frontiers in Cellular Neuroscience*. 2020;14(22). doi: 10.3389/fncel.2020.00022.
128. Yu AC, Neil SE, Quandt JA. High yield primary microglial cultures using granulocyte macrophage-colony stimulating factor from embryonic murine cerebral cortical tissue. *Journal of Neuroimmunology*. 2017;307:53-62. doi: <https://doi.org/10.1016/j.jneuroim.2017.03.018>.
129. Lawson LJ, Perry VH, Gordon S. Turnover of resident microglia in the normal adult mouse brain. *Neuroscience*. 1992;48(2):405-15. Epub 1992/01/01. doi: 10.1016/0306-4522(92)90500-2. PubMed PMID: 1603325.
130. Hopperton KE, Mohammad D, Trépanier MO, Giuliano V, Bazinet RP. Markers of microglia in post-mortem brain samples from patients with Alzheimer's disease: a systematic review. *Molecular Psychiatry*. 2018;23(2):177-98. doi: 10.1038/mp.2017.246.
131. Cho SH, Chen JA, Sayed F, Ward ME, Gao F, Nguyen TA, et al. SIRT1 deficiency in microglia contributes to cognitive decline in aging and neurodegeneration via epigenetic regulation of IL-1 $\beta$ . *J Neurosci*. 2015;35(2):807-18. Epub 2015/01/16. doi: 10.1523/jneurosci.2939-14.2015. PubMed PMID: 25589773; PubMed Central PMCID: PMC4293425.
132. Kleinberger G, Yamanishi Y, Suárez-Calvet M, Czirr E, Lohmann E, Cuyvers E, et al. TREM2 mutations implicated in neurodegeneration impair cell surface transport and phagocytosis. *Sci Transl Med*. 2014;6(243):243ra86. Epub 2014/07/06. doi: 10.1126/scitranslmed.3009093. PubMed PMID: 24990881.
133. Woodling NS, Wang Q, Priyam PG, Larkin P, Shi J, Johansson JU, et al. Suppression of Alzheimer-associated inflammation by microglial prostaglandin-E2 EP4 receptor signaling. *J Neurosci*. 2014;34(17):5882-94. Epub 2014/04/25. doi: 10.1523/jneurosci.0410-14.2014. PubMed PMID: 24760848; PubMed Central PMCID: PMC43996215.
134. Jin LW, Horiuchi M, Wulff H, Liu XB, Cortopassi GA, Erickson JD, et al. Dysregulation of glutamine transporter SNAT1 in Rett syndrome microglia: a mechanism for mitochondrial dysfunction and neurotoxicity. *J Neurosci*. 2015;35(6):2516-29. Epub 2015/02/13. doi: 10.1523/jneurosci.2778-14.2015. PubMed PMID: 25673846; PubMed Central PMCID: PMC4323531.
135. Hagemeyer N, Kierdorf K, Frenzel K, Xue J, Ringelhan M, Abdullah Z, et al. Transcriptome-based profiling of yolk sac-derived macrophages reveals a role for Irf8 in macrophage maturation. *The EMBO journal*. 2016;35(16):1730-44. Epub 2016/07/13. doi: 10.15252/embj.201693801. PubMed PMID: 27412700.
136. Dubbelaar ML, Kracht L, Eggen BJL, Boddeke EWGM. The Kaleidoscope of Microglial Phenotypes. *Frontiers in immunology*. 2018;9:1753-. doi: 10.3389/fimmu.2018.01753. PubMed PMID: 30108586.
137. Butovsky O, Jedrychowski MP, Moore CS, Cialic R, Lanser AJ, Gabriely G, et al. Identification of a unique TGF- $\beta$ -dependent molecular and functional signature in microglia. *Nature Neuroscience*. 2014;17(1):131-43. doi: 10.1038/nn.3599.

138. Healy LM, Perron G, Won S-Y, Rao VTS, Guiot M-C, Moore C, et al. Differential transcriptional response profiles in human myeloid cell populations. *Clinical Immunology*. 2018;189:63-74. doi: <https://doi.org/10.1016/j.clim.2016.04.006>.
139. Walton MR, Gibbons H, MacGibbon GA, Sirimanne E, Saura J, Gluckman PD, et al. PU.1 expression in microglia. *Journal of Neuroimmunology*. 2000;104(2):109-15. doi: [https://doi.org/10.1016/S0165-5728\(99\)00262-3](https://doi.org/10.1016/S0165-5728(99)00262-3).
140. Scott EW, Fisher RC, Olson MC, Kehrli EW, Simon MC, Singh H. PU.1 functions in a cell-autonomous manner to control the differentiation of multipotential lymphoid-myeloid progenitors. *Immunity*. 1997;6(4):437-47. Epub 1997/04/01. doi: 10.1016/s1074-7613(00)80287-3. PubMed PMID: 9133423.
141. DeKoter RP, Singh H. Regulation of B lymphocyte and macrophage development by graded expression of PU.1. *Science*. 2000;288(5470):1439-41. Epub 2000/05/29. doi: 10.1126/science.288.5470.1439. PubMed PMID: 10827957.
142. Jung S, Aliberti J, Graemmel P, Sunshine MJ, Kreutzberg GW, Sher A, et al. Analysis of fractalkine receptor CX(3)CR1 function by targeted deletion and green fluorescent protein reporter gene insertion. *Mol Cell Biol*. 2000;20(11):4106-14. Epub 2000/05/11. doi: 10.1128/mcb.20.11.4106-4114.2000. PubMed PMID: 10805752; PubMed Central PMCID: PMC85780.
143. Frank LE, Caldera-Siu AD, Pothos EN. Primary Dissociated Midbrain Dopamine Cell Cultures from Rodent Neonates. *JoVE*. 2008;(21):e820. doi: doi:10.3791/820.
144. Gaven F, Marin P, Claeysen S. Primary culture of mouse dopaminergic neurons. *Journal of visualized experiments : JoVE*. 2014;(91):e51751-e. doi: 10.3791/51751. PubMed PMID: 25226064.
145. Cardozo DL. Midbrain dopaminergic neurons from postnatal rat in long-term primary culture. *Neuroscience*. 1993;56(2):409-21. Epub 1993/09/01. doi: 10.1016/0306-4522(93)90342-d. PubMed PMID: 8247269.
146. Lautenschläger J, Mosharov EV, Kanter E, Sulzer D, Kaminski Schierle GS. An Easy-to-Implement Protocol for Preparing Postnatal Ventral Mesencephalic Cultures. *Frontiers in Cellular Neuroscience*. 2018;12:44.
147. GmbH MB. Neuron Isolation Kit, mouse. 2017:1-4.
148. Hui CW, Zhang Y, Herrup K. Non-Neuronal Cells Are Required to Mediate the Effects of Neuroinflammation: Results from a Neuron-Enriched Culture System. *PloS one*. 2016;11(1):e0147134-e. doi: 10.1371/journal.pone.0147134. PubMed PMID: 26788729.
149. Nagatsu T. Tyrosine hydroxylase: human isoforms, structure and regulation in physiology and pathology. *Essays Biochem*. 1995;30:15-35. Epub 1995/01/01. PubMed PMID: 8822146.
150. Poulin J-F, Zou J, Drouin-Ouellet J, Kim K-Youn A, Cicchetti F, Awatramani RB. Defining Midbrain Dopaminergic Neuron Diversity by Single-Cell Gene Expression Profiling. *Cell Reports*. 2014;9(3):930-43. doi: <https://doi.org/10.1016/j.celrep.2014.10.008>.
151. Soltani MH, Pichardo R, Song Z, Sangha N, Camacho F, Satyamoorthy K, et al. Microtubule-associated protein 2, a marker of neuronal differentiation, induces mitotic defects, inhibits growth of melanoma cells, and predicts metastatic potential of cutaneous melanoma. *The American journal of pathology*. 2005;166(6):1841-50. doi: 10.1016/S0002-9440(10)62493-5. PubMed PMID: 15920168.

152. Ysselstein D, Joshi M, Mishra V, Griggs AM, Asiago JM, McCabe GP, et al. Effects of impaired membrane interactions on  $\alpha$ -synuclein aggregation and neurotoxicity. *Neurobiol Dis.* 2015;79:150-63. Epub 2015/05/02. doi: 10.1016/j.nbd.2015.04.007. PubMed PMID: 25931201; PubMed Central PMCID: PMC4458405.
153. Strathearn KE, Yousef GG, Grace MH, Roy SL, Tambe MA, Ferruzzi MG, et al. Neuroprotective effects of anthocyanin- and proanthocyanidin-rich extracts in cellular models of Parkinson's disease. *Brain Res.* 2014;1555:60-77. Epub 2014/02/08. doi: 10.1016/j.brainres.2014.01.047. PubMed PMID: 24502982; PubMed Central PMCID: PMC4024464.
154. de Rus Jacquet A, Timmers M, Ma SY, Thieme A, McCabe GP, Vest JHC, et al. Lumbee traditional medicine: Neuroprotective activities of medicinal plants used to treat Parkinson's disease-related symptoms. *Journal of ethnopharmacology.* 2017;206:408-25. Epub 2017/02/15. doi: 10.1016/j.jep.2017.02.021. PubMed PMID: 28214539.
155. Block ML, Wu X, Pei Z, Li G, Wang T, Qin L, et al. Nanometer size diesel exhaust particles are selectively toxic to dopaminergic neurons: the role of microglia, phagocytosis, and NADPH oxidase. *Faseb j.* 2004;18(13):1618-20. Epub 2004/08/21. doi: 10.1096/fj.04-1945fje. PubMed PMID: 15319363.
156. Skibinski G, Nakamura K, Cookson MR, Finkbeiner S. Mutant LRRK2 toxicity in neurons depends on LRRK2 levels and synuclein but not kinase activity or inclusion bodies. *The Journal of neuroscience : the official journal of the Society for Neuroscience.* 2014;34(2):418-33. doi: 10.1523/JNEUROSCI.2712-13.2014. PubMed PMID: 24403142.
157. Borgs L, Peyre E, Alix P, Hanon K, Grobarczyk B, Godin JD, et al. Dopaminergic neurons differentiating from LRRK2 G2019S induced pluripotent stem cells show early neuritic branching defects. *Scientific reports.* 2016;6:33377-. doi: 10.1038/srep33377. PubMed PMID: 27640816.
158. Pais TF, Figueiredo C, Peixoto R, Braz MH, Chatterjee S. Necrotic neurons enhance microglial neurotoxicity through induction of glutaminase by a MyD88-dependent pathway. *Journal of Neuroinflammation.* 2008;5(1):43. doi: 10.1186/1742-2094-5-43.
159. Kim C, Lee H-J, Masliah E, Lee S-J. Non-cell-autonomous Neurotoxicity of  $\alpha$ -synuclein Through Microglial Toll-like Receptor 2. *Exp Neurobiol.* 2016;25(3):113-9. Epub 2016/06/08. doi: 10.5607/en.2016.25.3.113. PubMed PMID: 27358579.
160. Floden AM, Li S, Combs CK. Beta-amyloid-stimulated microglia induce neuron death via synergistic stimulation of tumor necrosis factor alpha and NMDA receptors. *J Neurosci.* 2005;25(10):2566-75. Epub 2005/03/11. doi: 10.1523/jneurosci.4998-04.2005. PubMed PMID: 15758166; PubMed Central PMCID: PMC4458405.
161. Roqué PJ, Dao K, Costa LG. Microglia mediate diesel exhaust particle-induced cerebellar neuronal toxicity through neuroinflammatory mechanisms. *NeuroToxicology.* 2016;56:204-14. doi: <https://doi.org/10.1016/j.neuro.2016.08.006>.
162. Polazzi E, Altamira LE, Eleuteri S, Barbaro R, Casadio C, Contestabile A, et al. Neuroprotection of microglial conditioned medium on 6-hydroxydopamine-induced neuronal death: role of transforming growth factor beta-2. *J Neurochem.* 2009;110(2):545-56. Epub 2009/05/22. doi: 10.1111/j.1471-4159.2009.06117.x. PubMed PMID: 19457129.
163. Haruwaka K, Ikegami A, Tachibana Y, Ohno N, Konishi H, Hashimoto A, et al. Dual microglia effects on blood brain barrier permeability induced by systemic inflammation. *Nature Communications.* 2019;10(1):5816. doi: 10.1038/s41467-019-13812-z.



164. Song P, Kwon Y, Joo J-Y, Kim D-G, Yoon JH. Secretomics to Discover Regulators in Diseases. *International journal of molecular sciences*. 2019;20(16):3893. doi: 10.3390/ijms20163893. PubMed PMID: 31405033.
165. Liu P, Weng Y, Sui Z, Wu Y, Meng X, Wu M, et al. Quantitative secretomic analysis of pancreatic cancer cells in serum-containing conditioned medium. *Scientific Reports*. 2016;6(1):37606. doi: 10.1038/srep37606.
166. Shin J, Rhim J, Kwon Y, Choi SY, Shin S, Ha C-W, et al. Comparative analysis of differentially secreted proteins in serum-free and serum-containing media by using BONCAT and pulsed SILAC. *Scientific Reports*. 2019;9(1):3096. doi: 10.1038/s41598-019-39650-z.
167. Joshi P, Turola E, Ruiz A, Bergami A, Libera DD, Benussi L, et al. Microglia convert aggregated amyloid- $\beta$  into neurotoxic forms through the shedding of microvesicles. *Cell Death & Differentiation*. 2014;21(4):582-93. doi: 10.1038/cdd.2013.180.
168. Prada I, Gabrielli M, Turola E, Iorio A, D'Arrigo G, Parolisi R, et al. Glia-to-neuron transfer of miRNAs via extracellular vesicles: a new mechanism underlying inflammation-induced synaptic alterations. *Acta Neuropathologica*. 2018;135(4):529-50. doi: 10.1007/s00401-017-1803-x.
169. Paolicelli RC, Bergamini G, Rajendran L. Cell-to-cell Communication by Extracellular Vesicles: Focus on Microglia. *Neuroscience*. 2019;405:148-57. doi: <https://doi.org/10.1016/j.neuroscience.2018.04.003>.
170. Grimaldi A, Serpe C, Chece G, Nigro V, Sarra A, Ruzicka B, et al. Microglia-Derived Microvesicles Affect Microglia Phenotype in Glioma. *Frontiers in Cellular Neuroscience*. 2019;13(41). doi: 10.3389/fncel.2019.00041.
171. Xia Y, Zhang G, Han C, Ma K, Guo X, Wan F, et al. Microglia as modulators of exosomal alpha-synuclein transmission. *Cell Death & Disease*. 2019;10(3):174. doi: 10.1038/s41419-019-1404-9.
172. Langston J, Ballard P, Tetrud J, Irwin I. Chronic Parkinsonism in humans due to a product of meperidine-analog synthesis. *Science*. 1983;219(4587):979-80. doi: 10.1126/science.6823561.
173. Cannon JR, Tapias V, Na HM, Honick AS, Drolet RE, Greenamyre JT. A highly reproducible rotenone model of Parkinson's disease. *Neurobiology of Disease*. 2009;34(2):279-90. doi: <https://doi.org/10.1016/j.nbd.2009.01.016>.
174. Betarbet R, Sherer TB, MacKenzie G, Garcia-Osuna M, Panov AV, Greenamyre JT. Chronic systemic pesticide exposure reproduces features of Parkinson's disease. *Nat Neurosci*. 2000;3(12):1301-6. Epub 2000/12/02. doi: 10.1038/81834. PubMed PMID: 11100151.
175. Haddad D, Nakamura K. Understanding the susceptibility of dopamine neurons to mitochondrial stressors in Parkinson's disease. *FEBS letters*. 2015;589(24 Pt A):3702-13. Epub 2015/10/23. doi: 10.1016/j.febslet.2015.10.021. PubMed PMID: 26526613.
176. Guzman JN, Sanchez-Padilla J, Wokosin D, Kondapalli J, Ilijic E, Schumacker PT, et al. Oxidant stress evoked by pacemaking in dopaminergic neurons is attenuated by DJ-1. *Nature*. 2010;468(7324):696-700. doi: 10.1038/nature09536.
177. Foehring RC, Zhang XF, Lee JC, Callaway JC. Endogenous calcium buffering capacity of substantia nigral dopamine neurons. *J Neurophysiol*. 2009;102(4):2326-33. Epub 2009/08/14. doi: 10.1152/jn.00038.2009. PubMed PMID: 19675297; PubMed Central PMCID: PMC2775382.

178. Matsuda W, Furuta T, Nakamura KC, Hioki H, Fujiyama F, Arai R, et al. Single nigrostriatal dopaminergic neurons form widely spread and highly dense axonal arborizations in the neostriatum. *J Neurosci*. 2009;29(2):444-53. Epub 2009/01/16. doi: 10.1523/jneurosci.4029-08.2009. PubMed PMID: 19144844; PubMed Central PMCID: PMC6664950.
179. Orimo S, Uchihara T, Kanazawa T, Itoh Y, Wakabayashi K, Kakita A, et al. Unmyelinated axons are more vulnerable to degeneration than myelinated axons of the cardiac nerve in Parkinson's disease. *Neuropathol Appl Neurobiol*. 2011;37(7):791-802. Epub 2011/06/24. doi: 10.1111/j.1365-2990.2011.01194.x. PubMed PMID: 21696416.
180. Hildebrand C, Remahl S, Persson H, Bjartmar C. Myelinated nerve fibres in the CNS. *Prog Neurobiol*. 1993;40(3):319-84. Epub 1993/03/01. doi: 10.1016/0301-0082(93)90015-k. PubMed PMID: 8441812.
181. Obeso JA, Rodriguez-Oroz MC, Goetz CG, Marin C, Kordower JH, Rodriguez M, et al. Missing pieces in the Parkinson's disease puzzle. *Nature Medicine*. 2010;16(6):653-61. doi: 10.1038/nm.2165.
182. Surmeier DJ, Guzman JN, Sanchez-Padilla J, Goldberg JA. Chapter 4 - What causes the death of dopaminergic neurons in Parkinson's disease? In: Björklund A, Cenci MA, editors. *Progress in Brain Research*. 183: Elsevier; 2010. p. 59-77.
183. Lawson LJ, Perry VH, Dri P, Gordon S. Heterogeneity in the distribution and morphology of microglia in the normal adult mouse brain. *Neuroscience*. 1990;39(1):151-70. Epub 1990/01/01. doi: 10.1016/0306-4522(90)90229-w. PubMed PMID: 2089275.
184. Yang TT, Lin C, Hsu CT, Wang TF, Ke FY, Kuo YM. Differential distribution and activation of microglia in the brain of male C57BL/6J mice. *Brain Struct Funct*. 2013;218(4):1051-60. Epub 2012/08/14. doi: 10.1007/s00429-012-0446-x. PubMed PMID: 22886465.
185. Zorov DB, Vorobjev IA, Popkov VA, Babenko VA, Zorova LD, Pevzner IB, et al. Lessons from the Discovery of Mitochondrial Fragmentation (Fission): A Review and Update. *Cells*. 2019;8(2):175. doi: 10.3390/cells8020175. PubMed PMID: 30791381.
186. Berg S, Kutra D, Kroeger T, Straehle CN, Kausler BX, Haubold C, et al. ilastik: interactive machine learning for (bio)image analysis. *Nat Methods*. 2019;16(12):1226-32. Epub 2019/10/02. doi: 10.1038/s41592-019-0582-9. PubMed PMID: 31570887.
187. Schindelin J, Arganda-Carreras I, Frise E, Kaynig V, Longair M, Pietzsch T, et al. Fiji: an open-source platform for biological-image analysis. *Nature Methods*. 2012;9(7):676-82. doi: 10.1038/nmeth.2019. PubMed PMID: WOS:000305942200021.
188. Ramstead AG, Wallace JA, Lee SH, Bauer KM, Tang WW, Ekiz HA, et al. Mitochondrial Pyruvate Carrier 1 Promotes Peripheral T Cell Homeostasis through Metabolic Regulation of Thymic Development. *Cell Rep*. 2020;30(9):2889-99.e6. Epub 2020/03/05. doi: 10.1016/j.celrep.2020.02.042. PubMed PMID: 32130894; PubMed Central PMCID: PMC7170217.
189. Marschallinger J, Iram T, Zardeneta M, Lee SE, Lehallier B, Haney MS, et al. Lipid-droplet-accumulating microglia represent a dysfunctional and proinflammatory state in the aging brain (vol 33, pg 247, 2019). *Nature Neuroscience*. 2020;23(2):294-. doi: 10.1038/s41593-020-0595-9. PubMed PMID: WOS:000510340400001.
190. Fam TK, Klymchenko AS, Collot M. Recent Advances in Fluorescent Probes for Lipid Droplets. *Materials (Basel)*. 2018;11(9):1768. doi: 10.3390/ma11091768. PubMed PMID: 30231571.

191. Qiu B, Simon MC. BODIPY 493/503 Staining of Neutral Lipid Droplets for Microscopy and Quantification by Flow Cytometry. *Bio-protocol*. 2016;6(17):e1912. doi: 10.21769/BioProtoc.1912. PubMed PMID: 28573161.
192. von Zahn J, Möller T, Kettenmann H, Nolte C. Microglial phagocytosis is modulated by pro- and anti-inflammatory cytokines. *Neuroreport*. 1997;8(18):3851-6. Epub 1998/02/14. doi: 10.1097/00001756-199712220-00003. PubMed PMID: 9462454.
193. Lively S, Schlichter LC. Microglia Responses to Pro-inflammatory Stimuli (LPS, IFN $\gamma$ +TNF $\alpha$ ) and Reprogramming by Resolving Cytokines (IL-4, IL-10). *Frontiers in cellular neuroscience*. 2018;12:215-. doi: 10.3389/fncel.2018.00215. PubMed PMID: 30087595.
194. Cushman SW. STRUCTURE-FUNCTION RELATIONSHIPS IN THE ADIPOSE CELL : I. Ultrastructure of the Isolated Adipose Cell. *Journal of Cell Biology*. 1970;46(2):326-41. doi: 10.1083/jcb.46.2.326.
195. Thiam AR, Beller M. The why, when and how of lipid droplet diversity. *Journal of Cell Science*. 2017;130(2):315-24. doi: 10.1242/jcs.192021.
196. Guo Y, Cordes KR, Farese RV, Jr., Walther TC. Lipid droplets at a glance. *Journal of cell science*. 2009;122(Pt 6):749-52. doi: 10.1242/jcs.037630. PubMed PMID: 19261844.
197. Pratten MK, Lloyd JB. Pinocytosis and phagocytosis: the effect of size of a particulate substrate on its mode of capture by rat peritoneal macrophages cultured in vitro. *Biochimica et Biophysica Acta (BBA) - General Subjects*. 1986;881(3):307-13. doi: [https://doi.org/10.1016/0304-4165\(86\)90020-6](https://doi.org/10.1016/0304-4165(86)90020-6).
198. Shanbhag AS, Jacobs JJ, Black J, Galante JO, Glant TT. Macrophage/particle interactions: Effect of size, composition and surface area. *Journal of Biomedical Materials Research*. 1994;28(1):81-90. doi: 10.1002/jbm.820280111.
199. Tinevez JY, Perry N, Schindelin J, Hoopes GM, Reynolds GD, Laplantine E, et al. TrackMate: An open and extensible platform for single-particle tracking. *Methods*. 2017;115:80-90. doi: 10.1016/j.ymeth.2016.09.016. PubMed PMID: WOS:000398010700009.
200. Fricker M, Oliva-Martín MJ, Brown GC. Primary phagocytosis of viable neurons by microglia activated with LPS or A $\beta$  is dependent on calreticulin/LRP phagocytic signalling. *Journal of Neuroinflammation*. 2012;9(1):196. doi: 10.1186/1742-2094-9-196.
201. Wu TT, Chen TL, Chen RM. Lipopolysaccharide triggers macrophage activation of inflammatory cytokine expression, chemotaxis, phagocytosis, and oxidative ability via a toll-like receptor 4-dependent pathway: validated by RNA interference. *Toxicol Lett*. 2009;191(2-3):195-202. Epub 2009/09/09. doi: 10.1016/j.toxlet.2009.08.025. PubMed PMID: 19735705.
202. Kawabe K, Takano K, Moriyama M, Nakamura Y. Lipopolysaccharide-Stimulated Transglutaminase 2 Expression Enhances Endocytosis Activity in the Mouse Microglial Cell Line BV-2. *Neuroimmunomodulation*. 2015;22(4):243-9. doi: 10.1159/000365484.
203. Zanoni I, Ostuni R, Marek LR, Barresi S, Barbalat R, Barton GM, et al. CD14 controls the LPS-induced endocytosis of Toll-like receptor 4. *Cell*. 2011;147(4):868-80. doi: 10.1016/j.cell.2011.09.051. PubMed PMID: 22078883.
204. West MA, Wallin RP, Matthews SP, Svensson HG, Zaru R, Ljunggren HG, et al. Enhanced dendritic cell antigen capture via toll-like receptor-induced actin remodeling. *Science*. 2004;305(5687):1153-7. Epub 2004/08/25. doi: 10.1126/science.1099153. PubMed PMID: 15326355.

205. Li L, Wan T, Wan M, Liu B, Cheng R, Zhang R. The effect of the size of fluorescent dextran on its endocytic pathway. *Cell Biology International*. 2015;39(5):531-9. doi: 10.1002/cbin.10424.
206. Oliver JM, Berlin RD, Davis BH. Use of horseradish peroxidase and fluorescent dextrans to study fluid pinocytosis in leukocytes. In: Di Sabato G, Langone JJ, Van Vunakis H, editors. *Methods in Enzymology*. 108: Academic Press; 1984. p. 336-47.
207. Marchetti A, Lelong E, Cosson P. A measure of endosomal pH by flow cytometry in *Dictyostelium*. *BMC Research Notes*. 2009;2(1):7. doi: 10.1186/1756-0500-2-7.
208. Ohkuma S, Poole B. Fluorescence probe measurement of the intralysosomal pH in living cells and the perturbation of pH by various agents. *Proceedings of the National Academy of Sciences*. 1978;75(7):3327-31. doi: 10.1073/pnas.75.7.3327.
209. Aerbajinai W, Lee K, Chin K, Rodgers GP. Glia maturation factor- $\gamma$  negatively modulates TLR4 signaling by facilitating TLR4 endocytic trafficking in macrophages. *Journal of immunology* (Baltimore, Md : 1950). 2013;190(12):6093-103. Epub 2013/05/15. doi: 10.4049/jimmunol.1203048. PubMed PMID: 23677465.
210. Husebye H, Halaas Ø, Stenmark H, Tunheim G, Sandanger Ø, Bogen B, et al. Endocytic pathways regulate Toll-like receptor 4 signaling and link innate and adaptive immunity. *The EMBO journal*. 2006;25(4):683-92. Epub 2006/02/09. doi: 10.1038/sj.emboj.7600991. PubMed PMID: 16467847.
211. Gillardon F. Leucine-rich repeat kinase 2 phosphorylates brain tubulin-beta isoforms and modulates microtubule stability--a point of convergence in parkinsonian neurodegeneration? *J Neurochem*. 2009;110(5):1514-22. Epub 2009/06/24. doi: 10.1111/j.1471-4159.2009.06235.x. PubMed PMID: 19545277.
212. Kawakami F, Yabata T, Ohta E, Maekawa T, Shimada N, Suzuki M, et al. LRRK2 phosphorylates tubulin-associated tau but not the free molecule: LRRK2-mediated regulation of the tau-tubulin association and neurite outgrowth. *PLoS One*. 2012;7(1):e30834. Epub 2012/02/04. doi: 10.1371/journal.pone.0030834. PubMed PMID: 22303461; PubMed Central PMCID: PMC3267742.
213. Kaverina I, Straube A. Regulation of cell migration by dynamic microtubules. *Semin Cell Dev Biol*. 2011;22(9):968-74. Epub 2011/10/04. doi: 10.1016/j.semcdb.2011.09.017. PubMed PMID: 22001384.
214. Garcin C, Straube A. Microtubules in cell migration. *Essays in biochemistry*. 2019;63(5):509-20. doi: 10.1042/EBC20190016. PubMed PMID: 31358621.
215. De Simone R, Niturad CE, De Nuccio C, Cat MAA, Visentin S, Minghetti L. TGF- $\beta$  and LPS modulate ADP-induced migration of microglial cells through P2Y1 and P2Y12 receptor expression. *Journal of ...* 2010;115(2):450-9. doi: 10.1111/j.1471-4159.2010.06937.x. PubMed PMID: 10.1111/j.1471-4159.2010.06937.x.
216. Fan Y, Xie L, Chung CY. Signaling Pathways Controlling Microglia Chemotaxis. *Mol Cells*. 2017;40(3):163-8. Epub 2017/03/18. doi: 10.14348/molcells.2017.0011. PubMed PMID: 28301917; PubMed Central PMCID: PMC5386953.
217. Bardien S, Lesage S, Brice A, Carr J. Genetic characteristics of leucine-rich repeat kinase 2 (LRRK2) associated Parkinson's disease. *Parkinsonism Relat Disord*. 2011;17(7):501-8. Epub 2011/06/07. doi: 10.1016/j.parkreldis.2010.11.008. PubMed PMID: 21641266.

218. Berg D, Schweitzer KJ, Leitner P, Zimprich A, Lichtner P, Belcredi P, et al. Type and frequency of mutations in the LRRK2 gene in familial and sporadic Parkinson's disease\*. *Brain*. 2005;128(Pt 12):3000-11. Epub 2005/10/28. doi: 10.1093/brain/awh666. PubMed PMID: 16251215.
219. Weykopf B, Haupt S, Jungverdorben J, Flitsch LJ, Hebisch M, Liu G-H, et al. Induced pluripotent stem cell-based modeling of mutant LRRK2-associated Parkinson's disease. *European Journal of Neuroscience*. 2019;49(4):561-89. doi: 10.1111/ejn.14345.
220. Danés AS, Patin YR, Carbajal IC, Delgado SJ, Caig C, Mora S, et al. Disease-specific phenotypes in dopamine neurons from human iPSC-based models of genetic and sporadic Parkinson's disease. *EMBO Molecular Medicine*. 2012;4(5):380-95. doi: 10.1002/emmm.201200215. PubMed PMID: 22407749; PubMed Central PMCID: PMC3403296.
221. López de Maturana R, Lang V, Zubiarrain A, Sousa A, Vázquez N, Gorostidi A, et al. Mutations in LRRK2 impair NF- $\kappa$ B pathway in iPSC-derived neurons. *Journal of Neuroinflammation*. 2016;13(1):295. doi: 10.1186/s12974-016-0761-x.
222. Liu GH, Qu J, Suzuki K, Nivet E, Li M, Montserrat N, et al. Progressive degeneration of human neural stem cells caused by pathogenic LRRK2. *Nature*. 2012;491(7425):603-7. Epub 2012/10/19. doi: 10.1038/nature11557. PubMed PMID: 23075850; PubMed Central PMCID: PMC3504651.
223. Martin I, Kim JW, Lee BD, Kang HC, Xu J-C, Jia H, et al. Ribosomal Protein s15 Phosphorylation Mediates LRRK2 Neurodegeneration in Parkinson's Disease. *Cell*. 2014;157(2):472-85. doi: 10.1016/j.cell.2014.01.064. PubMed PMID: 10.1016/j.cell.2014.01.064.
224. Miklossy J, Doudet DD, Schwab C, Yu S, McGeer EG, McGeer PL. Role of ICAM-1 in persisting inflammation in Parkinson disease and MPTP monkeys. *Exp Neurol*. 2006;197(2):275-83. Epub 2005/12/13. doi: 10.1016/j.expneurol.2005.10.034. PubMed PMID: 16336966.
225. Reddy PH. Inhibitors of mitochondrial fission as a therapeutic strategy for diseases with oxidative stress and mitochondrial dysfunction. *J Alzheimers Dis*. 2014;40(2):245-56. Epub 2014/01/15. doi: 10.3233/jad-132060. PubMed PMID: 24413616; PubMed Central PMCID: PMC3972337.
226. Vantaggiato C, Castelli M, Giovarelli M, Orso G, Bassi MT, Clementi E, et al. The Fine Tuning of Drp1-Dependent Mitochondrial Remodeling and Autophagy Controls Neuronal Differentiation. *Frontiers in Cellular Neuroscience*. 2019;13(120). doi: 10.3389/fncel.2019.00120.
227. Stoker TB, Torsney KM, Barker RA. Emerging Treatment Approaches for Parkinson's Disease. *Front Neurosci*. 2018;12:693-. doi: 10.3389/fnins.2018.00693. PubMed PMID: 30349448.
228. Kikuchi T, Morizane A, Doi D, Magotani H, Onoe H, Hayashi T, et al. Human iPSC-derived dopaminergic neurons function in a primate Parkinson's disease model. *Nature*. 2017;548(7669):592-6. Epub 2017/09/01. doi: 10.1038/nature23664. PubMed PMID: 28858313.
229. Barker RA, Parmar M, Studer L, Takahashi J. Human Trials of Stem Cell-Derived Dopamine Neurons for Parkinson's Disease: Dawn of a New Era. *Cell Stem Cell*. 2017;21(5):569-73. Epub 2017/11/04. doi: 10.1016/j.stem.2017.09.014. PubMed PMID: 29100010.

230. Huff JB, Wolfgang; Netz, Ralf; Anhut, Tiemo; Weisshart, Klaus. The Airyscan Detector from ZEISS Confocal Imaging with Improved Signal-to-Noise Ratio and Superresolution. Carl Zeiss Microscopy GmbH, Germany. 2015:1-19.
231. Harris LA, Skinner JR, Wolins NE. Imaging of neutral lipids and neutral lipid associated proteins. *Methods Cell Biol.* 2013;116:213-26. Epub 2013/10/09. doi: 10.1016/b978-0-12-408051-5.00011-5. PubMed PMID: 24099295; PubMed Central PMCID: PMC3870878.